EMERGING WORKS ON WIRELESS INDUCTIVE POWER TRANSFER: AUV CHARGING FROM CONSTANT CURRENT DISTRIBUTION AND ANALYSIS OF CONTROLS IN EV DYNAMIC CHARGING

by

Anindya Chitta Bagchi

A dissertation submitted in partial fulfillment
of the requirements for the degree

of

DOCTOR OF PHILOSOPHY

in

Electrical Engineering

Approved:

Regan Zane, PhD Major Professor	Abhilash Kamineni, PhD Committee Member
Reyhan Baktur, PhD Committee Member	Jacob Gunther, PhD Committee Member
Nick Roberts, PhD Committee Member	D. Richard Cutler, Ph.D. Interim Vice Provost of Graduate Studies

UTAH STATE UNIVERSITY
Logan, Utah

2020

ABSTRACT

Emerging Works On Wireless Inductive Power Transfer:
AUV Charging From Constant Current Distribution
and Analysis of Controls in EV Dynamic Charging

by

Anindya Chitta Bagchi, Doctor of Philosophy
Utah State University, 2020

Major Professor: Regan Zane, Ph.D.
Department: Electrical and Computer Engineering

Wireless power transfer through inductive coupling, termed as inductive power transfer (IPT), is one of the important technologies in power electronics that enable transfer of power between entities without physical connections. While it has seen significant growth in the areas such as electric vehicle charging, phone charging and biomedical implants, its emerging applications include charging of autonomous underwater vehicles (AUVs) and dynamic charging of electric vehicles from the roadway. This dissertation addresses a few key challenges in these areas of IPT applications, paving the way for future developments.

With recent developments in marine systems such as ocean observatories and sub-sea oil and gas fields, electrical equipment and AUVs are required to be installed deep in the sea-bed. They are typically supplied power through constant dc low-current distribution to avoid adverse effects of voltage drops along the cables. While wireless charging of AUVs are common for deep-sea applications, the existing systems are not compatible to interface with constant current distributions. This dissertation proposes underwater IPT topologies to interface directly with such constant current distribution and generate a constant voltage output supply to the on-board systems inside the AUVs. The coupler shapes, size and

operating frequency are selected through analysis and careful consideration of the effects of seawater on performance of underwater IPT systems to achieve high power transfer efficiency. Key expressions are developed for the steady-state operation and the design of the system to maintain constant output voltage over a wide load range, which are experimentally validated with laboratory prototypes. In addition, small-signal phasor model of the topologies are developed to help in future design of controllers for voltage regulated operation.

In the area of electric vehicle dynamic wireless power transfer (EV DWPT), one of the key challenge for future research is the control of power flow with dynamically varying coupling and with different topologies and gap ranges. With various couplers, compensations and converters proposed in ongoing EV DWPT works, it is important to study their control performances and interoperability for future commercialization. As part of this dissertation, the control performances of different EV DWPT topologies, especially different compensation topologies and control handles, are studied and compared. Key performance metrics are developed to perform such comparisons, helping in bringing out the effectiveness of the controls in the face of varying coupling and desired power regulation range. Based on that, topologies are suggested for future research for improved controllability. In addition, effect of communication latency on control bandwidth for these topologies are studied, to recommend proper EV DWPT arrangements to avoid control bandwidth related troubles. Analytical expressions and simulation results are used to validate the comparison results and shape the recommendations from this research.

(217 pages)

PUBLIC ABSTRACT

Emerging Works On Wireless Inductive Power Transfer:
AUV Charging From Constant Current Distribution
and Analysis of Controls in EV Dynamic Charging
Anindya Chitta Bagchi

Wireless power transfer through inductive coupling, termed as inductive power transfer (IPT), is one of the important technologies in power electronics that enable transfer of power between entities without physical connections. While it has seen significant growth in the areas such as electric vehicle charging, phone charging and biomedical implants, its emerging applications include charging of autonomous underwater vehicles (AUVs) and dynamic charging of electric vehicles from the roadway. This dissertation addresses a few key challenges in these areas of IPT applications, paving the way for future developments.

For the WPT for AUV, the recently developing sea-bed installed marine systems are targeted, which typically gets power from on-shore sources through constant dc low-current distribution. As the present underwater IPT topologies are not suitable for such applications, this dissertation proposes underwater IPT topologies to interface directly with such constant current distribution and provide a constant voltage output supply to the on-board systems inside the AUVs. The considerations for seawater losses and the small-signal models for control purposes are also addressed. Analysis and experimental results are provided for validations of the analytical designs and models.

In the area of electric vehicle dynamic wireless power transfer (EV DWPT), the comparison of control performances of different coupler, compensation topologies and control implementations are addressed. The effect of communication latency on control bandwidth are also addressed. The outcomes are presented through analysis and simulations, and

based on that future research recommendations are made to pave way for future commercial developments of well regulated and interoperable EV DWPT systems.

Dedicated to my amazing parents Ashim Ranjan Bagchi and Nivedita Bagchi, my sweet wife Sarah Ramos and our nice cat Nash.

ACKNOWLEDGMENTS

First of all, I would like to express my most sincere gratitude for my advisor, Dr. Regan Zane, for his endless guidance, encouragement and support throughout my PhD program to make it a success. Dr. Zane's help, trust and tolerance allowed me to explore beyond my limits, which formed the basis of my dissertation work. I would also like to thank my committee members, Dr. Abhilash Kamineni, Dr. Reyhan Baktur, Dr. Jacob Gunther and Dr. Nick Roberts for reviewing my work and providing their valuable advice towards making this work a success. A special thanks to Dr. Abhilash Kamineni, for collaborating with me in a lot of my works and supporting me with his prior knowledge and experiences.

I am grateful to the Utah State University Power Electronics Lab (UPEL), the Raytheon Company and the Idaho National Laboratory for the academic and financial supports, which allowed me to continue my education and conduct cutting-edge research in the field of power electronics. I also deeply appreciate the help from my colleagues at UPEL for their collaborations and wonderful discussions, which were important and beneficial to the success of this work. A special thanks to colleagues Tarak Saha and Rohail Hassan who were major collaborators in my experiments and brought new ideas and past experiences to make the experiments work towards achieving the desired goals. I would also like to thank our lab managers for their efficient management of equipment and resources to help drive my work in a timely manner, and the mechanical designers Braden Eichmeier and Jonathan Scheelke for their critical helps in making my test setups.

Finally, I would like to thank my family, especially my parents and my wife, Sarah Ramos, for their unconditional love, inspiration and support throughout my PhD program. These have helped me successfully go through the stressful journey towards the completion of the PhD program, and for these I will be forever grateful to them.

Anindya Chitta Bagchi

CONTENTS

LIST OF TABLES

LIST OF FIGURES

ACRONYMS

AUV	Autonomous underwater vehicles
FHA	Fundamental harmonic approximation
FEM	Finite Element Method
SRC	Series resonant converter
PRC	Parallel resonant converter
ZVS	Zero voltage switching
ZVS	Zero current switching
WPT	Wireless power transfer
IPT	Inductive power transfer
DCM	Discontinuous conduction mode
CCM	Continuous conduction mode
EMI	Electromagnetic interference
SS	Series-series
SP	Series-parallel
PS	Parallel-series
PP	Parallel-parallel
EV	Electric vehicles
DWPT	Dynamic wireless power transfer
UPF	Unity power factor
PF	Power factor
LV	Low voltage
HV	High voltage
DCS	Double-coupled system
CVO	Constant voltage output

CHAPTER 1

Introduction and Review of Literature

With widespread growth in the application of electricity in many aspects of modern human life, it is becoming greatly important to transfer electricity between different entities safely and efficiently. Wired power transmission has been the conventional method where electrical power is transmitted through connecting wires. On the other hand, with developments in high-frequency power electronics, wireless power transfer (WPT) technologies have been developed, which have the capability to perform similar task even without any physical connections. As a result, WPT has penetrated into areas such as stationary and dynamic charging of electric vehicles (EVs), consumer electronics, autonomous underwater vehicles (AUVs) and microwave communications, where power transfer could have never been possible with wired charging systems due to physical separation requirements [1, 32–34].

WPT systems can be classified into near-field and far-field technologies, as shown in Fig. 1.1 [34]. Among them, the near-field methods are mostly utilized in high-power systems, whereas the far-field methods are mostly used for communication and photo-electricity purposes. The near-field WPT for power applications is typically achieved through the creation of either time-varying electromagnetic field or time-varying electric field, both of which have the capability to induce electricity into another closed path electric circuit placed within the reach of the field. The first technology is termed as inductive power transfer (IPT) [1, 35–37] and the second one is termed as capacitive power transfer (CPT) [37–39], as shown in Fig. 1.1. The frequency range of such systems range from low kHz to tens of MHz. Since the energy storage capability of electromagnetic field is much higher compared to electric field, IPT can achieve high power transfer and efficiency for larger air gaps and in the low to medium frequency range [37]. As a result, despite recent developments in the area of CPT, IPT has seen a much bigger growth among WPT systems encompassing various frequency and gap ranges.

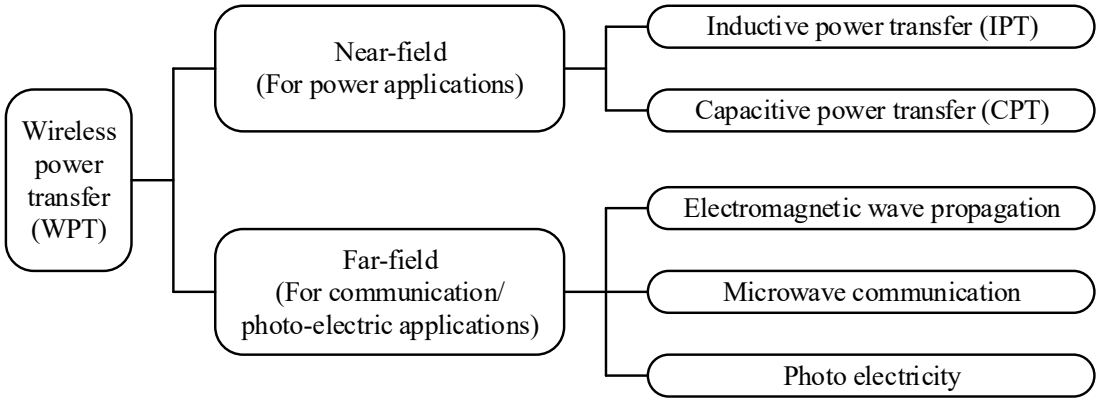

Fig. 1.1: Block diagram of different WPT technologies.

1.1 Basics of IPT and Overview of Its Application Areas

1.1.1 IPT Basics

IPT systems, pioneered by Nikola Tesla [35], work on the principle of electromagnetic induction, as per Ampere's Law and Faraday's Law [40]. A typical IPT coupler is shown in Fig. 1.2, where a time-varying current i_p is driven through the primary coil. This generates a time-varying electromagnetic field as per the principles of Ampere's Law in (1.1). The magnetic cores present are used to guide the flux towards the secondary coil and improve coupling. When a secondary coil is present within the area of the magnetic field, an electromotive force (v_{oc}) is generated in it as per Faraday's law (1.2). The relevant expressions are

$$\sum B\Delta l = \mu N_p I_p \ , \tag{1.1}$$

$$v_{oc} = -N_s \frac{d\varphi_{ps}}{dt} = M\frac{di_p}{dt} \ , \tag{1.2}$$

where μ is the absolute permeability of the magnetic path, including the magnetic core and the air gap, B is the magnetic flux density, Δl is the unit length of the conductor, N_p is the number of primary turns, N_s is the number of secondary turns, I_p is the primary coil current,

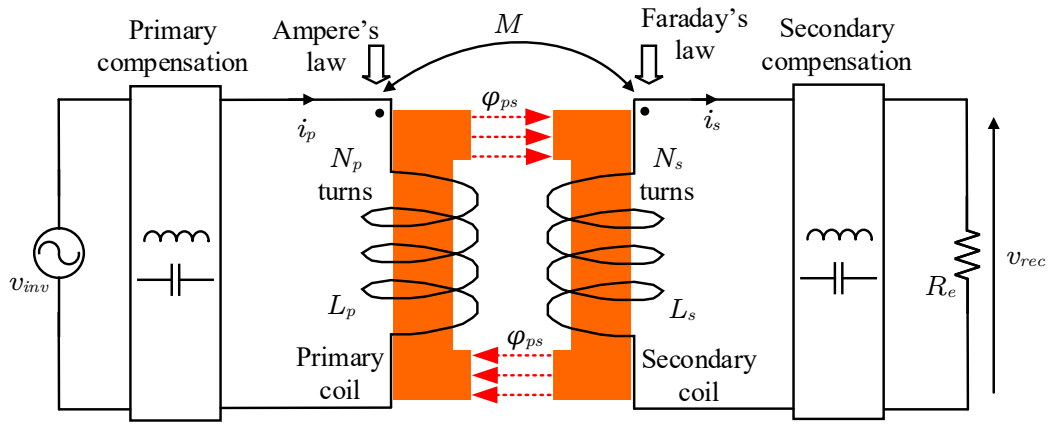

Fig. 1.2: A generic IPT system with a representative series-series compensation.

φ_{ps} is the flux linkage in the magnetic path of the secondary owing to the flux created by the primary, and M is the mutual inductance between the coils, given by $M = k\sqrt{L_p L_s}$ with L_p being the primary coil inductance and L_s being the secondary coil inductance. In practical IPT systems, a high frequency sinusoidal current is driven through the primary coil to induce sinusoidal voltage in the secondary coil, so that bulk power transfer happens at the fundamental frequency. Usage of higher frequency results in higher di/dt, leading to higher induced voltage with the same mutual inductance. However, the coils typically have higher losses at higher frequency due to skin effect and proximity effect, which greatly reduce the power transfer efficiency. Hence optimizations between them are required for practical design of IPT systems.

The high-frequency primary current is typically generated using a dc-ac inverter [1]. On the secondary side, typically a diode rectifier or active rectifier is employed to convert the high-frequency ac voltage to dc output, which can be used in storage purposes or further converted to power frequency ac for V2G type applications [1, 34]. Due to the presence of large air gap in the IPT coupler magnetic path as shown in Fig. 1.2, high amount of magnetic flux is needed to generate sufficient coupling to the secondary coil. This leads to high VA rating requirements of the inverter devices. To reduce the inverter device ratings, reactive power compensation networks are used to supply the required VA to the coils, as shown in Fig. 1.2. Similarly, compensations are employed on the secondary side to reduce

the secondary side device ratings, whereas the coils operate with higher VA. This has led to the use of resonant compensations in IPT systems, which also help in the reliable operation of the inverter and rectifier devices, often helping in soft-switching through zero voltage switching (ZVS) [41].

Utilizing the above-mentioned basics, the basic power equation of an IPT system is obtained as

$$P_{out} = \omega_s L_p I_p^2 k^2 Q_{sl} \ , \tag{1.3}$$

where, $\omega_s = 2\pi f_s$ is the angular frequency of the primary current with f_s being the primary current frequency and Q_{sl} is the loaded secondary quality factor, defined as the ratio of the secondary side reactive power to the active power delivered to the load, at the frequency of the primary current (also the frequency of the secondary coil current) [42]. Using this relation in terms of Q_{sl} normalizes the relation in terms of the secondary coil inductance and load specifications, which makes it simpler to interpret. The above expression is also written as

$$P_{out} = S_p k^2 Q_{sl} \ , \tag{1.4}$$

where $S_p = \omega L_p {I_p}^2$ denotes the VA rating of the primary coil. The expression in (1.4) is helpful as it takes out the complications associated with different inductance relationships also helps in figuring out where controls can be performed in IPT systems.

1.1.2 IPT Challenges

While providing the advantages of transferring electricity without physical connections, IPT is fraught with some major challenges that need to be addressed towards large-scale deployments. Due to larger reactive volt-ampere (VA) requirements of the IPT coils to generate the required amount of coupling flux, IPT systems (in general WPT systems) are less efficient than wired power transfer systems. This needs considerations during design of system component ratings and power loss management. Moreover, the leakage flux from

the IPT systems can result in detrimental effects, such as tissue heating in humans and malfunctioning of implanted equipment or surrounding equipment in the roadway [43, 44]. Hence, research and developments are in progress to optimize IPT pads and management of the leakage fields, such that widespread commercialization can happen in future.

1.1.3 Typical IPT Applications

A pictorial view of different IPT application areas is shown in Fig. 1.3. The main application areas where IPT has seen widespread developments include wireless charging of stationary electric vehicles [1, 33, 45], charging of mobile phones [43, 46] and biomedical implants [47]. IPT in some of these areas are also developed for commercial applications, such as the SAE J2954 standards for wireless EV charging [44] and Qi standard for consumer electronics wireless charging [43].

In recent years, developments are also growing towards emerging areas such as wireless charging of autonomous underwater vehicles (AUVs) [5,32] and dynamic charging of electric vehicles on the roadway [3,33]. IPT technology brings in unique advantages in both of these areas, but due to existing multi-dimensional challenges, they are yet to see widespread commercial developments. As a result, these applications are recently seeing a lot of active developments in research.

1.1.4 IPT for Autonomous Underwater Vehicles (AUVs)

AUVs, such as the REMUS-600, are typically used in ocean environments for off-shore surveying, sub-sea inspection, ocean science, marine archaeology, search operations and military applications [32, 48]. For this, they are often deployed in remote and mostly inaccessible areas, such as deep in the ocean, in the sea-bed and under ice coverings. To enable this, AUVs are equipped with on-board power system, different sensors such as sonars and salinity sensors, cameras, guiding and navigation systems and wireless communication modules, so that they can self-sustain for several hours or even days.

As a result, AUVs require on-board battery storage, which need to be frequently charged for their reliable operation. The conventional techniques for supplying power to

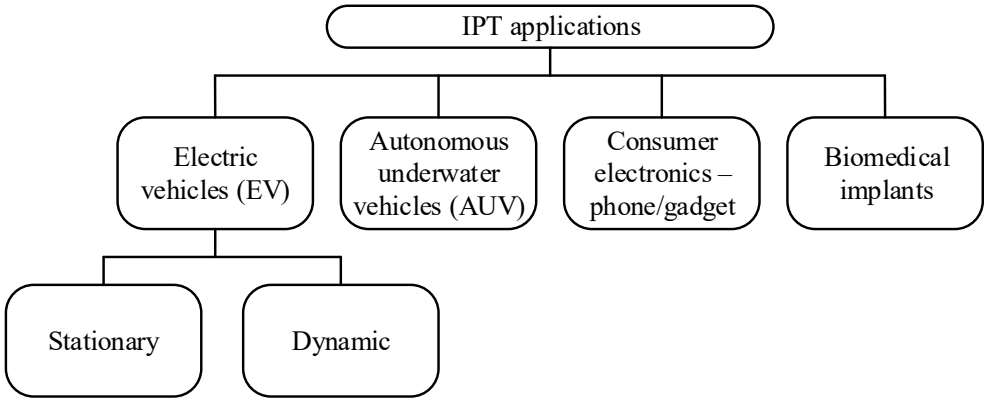

Fig. 1.3: Block diagram of different application areas of IPT.

AUVs include battery swapping [49] and solar charging [50], both of which require them to frequently travel up to the shore to get charged. To improve the autonomy of the AUVs, underwater charging systems such as docking [51], homing systems [52] and DEC charging [53] were developed. In these underwater charging methods, the AUVs are typically guided to a particular position where the charging system is installed. Funnel shaped docks and locking mechanisms are very common to keep the AUVs in a desired position.

Both wired and wireless charging are common among these underwater charging systems. The wired chargers typically use underwater electrical cables or wet-mate connectors [54]. Even if they are properly designed and sealed, they are mostly unreliable because of high corrosion in the seawater environment and risk of exposure to the partially conductive seawater. Hence the WPT based couplers based on IPT have gained popularity in AUV charging, such that power can be delivered to them without the requirement of any underwater physical connection.

A typical IPT system in AUV application driven from a voltage source is shown in Fig. 1.4(a), showing the primary coil mounted inside a charging station/platform, the secondary coil mounted within the AUV, and the gap between them formed by the thickness of the plastic/fiber glass body and seawater. The size of the secondary coil is typically constrained by the AUV dimensions, such that it can be housed properly within the AUV along with other accessories. With smaller AUVs for deep-sea deployed operations gaining

popularity, smaller IPT couplers are being in demand for them. Hence, even though low-frequency couplers with efficiency as high as 97 % and power rating as high as 1.1 MW have been designed for large ship applications [55], research is in progress for higher frequency operations with smaller pads to improve power density.

1.1.5 IPT for Dynamic Wireless Charging of Electric Vehicles (EV DWPT)

On the other hand, IPT systems for EVs were primarily developed for stationary EV charging, to avoid the heavy cabling requirements associated with wired fast-charging systems. However, stationary IPT does not help EVs, developed as a cleaner alternative to pollution-prone internal combustion engine (ICE) vehicles, overcome their major drawback of range anxiety associated with the lower energy and power density of EV batteries. Even with the most advanced battery technologies available, large, bulky batteries are required in EVs to match the driving range of ICE vehicles. They also often take much longer time to charge compared to filling up the gas tank in a gas station, due to their limited power capabilities. Even with wired and wireless fast-chargers [56–59] available till date, the EVs are not yet able to match the combination of long driving range and lower curb weight available with ICE vehicles

On the other hand, DWPT enables providing charge to the EV batteries from the roadway while they are in motion, such that smaller batteries can be used. Moreover, the smaller batteries take shorter time to charge-up in charging stations. Hence, dynamic charging is expected to help the EVs to get around their major drawbacks towards widespread commercialization with IPT working as the key enabling technology behind it.

The principal challenge in DWPT is to regulate the power flow from the roadway to the vehicle when it is moving, which results in dynamic variation in the coupling and mutual inductance profiles. As a result, DWPT systems are typically designed with multiple primary pads or rails embedded in the roadway along the road, with single or multiple secondary pads mounted under the vehicle, as shown in the general schematic in Fig. 1.4(b). With large number of topologies and control methods available in literature for EV DWPT, the research is moving in the direction of adjudging their controllability and interoperability,

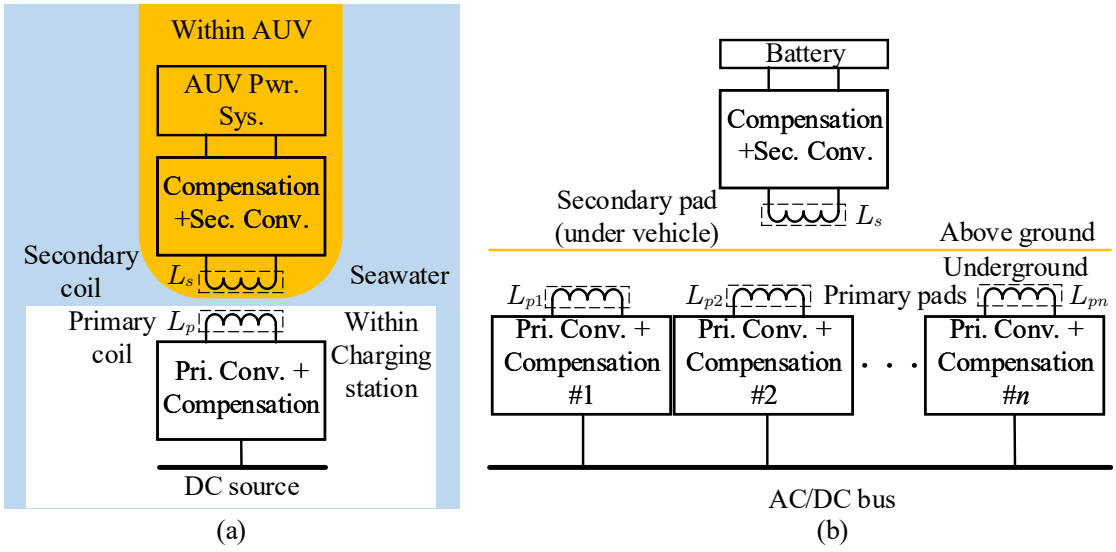

Fig. 1.4: Block diagram of (a) an AUV IPT system, (b) an EV DWPT system.

such that they can be standardised in future.

1.2 Research Problem: IPT for AUVs in Sub-sea Deployed Systems with Current Distribution

As an emerging trend, small AUVs are being developed for advanced sea-bed embedded marine systems such as ocean observatories and sub-sea oil and gas fields, for autonomous wide area monitoring purposes. These systems are typically deployed deep in the ocean, often hundreds of km away from the sea-shore. They typically involve electrical equipment for local power systems, robots, sensors and even AUVs. Their power systems should be designed to make them self-sustainable for long periods as frequent servicing may not be possible.

1.2.1 Significance of DC Current Distributions for Underwater Systems

To achieve the above, they are typically provided power from shore based sources or wave energy sites through long distance electricity distribution [60]. While long distance transmission and distribution using ac electricity is regularly used in electrical power systems, they are difficult to use for charging applications as ac electricity cannot be stored.

For this purpose, dc distribution systems were developed for systems requiring electrical storage such as the underwater electrical systems [60].

DC distributions can be classified into constant voltage (CV) and constant current (CC) distributions, as shown in Fig. 1.5. In CV distribution, the loads and other interface converters are connected in parallel with each other with the distribution system, which is depicted in Fig. 1.5(a). While this is convenient for most applications, the resistances of the distribution lines affect the load terminal voltages in such systems. Hence, to maintain a certain voltage across the converter situated at the farthest end, the system needs to be proportionally over-designed to take care of the voltage drops. Still, it may not be of concern for typical dc distribution systems in a small area.

However, for the long-distance power distribution required for powering the underwater electrical systems from on-shore systems, the above is not palpable. The cable resistance for such system is substantial, which leads to large load-dependent voltage drop in case voltage distribution is used. Instead, using a CC distribution as shown in Fig. 1.5(b), the effects of load-dependent voltage drop is alleviated. In this case, the cable voltage drop is constant and the input to the load converters are not affected due to the voltage drop, irrespective of the total loading. Moreover, for the same reasoning, the partially conductive seawater can be utilized as the ground return using CC distribution, which saves half the cost of the cable. Hence CC distributions are found most suitable for power distribution to underwater systems [60]. As a result, the load interface converters used in such systems are to be designed to take power from the constant current input rather than the conventional voltage sources.

1.2.2 IPT System Design with Underwater Constant Current Distribution

Due to the above reasons, AUV IPT systems for such underwater systems also need to be designed to interface with the constant current distribution. Considering this, a typical underwater current distribution system with load converters and potential converters for AUV IPT connected in series is shown in Fig. 1.6.

It can be seen that the load converters for such systems are designed with constant

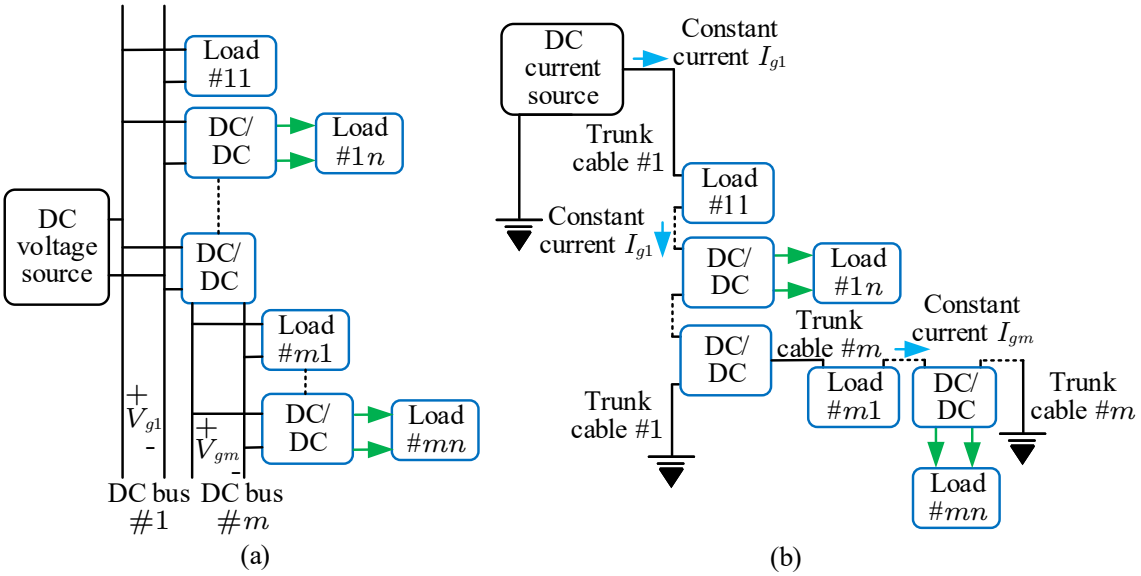

Fig. 1.5: Schematic diagrams dc distributions (a) CV distribution, (b) CC distribution.

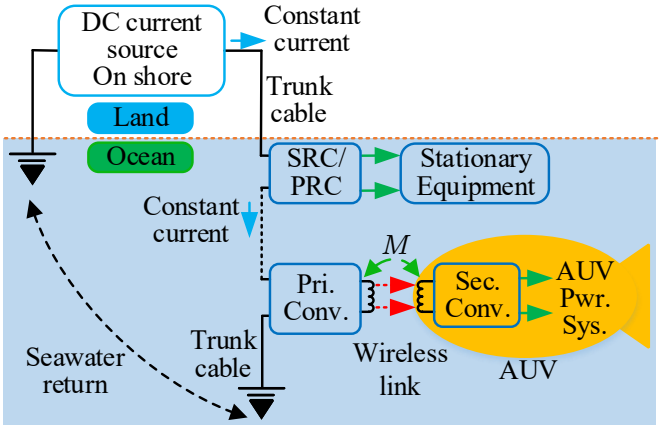

Fig. 1.6: Schematic diagram of a constant current undersea power distribution with load converters and AUV charger.

current input rather than constant voltage, which results in higher input voltages at higher operating power. Considering these effects, dc-dc converters for conductive power supply applications were designed using resonant conversion techniques, with series resonant converters (SRC) generating constant current output [61–64] and parallel resonant converters (PRC) generating constant voltage output [65,66]. With suitable designs, the resonant converters can achieve zero voltage switching (ZVS) of the devices, which improves efficiency, eliminates high-voltage parasitic ringings during switching transitions and correspondingly reduces electromagnetic interference (EMI) generation to improve system robustness and reliability [41].

Even though these converters cannot be directly used for AUV IPT systems, similar technologies can be utilized as IPT systems are designed with resonant compensations [1]. Also, the existing underwater IPT systems mostly focus on typical voltage input topologies with series-series (SS) or series-parallel (SP) compensations for mostly constant current output, whereas AUVs in constant current distributions typically need constant voltage power supply to them. Hence, the design of the desired constant voltage output AUV IPT system as part of the underwater current distribution requires the combined consideration of different IPT topologies and the techniques used in resonant converters in underwater current distribution. In addition, analysis of losses of such systems and coil optimizations for small AUVs with due considerations for seawater losses form an important area of research.

1.2.3 Small signal modeling for AUV IPT System in Constant Current Distribution

In addition to the modifications in steady-state operations, the constant current input resonant converter configuration results in markedly different dynamic characteristics, which are important to study for their stability analysis and control designs. This is identifiable from the small-signal models available for constant dc voltage and current input SRCs in literature [61, 67]. For IPT systems, models of dc voltage input SS IPT configurations are available, but they are not directly applicable for constant input current configurations [18, 68, 69]. A review of the modeling techniques and their careful applications towards

the constant input current configuration are required for small-signal model development of underwater IPT systems in constant current distribution.

1.3 Research Problem: Controls in EV DWPT

As explained earlier, the main target in an EV DWPT system is to regulate a desired power flow even in presence of dynamically changing misalignment between primary and secondary pads. These result in the change of parameters used in the basic power expressions in (1.3)-(3.10). Based on them, the typical requirements of controls in EV DWPT can be stipulated as

- Coupler designs which minimize fluctuation in flux linkage to the secondary,
- Compensation topologies to reduce the effects of change in coupling,
- Choice of control variable to achieve desired power flow with minimal control effort variations despite changes in coupling.

1.3.1 Control Performance of EV DWPT Systems

The existing works in EV DWPT present various coupler, converter and compensation topologies and different open-loop and closed loop control schemes to address the above targets. However, for a fair comparison of their performances, a system is to be designed with the the same input and output specifications and with comparable volume of IPT tanks, such that the effects of the topology selections in the controls stand out. This is typically not performed in the individual works and in the available review works. Hence this can be addressed to obtain a better comparative account of control performances of the existing EV DWPT systems.

1.3.2 Analysis of Communications in DWPT and Their Effects on Controls

Among different control implementations in DWPT, two popular approaches are primary side control and dual side control, both of which provide better closed loop stability if designed carefully. However, the power flow control requirement is typically decided by the

vehicle, which houses the secondary pads and associated electronics. Hence, these systems typically need communications between primary and secondary sides for effective controls. This leads to the dependency of these control schemes on the effectiveness of communications. The communication bandwidth can limit the power regulation capability in such configurations, which is not sufficiently addressed in literature. This is also an important area to address for improved power regulation in EV DWPT.

The next sections provide an overview of the relevant literature towards the solution of the above-mentioned research problems, leading to the specific contributions of this dissertation. Since both the areas of this dissertation focus on IPT systems, the review is presented from different aspects of an IPT system design. During the discussions about the topics, the applicability of them towards underwater IPT and EV DWPT are specified.

1.4 Review of Loss Characterizations and Optimizations

In an IPT system, the peak efficiency is dictated by the coupling factor k and coil intrinsic quality factors, expressed as

$$Q_p = \frac{\omega_s L_p}{R_p} \ , Q_s = \frac{\omega_s L_s}{R_s} \ , \tag{1.5}$$

where R_p and R_s denote the ac equivalent series resistance (ESR) of the coils. The peak efficiency under this condition is expressed as

$$\eta_{max} = \frac{k^2 Q_p Q_s}{(1+\sqrt{1+k^2 Q_p Q_s})^2} \approx 1 - \frac{2}{k\sqrt{Q_p Q_s}} \ , \tag{1.6}$$

which indicates that higher coupling and higher intrinsic quality factors lead to higher efficiency [70, 71]. Hence, the IPT coils are optimized to reduce ESRs at the frequency of operation, while maintaining a coupling factor as high as possible. Since all of these are dependent on operating frequency, coil dimensions and power transfer distance, it is

typically required to perform a rigorous multi-objective optimizations for the design of IPT systems.

1.4.1 Loss Characterizations and Optimizations In Underwater IPT

Typically ac resistance of the coils as per the characteristics of the selected litz wire is sufficient for in-air applications such as stationary or dynamic IPT of EVs. However the seawater losses are required to be considered for underwater applications, where the high-frequency magnetic field generates eddy currents in the partially conductive seawater. While these effects are possible to be replicated in finite element simulations (FEM) using a seawater environment around the coils, analytical expressions are useful in understanding the role of system parameters on such losses. The eddy losses are typically estimated from eddy current field integrals, and they are represented as additional coil ac resistances, termed as radiation resistance or eddy loss impedance [5, 8, 72–74].

Analytical expressions in forms of approximate integrals give more insights into such loss characterizations of coils in seawater, which is traditionally available only for a single coil and cylindrical coil immersed in infinite medium [75]. Similar model is used in [5] for circular coils, but it is not accurate as the variation of radii from turn to turn is not accounted for.

Underwater IPT systems are rarely connected to the power grid where frequencies are carefully monitored. Moreover, they vary in size and shape depending on the charging configurations and size of AUVs. Hence, no standard frequency of underwater IPT is yet published. Typically these systems are operated below 130 kHz to keep eddy current losses low [74], while a few works report usage of high frequency up to 465 kHz with three-phase coils [8]. However, higher power underwater IPT systems operate at mostly lower tens of kHz range [55]. Hence, optimizations for underwater IPT include selection of coil geometry and dimensions as per AUV dimensions and subsequent simulations to find designs achieving desired power transfer and efficiency at any suitable frequency of operation. Based on that, the designs meeting power transfer and efficiency criteria are selected.

1.4.2 Loss Characterizations and Optimizations In EV DWPT

While quality factor of the pads considering their ac losses are considered, typically EV DWPT topologies are designed targeting the SAE J2954 standard frequency of 85 kHz. The typical operating frequency range in EV DWPT is 20 kHz to 200 kHz [76, 77]. Typically more stress is given on optimization of the coupler shapes to obtain a flat mutual inductance profile [17], such that the effects of the moving vehicle can be minimized. In addition, η-α-Pareto optimization methods are available for EV DWPT systems, where thermal management is considered as part of the optimization work [78].

1.5 Review of Magnetic Couplers in IPT

As the coupler designs determine the peak efficiency of the IPT systems, their optimized design in greatly important. They widely vary in shape and dimensions for underwater IPT and EV DWPT, as per specific application requirements.

1.5.1 Couplers for Underwater IPT

The magnetic coupler configurations typically used in underwater IPT are shown in Fig. 1.7, which include circular [6], coaxial [7], three-phase [8], conical and double-EE core type coils [9]. Among these, the circular coil structure provides the best coupling and misalignment tolerance, because these coils have larger coupling area compared to the other types. The three-phase coil is formed using three cylindrical coils spatially arranged to generate three-phase flux. It has the advantage over the cylindrical coil used in the coaxial form, that the flux does not crowd towards the center of the AUV [8]. The conical shape is similar to the circular coils, whereas the reshaped EE coupler uses a different magnetic core shape rather than coil shape.

Due to the above reasons, most of the works in underwater IPT has focused on using circular coils, but the accurate loss models are typically not used [5, 6, 79].

1.5.2 Couplers for EV DWPT

Broadly, the EV DWPT coupler configurations can be classified in rail type structures

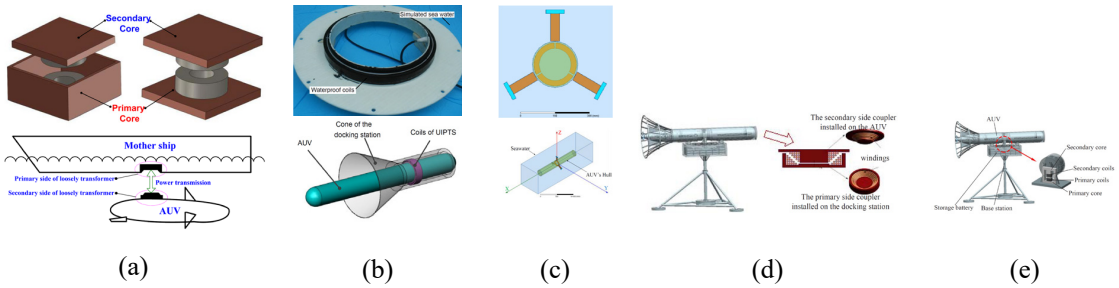

(a) (b) (c) (d) (e)

Fig. 1.7: Different coupler configurations in underwater IPT (a) circular [5, 6], (b) coaxial (cylindrical) [7], (c) three-phase [8], (d) conical [9], (e) reshaped EE [9].

as shown in Fig. 1.8 with alternate pole formations and separate pad-type systems as shown in Fig. 1.9.

The rail type couplers are mostly employed in the primary side. These include the E-type, W-type, U-type, I-type and S-type rails developed as part of the 1G to 6G OLEV generations [10, 12, 76, 80–83]. A few more recent developments have looked to improve on the effect of the zero coupling zones through couplers such as the I-type rail with d and q axis coils [14], n-type rail [16], π-type rail [15], I-type rail with multi-phase inverters [13] and E-type rail with E-type dual pick-up and multiphase inverter [11].

On the other hand, the separate pad structures are found on both primary and secondary side couplers. The primary couplers in such systems are constructed with multiple pads embedded within the roadway, to generate coupling with the secondary along the path of motion. Secondary sides typically employ similar pads, either single or multiple as per space availability, as the original equipment manufacturers (OEMs) prefer the smallest pads possible on the vehicles to reduce curb weights. The different pad shapes include circular, cylindrical (solenoidal), rectangular (including elongated ones), DD, DDQ and bipolar pads (BP) [2–4, 18–20, 22–25, 27–29, 36, 59, 77, 84–103]. To improve coupling during the transition zones of multiple DD pads, crossed and overlapped DD pad couplers are proposed [87, 92]. However, their practical application prospect is limited owing to installation and maintenance difficulties.

The rail-type structures typically energize all coils in the system through one inverter,

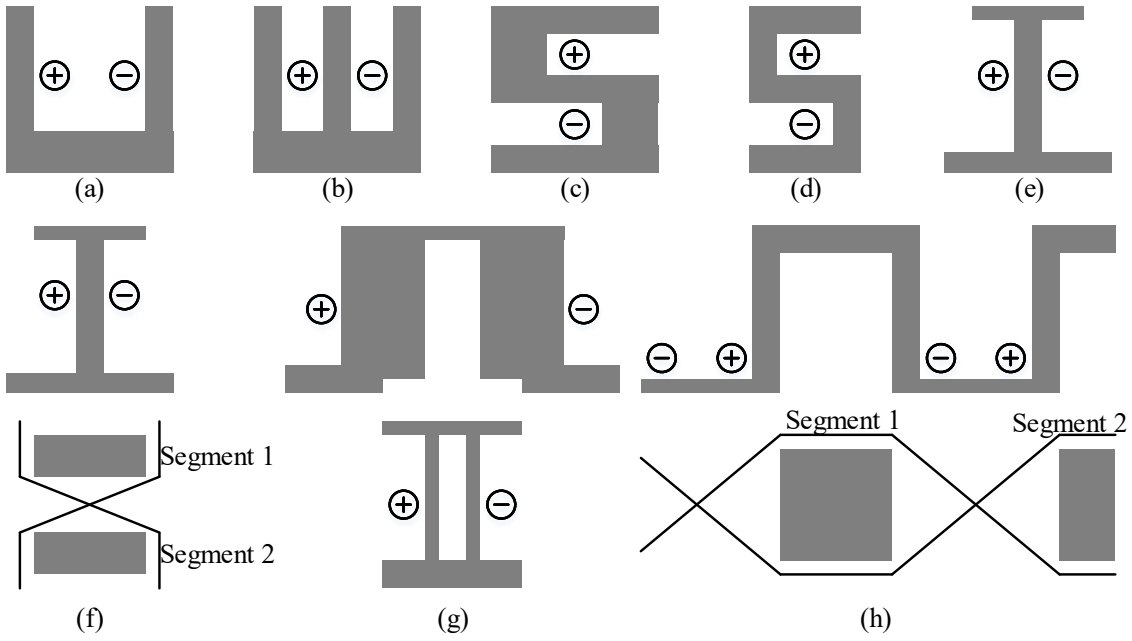

Fig. 1.8: Rail type primary couplers in EV DWPT (a) U-type [10], (b) E-type [11], (c) S-type [1], (d) Ultraslim S-type [12], (e) I-type [13], (f) I-type with DQ phases [14], (g) π-type [15], (h) n-type [16].

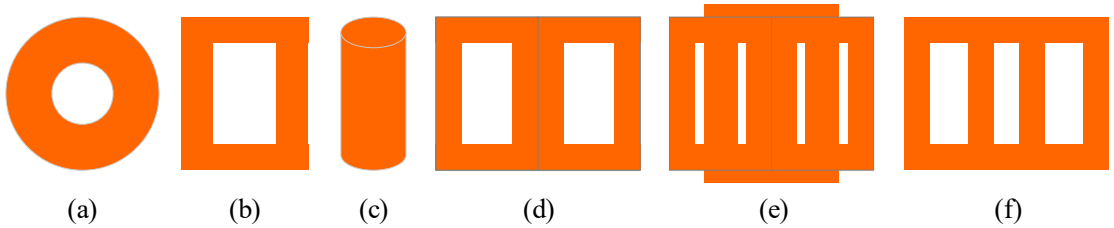

Fig. 1.9: Pad type primary couplers in EV DWPT (a) circular [17], (b) rectangular [18], (c) solenoid shaped/cylindrical [19, 20], (d) DD [21], (e) DDQ [22, 23], (f) Bipolar [24, 25].

leading to higher leakage flux and conduction losses. The multiple-pad structures improve on this, but they require segmentation controls to turn on the proper coils as per vehicle position. This also necessitates synchronization between the inverters using some sort of communications.

1.6 Review of Converter Topologies in IPT

The main converters in an IPT system include an inverter to drive the high-frequency current through the primary coil, and a rectifier on the secondary side to convert the high-frequency ac into dc for storage and other appliances. Typical inverter configurations in IPT include dc voltage input voltage-fed H-bridge [5, 14], current-fed H-bridge [26] and current-fed push-pull [27]. Among them, the first one is found in most of the works. Most rectifiers use diode rectifiers due to their simplicity of operation and no need of synchronization. However, synchronous rectifiers are used by some to improve efficiency while emulating the diode rectifier operation [93]. The circuit configurations of these typical inverter and rectifier topologies in IPT are shown in Fig. 1.10.

1.6.1 Converter Topologies in Underwater IPT and in Underwater Current Distribution

Among the above-mentioned common inverter configurations, the dc voltage input voltage-fed inverter and diode rectifiers are typically used in underwater IPT systems, as they typically do not explore into different converter topologies. The three-phase coils in [8] use three half-bridge legs from a constant dc voltage source, with each leg operation being similar to a voltage-fed H-bridge.

Among these options, the current-fed configurations can be used for a current distribution system shown in Fig. 1.6, such that additional conversion steps can be avoided. However, the square-wave currents in their output result in difficulty to achieve ZVS above certain voltage threshold. On the other hand, the resonant converters in underwater current distributions use the dc voltage-fed configuration shown in Fig. 1.10(a), but with a constant current input and a large input capacitor [62, 65]. As a result, they generate a

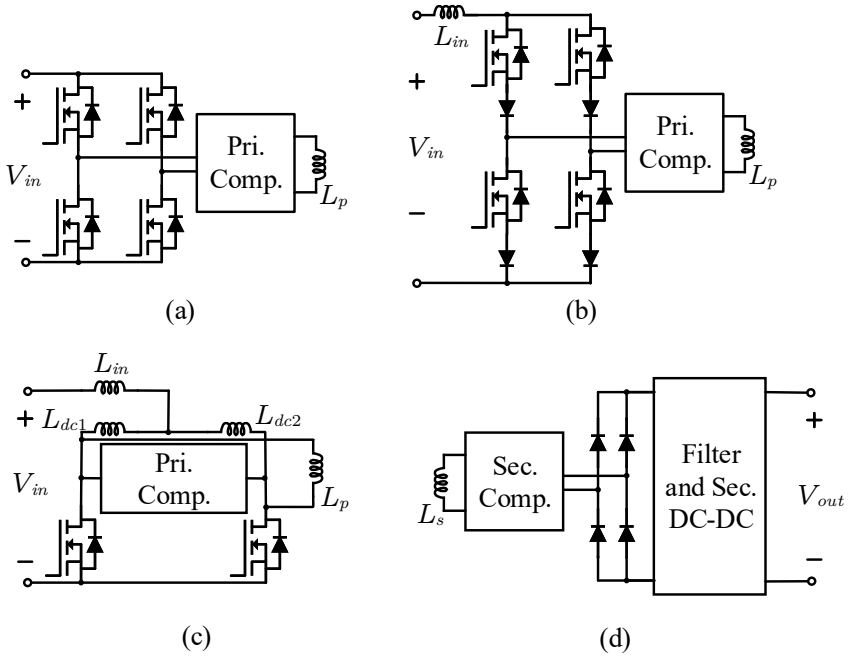

Fig. 1.10: Typical inverter and rectifier configurations in IPT (a) voltage-fed H-bridge inverter [5,14], (b) current-fed H-bridge inverter [26], (c) current-fed push-pull inverter [27], (d) diode rectifier with capacitive or LC filter [14,25].

quasi square-wave output voltage. The inverter output is connected to series or parallel resonant networks, tuned at or near the fundamental frequencies of the square wave voltages. As per the characteristics of the resonant network, shown in the frequency and time domains in Fig. 1.11, the inverter output currents are sinusoidal.

As a result, with proper design of the resonant network, the voltage-fed inverter is able to achieve ZVS, which is only possible for a narrow range with the current-fed inverter [65]. Moreover, this configuration leads to easier control of the inverter output current through the phase shift modulation (PSM) of the inverter [62,65] and ZVS over a wide load range with addition of an assisting half-bridge leg without significant loss in efficiency [104–106]. Hence the combination of voltage-fed inverter with constant current input, phase shift control and ZVS assistance leg form a suitable circuit which can be leveraged in the design of an underwater IPT system in constant current distribution.

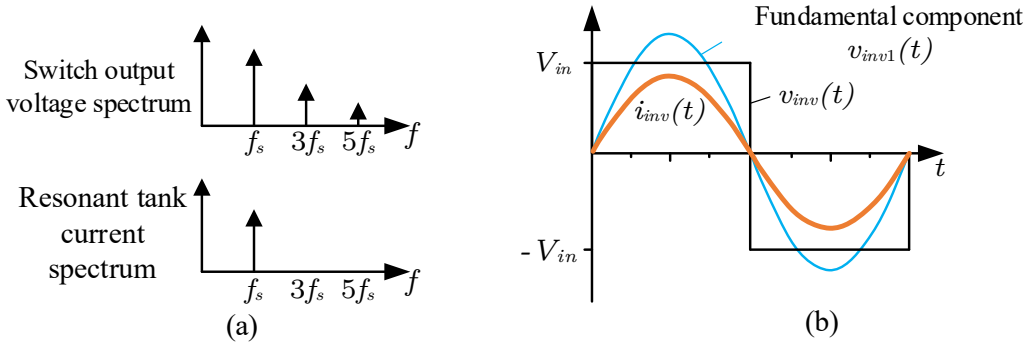

Fig. 1.11: Inverter output voltage and resonant tank current characteristics: (a) FFT spectrum, (b) time-domain waveform.

1.6.2 Topologies in EV DWPT

On the other hand, the schematic of an EV DWPT system in Fig. 1.4(b) shows that EV DWPT systems are typically driven from an ac/dc bus, through primary side converters and inverters. Often they are connected to the grid as well, similar to the stationary WPT systems for EV applications. On the vehicle side as well, there exist rectification and sometime additional converter stages to control interfacing to the batteries. Hence, in a typical EV DWPT system, conversions happen in four stages, involving a front-end converter, a high-frequency inverter, a rectifier and a back-end dc-dc converter, as shown in Fig. 1.12.

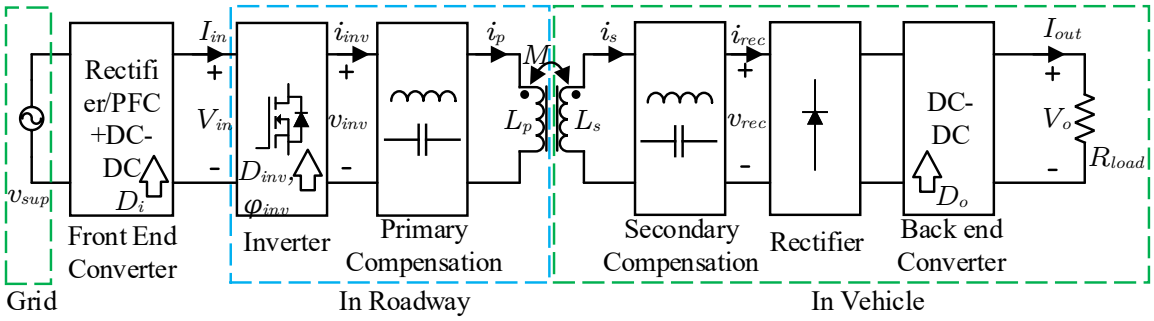

Fig. 1.12: Block-diagram representation of a DWPT system showing different stages and useful control handles.

Inverters

For the inverter stages, most of the inverter configurations shown in Fig. 1.10 are used, in addition to some multi-phase and single-phase, multi-coil drive inverters as shown in Fig. 1.13. Most of them use a single-phase inverter to drive each coil, and then synchronize switching instants through communications [20, 22, 83, 85]. Some works use a single-phase inverter to drive multiple coils [12, 28, 92]. The multi-phase inverters typically connect one pad between two successive legs, and switch them in proper sequence to turn different pads on and off [11, 13, 29, 102].

A comparative account of the different inverters in EV DWPT is presented in Table 1.1 to highlight their main features.

Rectifiers

Diode rectifiers are passive rectifiers and offer no control over power flow. Synchronous rectifiers emulate the same operation using MOSFETs instead of diodes for increasing efficiency. Most of the available DWPT works use diode rectifiers as they mostly use primary side control or controls through additional dc-dc converters on the secondary side [76]. Synchronous rectifiers do not offer additional operational benefits in DWPT systems, leading to only a few works using them [93].

Front-end Converters

The front-end converters include power factor correction (PFC) [10–12,15,23,76,88,101] and a subsequent buck or boost converter stages to control the DWPT stage primary pad current [14, 36, 93]. However most of the lab prototypes do not use them.

Back-end Converters

The back-end converters include buck, boost or buck-boost converters, depending on the secondary side compensation network [1,36]. [11,13,18,23–25,36,86,89–91,95,99]. Having a dc-dc converter following the rectifier on the secondary side help achieve secondary side power flow control with simpler rectifier structure. For this reason most of the available

Table 1.1: Inverter topologies in DWPT.

Inverter Topology	**Characteristics**
Single-phase full-bridge driving single coil [2, 101]	• Simplest inverter architecture, easy to control • Individual compensation networks with each inverter • High number of inverters and compensation network elements • Detection and communication required for segmentation control
Single-phase full-bridge driving multiple coils [22, 28, 84, 94]	• Lower inverter count than single coil drive configuration • Multiple coils and compensations in parallel - automatic detection and segmentation control • Multiple coils and compensations with selection switches - requires alignment detection for segmentation controls required • Multiple coils in series - reduced compensation network volume but larger leakage fields and losses
Multi-phase bridge [11, 13, 29, 102]	• Multi-phase pads or individual pads and compensations connected between each pair of legs • Lower device count compared to single-phase single coil drive • Communication not required for segmentation control • Soft switching scenarios require consideration as legs are switched for energizing different coils
Single-phase current-fed push-pull [27]	• Applicable with primary parallel compensation • Automatic tuning of switching frequency to tank resonant frequency • Requires considerations for soft-switching, switchable capacitors can be employed
Single-phase Class EF [97]	• Lower switch count • Load independent current output • Higher switch stress

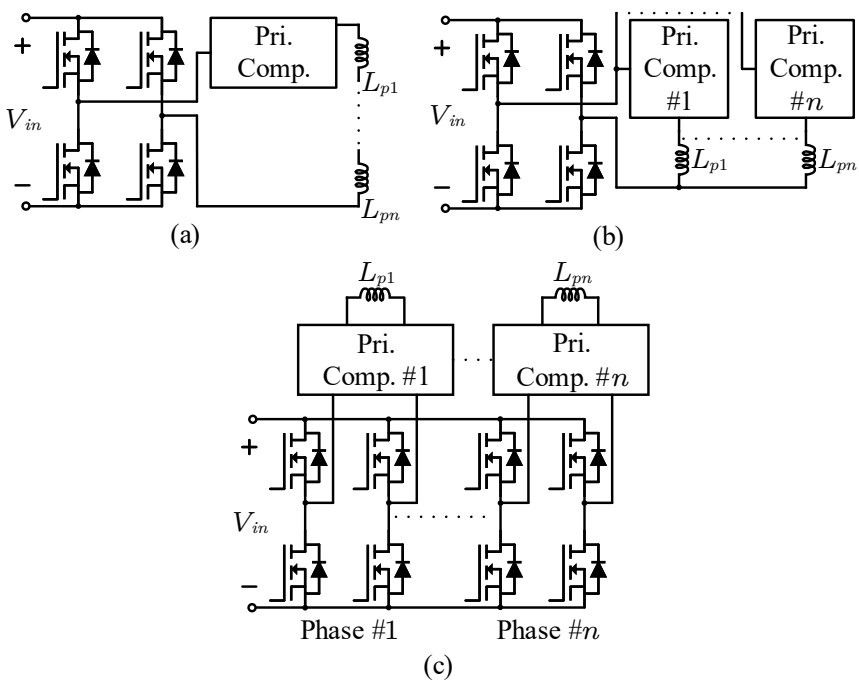

Fig. 1.13: Multiple coil drive inverters in EV DWPT (a) single-phase inverter driving multiple coils in series [12], (b) single-phase inverter driving multiple coils in parallel [28], (c) multi-phase inverter [13, 29].

works having secondary side control use them [11,13,18,23–25,36,86,89–91,95,99]. However this approach requires additional power electronics put on the vehicle side, which the vehicle manufacturers are trying to avoid.

1.7 Review of Compensation Topologies in IPT

IPT systems employ resonant compensation networks to compensate for the coil reactive power requirements. It leads to higher power transfer capability with reduced device stresses. The compensation networks also determine the constant voltage (CV) or constant current (CC) output characteristics and soft-switching behavior of the switches. Hence the compensation networks are chosen based on the frequency of operation, load-dependence requirements of the output quantities and the coil currents and soft-switching requirements of the switches.

An overview of resonant networks to constant voltage or current inputs to constant voltage or current output is shown in Fig. 1.14 [107]. The compensation topologies selected

in different IPT systems are governed by these basic configurations and their combinations.

The basic compensation topologies used in IPT systems include the second order LC compensation such as series-series (SS), series-parallel (SP), parallel-series (PS) and parallel-parallel (PP), as shown in Fig. 1.15. Characteristics of these topologies are documented in many available publications [1, 32, 108], which are provided in Table 1.2. The PS topology is excluded as it is not typically used.

Notably, the SS topology driven with a constant voltage results in constant output current, and driven with constant primary current produces constant voltage output. The dual of it happens with SP topology, which generates constant voltage output if driven from a constant voltage source, and constant current output if driven with constant primary current [108].

1.7.1 Compensation Topologies in Underwater IPT

In underwater IPT, mostly the SS and SP topologies are used, with the former finding the most usage [5, 8]. Typically these are driven from a constant voltage source to generate a constant current output to charge AUV batteries. However, the configuration needs to be modified for constant voltage power supply. The SS topology is also popular as it only requires capacitive filter whereas the SP topology needs an LC filter at the output.

To reduce system volume, some of the underwater IPT systems use no compensation on the secondary [7]. This is achievable in underwater IPT due to smaller gaps and higher couplings. However these are limited to lower power designs.

1.7.2 Compensation Topologies in EV DWPT

LC compensations

The LC compensation topologies discussed in Table 1.2 are also extensively used in EV DWPT, with again SS dominating due to its nice characteristics such as resistive reflected resistance at resonance. However, using SS topology in EV DWPT needs the primary

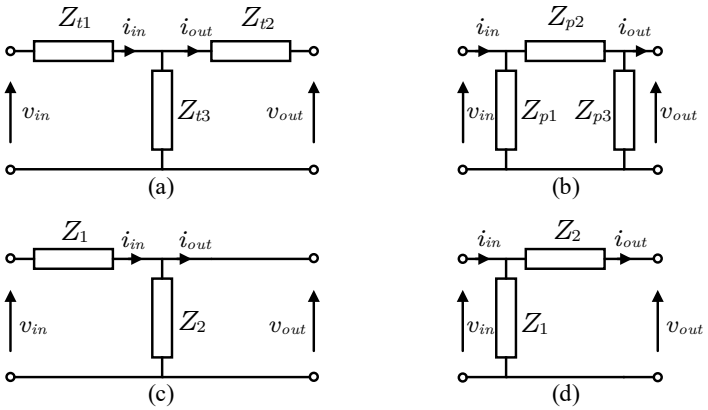

Fig. 1.14: Schematics of generalized resonant compensation tanks for (a) voltage-voltage, (b) current-current, (c) voltage-current and (d) current-voltage conversion.

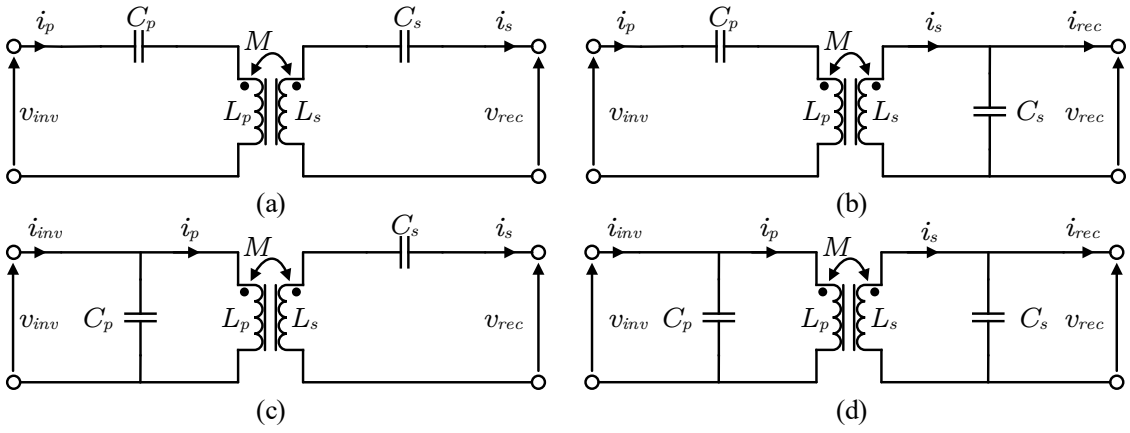

Fig. 1.15: Basic LC compensation topologies in IPT (a) series-series (SS), (b) series-parallel (SP), (c) parallel-series (PS), (d) parallel-Parallel (PP).

Table 1.2: Basic LC compensations in IPT.

Topologies	**Characteristics**
• Series-Series (SS) [14] • Series-Parallel (SP) [101] • Parallel-Parallel (PP) [23]	• Lower compensation tank volume • Simpler design, high reliability and efficiency • SS is inoperable at no-load, SP and PP are no-load capable • SS has resistive reflected impedance when operated at resonance, which is not available for the others • Higher tank harmonics with the series compensations • Voltage-fed inverter with series primaries, current-fed inverter with parallel primaries • SS good for high-power, SP and PP good for low to medium power

tank current to be controlled, which is typically performed through controlling the input voltage [12, 14], as in SS the tank current becomes high with lower coupling.

Higher order compensations

Due to this, in EV DWPT systems, typically a constant current throught the primary pads are desired, with mostly sinusoidal currents. For this, the higher order $LCCL$ based compensations were developed. These include primary side $LCCL$, LSP and 3-capacitor T topologies [3, 77, 93]. Primary $LCCL$ compensation helps generate a constant primary coil current when the inverter facing LC circuit is tuned at the frequency of operation. However, $LCCL$ compensation can also be optimized to obtain low-pulsation power flow profile with lagging power factor in the inverter, helping in soft-switching [2, 3].

Along with the higher order compensation on the primary, series compensation on the secondary is common to reflect a resistive impedance, with minimum volume in the vehicle [3, 29, 77, 84, 85, 87, 90, 93, 96]. Secondary parallel compensations are also found in a few applications focusing on filtering the secondary coil harmonics [24, 25]. However to make the secondary side immune to resonance shifts and protect the system from load open or short circuits, secondary side $LCCL$ topologies are developed [2, 4, 13, 18, 22, 89, 91, 92]. They also help in generating a constant output current which is often desired in battery charging applications. However secondary $LCCL$ compensation leads to lower power volume of vehicle side system and also achieves lower efficiencies compared to the other topologies. These topologies are shown in Fig. 1.16, and an overview of the features of these some of the higher order topologies are provided in Table 1.3.

A few recent works have looked to utilize the advantages of $LCCL$-$LCCL$ and SS in developing series and parallel hybrid compensation topologies, shown in Fig. 1.17 [21, 30]. These are used with DD or bipolar pads on both sides, where two coils per pad are available. The series hybrid compensation topology demonstrates better performance with misalignments in keeping flat power transfer profile. These topologies do not need the additional inductors in the $LCCL$ compensation designs, leading to higher power densities.

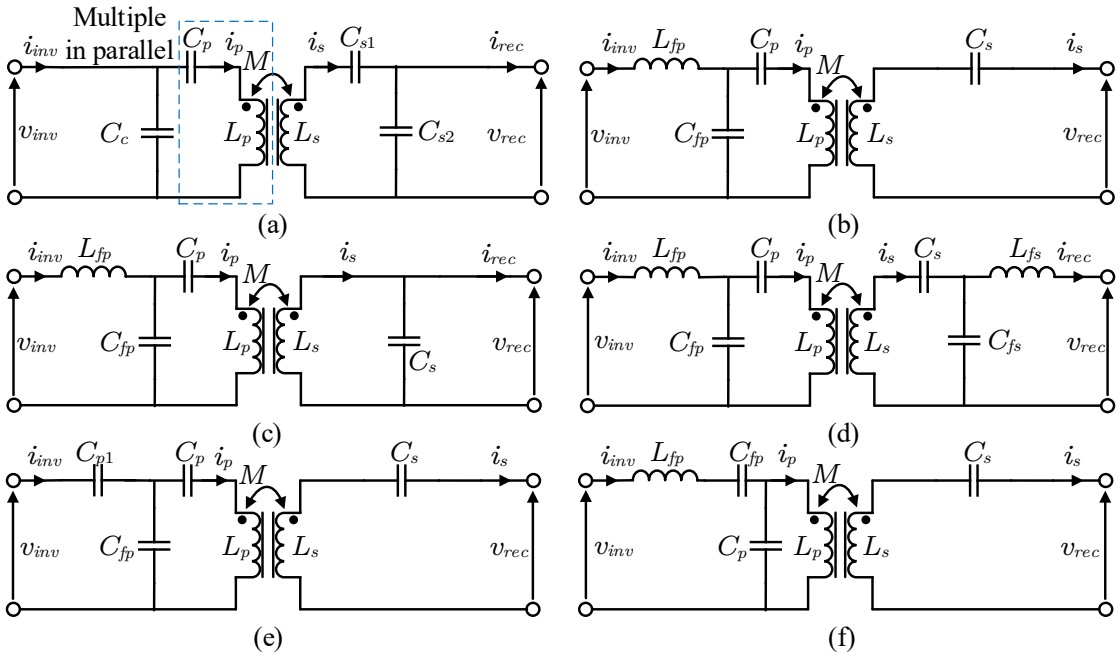

Fig. 1.16: Higher order compensation topologies in EV DWPT (a) *LCC-LCC*, (b) *LCCL*-series, (c) *LCCL*-parallel, (d) *LCCL-LCCL*, (e) *CCC-T*, (f) LSP-S.

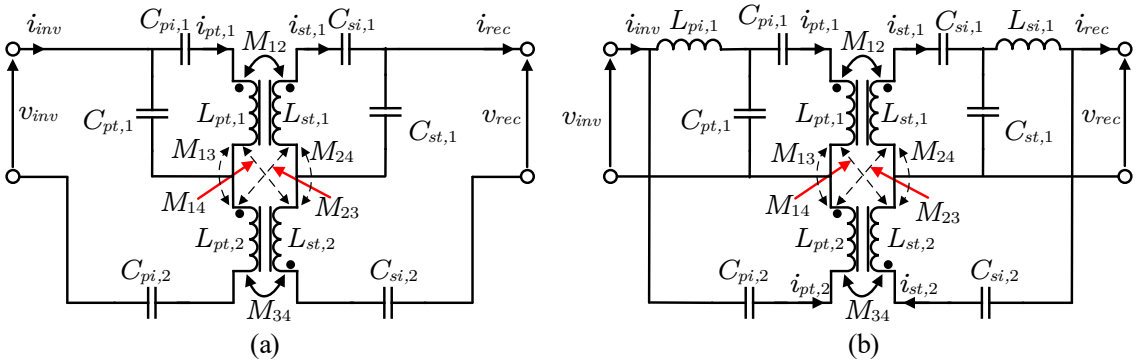

Fig. 1.17: Hybrid compensation topologies in EV DWPT (a) series hybrid (SH) [21], (b) parallel hybrid (PH) [30].

Table 1.3: Higher-order and Re-configurable Compensations used in EV DWPT.

Type	**Topologies**	**Characteristics**
Higher order	• *LCCL*-series (*LCCL*-S) [3] • *LCCL*-parallel (*LCCL*-P) [25] • *LCCL-LCCL* [4] • *CCC-T* [77] • LSP-S [93] • *LCC-LCC* [28] • Series hybrid (SH) [21] • Parallel hybrid (PH) [30]	• Higher order filtering of current harmonics • Improved control over primary current • High reliability and high design flexibility • Higher compensation tank volume and lower efficiency compared to *LC* compensations • Best applied for low to medium power applications
Re-configurable	• Primary switched capacitor network [27] • Multiplexed primary *LCC* networks with component redistribution [15] • Multi-parallel priary *LCC* with auxiliary *LCC* network [22] • Switched primary *LCC* and *LCCL*/S mode switched secondary compensation [94] • SP-SP^2 mode switched compensation [103]	• Soft-switching control through switched primary capacitors • Circuit based control of segmentation and primary current • CC/CV output mode control with *LCC*/S switched mode • Encrypted WPT with SP-SP^2 mode switched operation

Re-configurable compensations

The configurable compensation networks are developed by researchers to provide additional circuit-based controls to the DWPT systems. Key features of the re-configurable compensation networks are presented in Table 1.3. These systems help in achieving power flow control [22], control of the automatic switching of coils based on alignment [28, 84] or compensation modes [94, 98]through additional circuits. Hence they achieve improved open-loop performance with additional features. However they make the hardware more bulky and complicated to operate.

1.8 Review of Small-signal Modeling of Resonant Converters and IPT Systems

Typical small-signal modeling techniques for resonant systems include generalized state-space averaging (GSSA) [18, 109], extended describing functions (EDF) [69, 110, 111] and sampled data modeling [112]. In the GSSA method involve complicated mathematics associated with large matrices corresponding to taking each inductor current and capacitor voltage as state variables. Hence, even though experimentally proven to be quite accurate, they provide limited insight into the system. Similar argument is also applicable to the sampled data models for resonant converters, as the models get too complex [112]. The EDF method takes into account the resonant tank harmonics and is the only available method to account for them in the area of small-signal analysis of resonant systems. However it is not applicable to phase-shift controlled systems such as the resonant systems in underwater current distribution. Moreover, these modeling techniques do not follow a circuit analysis oriented method that can provide more insight into resonant systems.

On the other hand, the newer technique of small-signal phasor modeling [61,67,68,113] provides an option to transform the resonant network to a phasor domain, which allow circuit operation to perform small-signal analysis through circuit operations. As a result this technique is becoming more popular and its application is growing into the analysis of systems such as series resonant converters and constant voltage input SS IPT systems. Hence a detailed overview of this technique is presented here as the target system is an IPT system to be developed for underwater current distribution.

The phasor model describes a sinusoidal switching frequency variable as a static envelope, such that the rotational property goes away. Hence any ac quantity with switching frequency ω_s is represented as

$$x(t) \Rightarrow \Re[\vec{x}e^{j\omega_s t}] \ . \tag{1.7}$$

This demonstrates that, in a system where switching frequency is constant, this technique results in a time-invariant model. Hence this is very useful for phase-shift controlled resonant systems in underwater current distribution.

Expressions for basic circuit elements, such as the resistor, inductor, capacitor, H-bridge inverter and full-bridge rectifier are available from existing works, which are put forward here as a reference. The models for these components are shown in Fig. 1.18, which correspond to the parameters as

$$\vec{s}_p = \frac{\vec{v}_{AB}}{V_{in}} = \frac{2\sqrt{2}}{\pi} \sin\left(\frac{\varphi_{AB}}{2}\right) \ , \tag{1.8}$$

$$\vec{s}_s = \frac{V_{out}}{\vec{v}_{DE}} = \frac{2\sqrt{2}}{\pi} \ , \tag{1.9}$$

$$\vec{v}_l = L\frac{d\vec{i}_l}{dt} + j\omega_s L\vec{i}_l \ , \tag{1.10}$$

$$\vec{i}_c = C\frac{d\vec{v}_c}{dt} + j\omega_s C\vec{v}_c \ . \tag{1.11}$$

$$\tag{1.12}$$

Later in the dissertation, these models are appropriately modified for the designed IPT system to develop required small-signal models.

1.9 Review of Control Objectives and Implementations in EV DWPT

The magnetic coupler design, choice of compensation network and power electronic converter topology for any WPT system decide the steady-state operation of the system.

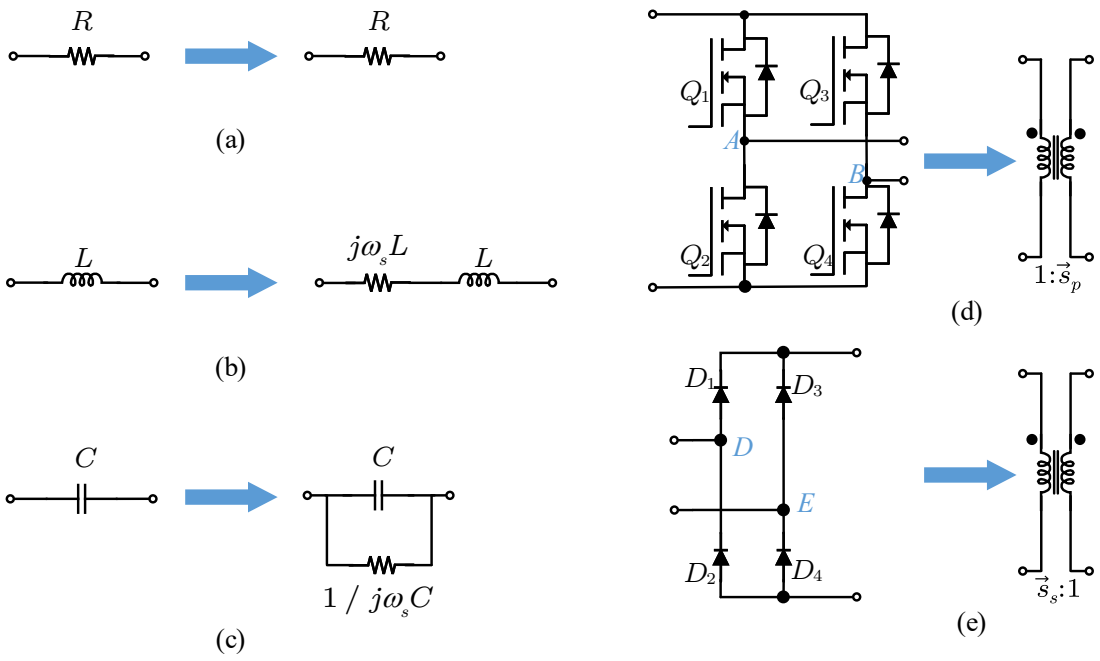

Fig. 1.18: Phasor transformation of basic circuit elements in a resonant converter system.

However load, coupling and parametric changes in EV DWPT systems lead to deviations from the ideal design conditions. Control systems are required to regulate power flow under such conditions. While power flow control is the main objective in EV DWPT systems, the other objectives include segmentation, soft-switching and compensation modes which help in important operating aspects of them. A block diagram of different control objectives in DWPT is shown in Fig. 1.19, which include power flow control, segmentation control, ZVS control and compensation mode control. The first one is the main objective, while the other ones are auxiliary ones helping to achieve better power flow control reliably, through open-loop or closed-loop configurations.

Existing EV DWPT works include open-loop or closed loop controlled systems and their implementations include single or dual-side schemes. While power flow control and mode controls are available on both primary or secondary systems, segmentation and soft-switching controls are mostly used on the primary side.

The features of different open-loop and closed-loop control implementations of power flow control and segmentation control are provided in Table 1.4.

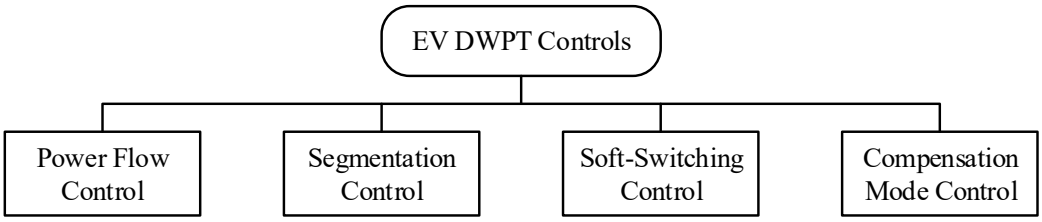

Fig. 1.19: Block-diagram of control objectives in DWPT.

Table 1.4: Open loop power flow control methods in EV DWPT.

Methods	**Characteristics**
• Large secondary pads and *LCCL*-*LCCL* compensation [4]	
• Optimized *LCCL*-S compensation with lagging primary phase [3]	• Mostly flat power transfer profile without feedback
• Crossed DD primary pads with double-coil excitation [92]	• Circuit based power regulation, faster response
• n-type rail and DDQ secondary [16]	• Typically larger or complicated pads, often impractical
• *CCC*-*T* topology with the primary acting as series compensation above resonance [77]	• Optimization of pads and compensations necessary
• Class EF inverter and Class D rectifier	• Not always interoperable with different topologies and air gaps
• Combining the advantages of *LCCL* and series compensation on both sides and DD pads [21, 30]	

Table 1.5: Closed loop power flow control methods in EV DWPT.

Methods	**Characteristics**
• Front-end converter control [12, 36, 76, 93] • Inverter duty ratio control [96, 99, 101] • Inverter frequency control [101] • Inverter phase shift control [13, 18, 87, 89–91] • Regulation through auxiliary *LCC* network [22] • Secondary dc-dc converter control [11, 13, 18, 23–25, 36, 86, 89–91, 99] • Dual-side control [13, 18, 89–91, 99]	• Regulation of primary coil current or secondary quality factor • High reliability • Feedback through communications for primary or dual side controls might degrade reliability • System overdesign necessary for control actions

Table 1.6: Open loop segmentation control methods in EV DWPT.

Methods	**Characteristics**
• Reflexive field containment [28] • Circuit based Autotuning [84] • Constant current driven through paralleled *LCCL* compensated coils [22]	• Circuit-based automatic switching of coils based on EV positions • Communication requirements can be avoided • Cross-coupling among coils and change in coil self-inductances can cause reliability problems • Additional power loss in series or parallel connected coils carrying low but non-zero currents • Functions well for a very few topologies, not operable with other ones

Table 1.7: Closed loop segmentation control methods in EV DWPT.

Methods	Characteristics
• Detection systems [89, 91] • Monitoring free resonance current [25] • Primary current monitoring [20, 85] • Switch boxes with cross-segmented rail [83] • Multi-phase inverter phase control [29] • TMR sensors on secondary [100] • Secondary side power allocation control [95] • Ferrite core counter and FPID message [82]	• Better control over segmentation and current through inactive pads • The free-resonant monitoring avoids additional hardware for segmentation control - easiest for interoperability • Secondary segmentation controls less practical, often DDQ coils are sufficient • Reliability depends on sensors • Communicatons are required between different inverter units, which are reduced for multi-phase architectures

1.9.1 Open-loop Control

These EV DWPT works rely on circuit and magnetic designs to obtain a smooth power transfer profile, by driving the inverter at a fixed phase angle (or duty ratio). The major aspects of them include primary and secondary pad designs, choice of compensation networks and converter topologies to regulate desired power flow. A few notable ones include usage of large pads [4], crossed DD pads [92], overlapped DD pads [87], optimized *LCCL*-S [3], multiple coil driving inverter [59] and hybrid compensations [21, 30].

Open-loop segmentation control is achieved in the field focusing technique [28] and the autotuning control arragement in [84]. A hardware-based detection of pads for interoperability is presented in [25] which can achieve segmentation without additional circuitry. The detection systems also enable precise control of segmentation, but they typically involve additional hardware [89, 91].

1.9.2 Primary Side Control

The primary side controlled DWPT systems typically employ feedback based closed

loop architecture on the primary subsystem, while having a passive secondary. Primary side power flow control helps changing the effective VA of the primary coil (S_{pri}), such that even with variation in coupling (k), a mostly constant power flow is achieved as per (1.4). Control is mostly implemented in the front-end converters [12, 14, 76] or in the inverter stages [10, 19, 87, 96, 101, 102]. Inverter phase shift control or duty cycle control typically introduce soft-switching and harmonic problems in the circuit, but they are quite popular in lab prototypes which do not use any front end converters. Achieving primary side control in the front-end converters help in soft-switching in the DWPT stages.

DWPT works employing active segmentation control on the primary use single-phase [2, 22, 92] or multi-phase inverter configuration [29]. In single-phase configurations, single inverter driving single or multiple coils and tanks are used [2, 22, 92]. The double-coupled system provides a way of effectively synchronizing a large number of inverters together, but at the cost of added wireless stages and complexities of implementation [114]. The important techniques of turning on/off correct coils include monitoring of switch-on transient current, determining transition instant through a pulsation control pulse, switch boxes with cross-segmented rail and mode controls through free resonance and impedance control on primary tank [20, 22, 25, 83, 85].

Soft switching control using active method is used with switchable capacitors and push-pull inverter for a current-fed input in the work by A. Kamineni *et al.* [27]. It helps overcome the soft-switching difficulties in current-fed inverter configurations against mistuning in the system.

The primary side controls typically require communication between the primary and secondary, which is typically avoided by sensing primary side quantities. However primary side segmentation control and soft-switching control are indispensable in DWPT.

1.9.3 Secondary Side Control

These systems only use secondary side control from in the vehicle. The existing works for DWPT with secondary side power flow control mostly employ dc-dc converters following the DWPT stages [23–25, 86, 95]. The variation of secondary dc-dc converter duty ratios

regulate power flow through by modifying the loaded quality factors of the secondary coils (Q_{sl}) with variation in k, as per (1.4). The primary sides are operated in open-loop, often driving a constant current through the primary coils/rails. Hence, typically no communication is necessary between the primary and secondary subsystems.

Very few works use segmentation control on the secondary side, which employ multiple receivers. The methods include TMR sensor based position detection and ferrite core counter and FPID message based alignment detection [82,100]. These methods however are only suitable for large vehicles where multiple pad receiver might be feasible.

Mode switching controls are used in the secondary side for CC/CV mode charging and encrypted DWPT purposes. The former is achieved by switching the secondary between *LCCL* and series mode [94], and the latter is achieved by switching between SP and SP^2 modes using a configurable capacitor array [98].

1.9.4 Both Side Control

These works include control actions on both primary and secondary sides. The primary controls include the front-end converter controls [11,36,93], inverter phase shift or duty cycle controls [13,18,90,91,99] and multi-phase inverter control [13]. The secondary side controls use buck or boost converter duty ratio controls [11, 18, 36, 89, 91, 99]. Dual-loop control is also present [18]. Communications are typically indispensable in them to keep coordination between primary and secondary controls.

1.9.5 Communications in DWPT Controls

Communications in DWPT are essential for reliable operation between the roadway and the vehicle mounted pads. Communications are used not only to communicate operation related data, but also used in some of the control loop designs. In fact, most of the high power DWPT systems demonstrating primary side or dual side power flow control use communications [10, 89, 90, 99, 101].

The typical communication protocols in EV IPT applications include FM, WiMax, Cellular, DSRC, Satellite and Bluetooth [91]. Among these, high data rates are available

with Satellite, Bluetooth and DSRC,, while the least latencies are available with Bluetooth, DSRC and FM.

1.10 Contributions and Organization of the Dissertation

1.10.1 Overview of the Contributions

Based on the review of loss modelings and optimizations of underwater IPT systems, a simplified, approximate integral based analytical model is derived for modeling of eddy losses with circular spiral coils. The model considers the effect of unequal radii of turns in such coils and represents the losses as an additional ac ESR of the coil. The model is also used to optimize an IPT system for small size and higher frequency of operation than the typical range found in literature.

Through the review presented in the above sections, it can be found that the voltage-fed inverter topology with a constant current source helps in generating a constant current at the inverter output controlled through the inverter phase shift and maintain ZVS over wide load range with the help of simple assistance circuits. On the other hand, the review of IPT compensation topologies demonstrated that under such condition, SS and *LCCL*-*LCCL* compensations can lead to constant voltage characteristics on the output. Based on this, the SS topology is developed for the AUV IPT system design in underwater current distribution, due to its inherent advantage of lower system volume. Two versions of the same topology are proposed, one with a current-boost transformer on the primary tank and the other without it, to consider for different input current ranges to generate the same output voltage. For both topologies, steady-state analysis and design considerations are developed to find out operating conditions to maintain such constant voltage characteristics in a practical design over a wide load range.

In addition, small-signal modeling is performed for the proposed IPT topologies for underwater current distribution to gain insights into the dynamic behavior of the system in terms of their parameters. Based on the model, the critical pole and zero locations are identified and a typical control loop design is provided. The small-signal model is also

validated for the transformer-based version through simulations and experiments.

The above developments are experimentally validated in setups up to 1 kW power ratings. A conventional dc voltage input system operating with 48 V input and 255 kHz frequency is used to validate the eddy loss models and optimizations. On the other hand, two prototypes, one operable up to 330 W and the other one up to 1 kW, operating with 1 A constant dc current input and 250 kHz frequency were used to validate the steady-state characteristics, design considerations and dynamic characteristics of the constant dc current input underwater IPT systems.

On the other hand, the overview of couplers, converters, compensations, control objectives and their implementations presented for EV DWPT are used to find the contributions of these stages towards improvement of control performances. Based on that, it is identified that comparisons between control performances achieved with different compensation topologies and different control handles are important to achieve it. To perform the comparisons, an example 50 kW EV DWPT system with identical coils are designed with different compensation topologies and different primary and secondary side control handles. Then their control performances are compared through key performance metrics, which can be used for any future IPT systems for judging their control effectiveness.

The effect of communications in DWPT controls is also analyzed through the knowledge of delays associated with existing communication protocols. A relation is derived between rate of change of mutual inductance and vehicle speed, which is used for existing coupler designs and compensation topologies to compare power regulation effectiveness in presence of communication latency, the outcomes of which can be used in future EV DWPT system designs with communication dependent controls.

1.10.2 Organization of the Dissertation

The rest of the dissertation is organized as follows:

The eddy loss model for circular spiral shaped coils and its application towards the analytical optimization of an underwater IPT system considering air-core coils immersed in seawater are presented in Chapter 2.

The steady-state analysis of the conventional constant dc voltage input underwater IPT topology and the two proposed implementations of the constant dc current input underwater IPT topologies are presented in Chapter 3. It is shown there how a constant current output is obtained in the constant voltage input topology and how a constant voltage output is obtained from the constant dc current input topologies. Moreover, analysis of effects of tank ESRs and tank mistuning due to coil misalignment for the proposed constant dc current input topologies are also presented here, paving way for the design considerations.

Design considerations and their applications for all the above topologies are presented in Chapter 4. For the voltage input topology, the design is presented only for the coils as per the analytical optimizations presented in Chapter 2 and the corresponding design of the tank components and inverter/rectifier devices. As the same setup is used for tests with the transformer-based constant current input IPT system, the design of the current-boost transformer and the choice of power range for sinusoidal operation of the tank currents are discussed for this topology. Further, full design considerations including current-to-voltage conversion ratio under nominal and misaligned conditions, total VA ratings of the tank, discontinuous conduction mode (DCM) of the rectifier, output power condition under misalignment and component sizing are presented along with its application towards the design of a 1 kW prototype for the transformer-less constant dc current input topology.

The small-signal modeling of the constant dc current input underwater IPT topologies are presented in Chapter 5 using the small-signal phasor modeling technique. It also presents how the model is used to gain insights into the dc gain and pole-zero locations in terms of the system parameters and a typical control scheme.

All experimental results for the designed underwater IPT systems are presented in Chapter 6. This includes a loss-distribution analysis for the voltage input IPT system for validation of the optimization procedure, steady-state waveforms and plots for both the implementations of the constant current input topologies, steady-state results and plots for the misaligned conditions for the transformer-less topology and simulation and experimental validation of the small-signal model for the transformer-based topology.

The focus shifts to the control analysis of EV DWPT systems in Chapter 7, which presents a critical analysis of the different stages of DWPT systems in their controls. It brings out that choice of compensation topologies and control handles are key to design of stable DWPT systems with simplified couplers and other hardware. Moreover, the analytical expressions for these topologies are listed here.

Based on the analytical expressions in Chapter 7, comparison of control performances and effects of communication od DWPT controls are presented in Chapter 8. The control performance comparison results of different DWPT compensation topologies and control handles are presented through the proposal of the performance metrics. The analysis and results for the communication delays on DWPT controls are also presented in this chapter, for different coupler configurations and different compensation topologies. Based on these comparative analysis, a few recommendations are made for guiding future DWPT research.

The dissertation is concluded in Chapter 9 with a summary of the contributions and an overview of the future research opportunities coming out of it.

CHAPTER 2

Eddy Current Loss Models and Optimizations for Spiral Coils in Underwater IPT System

To present the underwater loss model of the circular spiral coils, their equivalent representations are considered. The loss components for proximity and skin effects are considered from available works and from litz wire constructions [115, 116]. Then the single-turn coil radiation resistance expression from [75] is carefully extended for the circular spiral coils considering unequal radii of the turns.

2.1 Analytical Model of Litz Wire Based Spiral Coils

2.1.1 Spiral Coil Models and Dimensions

An N-turn spiral coil is shown in Fig. 2.1(a) with its important dimensions such as inner radius r_{in}, outer radius r_{out} and wire diameter d_w marked. The center to center distance between two adjacent turns is defined as the pitch. The pitch of each turn can be equal or unequal [117]. From Fig. 2.1(a) the pitch for the n^{th} turn from the inner side (p_n), representing the center to center distance of the n^{th} turn and the next, $(n+1)^{th}$ turn, as

$$p_n = r_{n+1} - r_n \ . \tag{2.1}$$

Hence an N-turn coil has (N-1) pitches, and the dimensional relation for the N-turn coil is obtained as

$$r_{out} = r_{in} + \sum_{i=1}^{N-1} p_i \ . \tag{2.2}$$

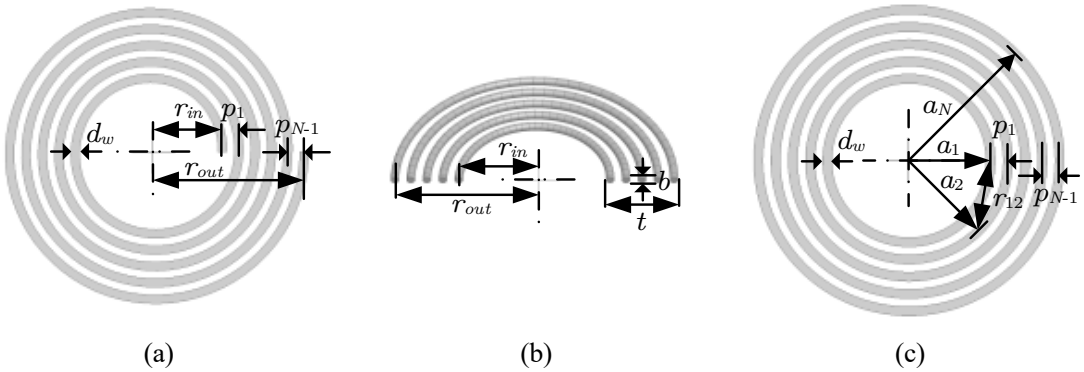

(a) (b) (c)

Fig. 2.1: Diagrams of spiral coils and its model with important dimensions (a) Top view of spiral coil, (b) Side view of spiral coil, (c) Concentric circle model of spiral coil.

Its cross-section model is shown in Fig. 2.1(b), which shows the width b and thickness t of the coil. Using the dimensions introduced earlier, the expressions for b and t for a single-layer circular coil are obtained as

$$b = d_w \ , \tag{2.3}$$

$$t = d_w + \sum_{i=1}^{N-1} p_i \ . \tag{2.4}$$

As it is difficult to work with the constantly changing radii of the spiral coil turns, an N-turn coil is typically approximated as the combination of N concentric circular conductors [118]. This is also found applicable in the present work for computing the impedance between the turns in presence of eddy current fields. The model is shown in Fig. 2.1(c), with the important dimensions marked in the figure. Each turn in the model is approximated as a circle with the radius equal to the average of its inner and outer radii. With the aforementioned definition of the pitch of a turn, the radius of the n^{th} turn of the model (a_n) can be obtained as

$$a_n = \frac{r_n + r_{n+1}}{2} = r_n + \frac{p_n}{2} \ . \tag{2.5}$$

2.1.2 Loss Model Development of a Litz Wire Based Spiral Coil in Seawater

The main properties of a litz wire based spiral coil for underwater IPT applications include its ac resistance and inductance. The total ac resistance of an underwater IPT coil consists three loss components, the skin effect losses, the proximity effect losses and the seawater eddy current losses, typically represented as additional ac losses of the coil [72]. Detailed modeling of litz wire coils for ac resistance estimation [119] as well as approximate methods [115] are available in literature. However, with a properly selected litz wire, losses due to skin effect in the coil and proximity effect within the winding strands become negligible [115]. Considering this, the model of a spiral coil based underwater IPT system is required to have expressions for the following components:

a. AC resistance of each coil due to proximity effect between the coil turns (R_{pro}) [115]

b. Eddy loss resistance in seawater for each coil (R_{eddy}) [5, 75]

c. Self-inductance of each coil (L)

d. Mutual inductance between the coils (M)

The equivalent circuit model for one coil is shown in Fig. 2.2, which shows the above components, except for the mutual inductance which exists between each pair of coil in the IPT system. Each underwater coil also undergoes negligible modification in its inductance, expressed in the form of the correction reactance ($X_{cor,sea}$) in [75]. However this modification is neglected in the present work as it was shown to have negligible value and negligible variation with frequency.

The following subsections provide the expressions of the equivalent circuit model components shown in Fig. 2.2, which will be later used in analytical optimization.

Proximity Resistance Expressions

The proximity losses in a litz wire based coil are dependent on the litz wire constructions and they are present for both in-air and underwater operations. An approximate expression for R_{pro} is available in [115] for an N-turn spiral coil, and hence it is directly used in the

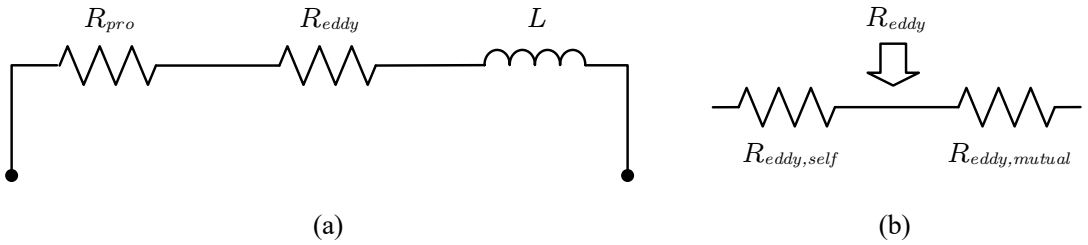

Fig. 2.2: Equivalent circuit representation of a litz wire spiral coil for underwater IPT system (a) Full model, (b) Components of the eddy loss resistance.

model in the present work. Equations (2.6) and (2.7) show the necessary expressions with the parameters of the coil as per Fig. 2.1(a) and Fig. 2.1(b):

$$R_{dc} = N\rho\left(\frac{2\pi r_{avg}}{A_w}\right)1.06^{N_b}1.03^{N_c}\ , \tag{2.6}$$

$$R_{pro} = R_{dc}(1 + 409.6NN_{st}d_{st}^4nBf_s^2)\ , \tag{2.7}$$

where ρ is the resistivity of copper (in Ω m), r_{avg} is the average radius of the coil (in m), given by $(r_{in}+r_{out})/2$, A_w is the winding area (in m^2), given by $N_{st}\pi(d_{st}/2)^2$, N_{st} is the number of strands in the litz wire, d_{st} is the strand diameter of the litz wire (in m), N_b is the number of bunching operation in the litz wire, N_c is the number of cabling operation in litz wire, f_s is the operating frequency (in Hz). The factors n and B are calculated using the method in [47]. All litz wire related parameters are obtained from the supplier's product selection guide [116].

Eddy Loss Resistance Expressions

The eddy loss resistance accounts for the additional power losses in the coil in order to maintain the coil current against the fields produced by the eddy currents in seawater. It properly represents the contributions of the seawater conductivity in the power losses. The expression of R_{eddy} of a single insulated circular conductor ($R_{eddy,a}$) in an infinite conductive medium is presented in [75], which shows that $R_{eddy,a}$ increases exponentially

with frequency. Since this component is directly related to the eddy current losses, its exact estimation for an N-turn spiral coil is important in optimizing such coils for small size with higher operating frequencies.

The expression of R_{eddy} for the single-turn thinly insulated conductor from [75] is

$$R_{eddy,a} = \omega_s \mu a \left[\frac{4}{3}(\beta a)^2 - \frac{\pi}{3}(\beta a)^3 + \frac{2\pi}{15}(\beta a)^5 - \cdots \right] , \tag{2.8}$$

where ω_s is the angular frequency of the loop current (in rad/s), given by $2\pi f_s$, μ is the permeability of the conductive medium (in H/m), a is the radius of the conducting loop (in m), β is the imaginary part of the complex propagation constant of the conductive medium, given by $\sqrt{\omega_s \mu \sigma/2}$ and σ is the electrical conductivity of the infinite medium (in S/m).

For a coil immersed in seawater, the infinite conductive medium is the saline water, whose permeability is approximately equivalent to that of air ($\mu_{sea} \approx \mu_0 = 4\pi \times 10^{-7}$H/m). The conductivity of seawater σ varies with the salinity and temperature [120]. For the loss models and optimizations presented in this work, the nominal conductivity at room temperature is considered, which is approximately obtained from the graphs to be around 5 S/m [120].

To find the expression of eddy loss resistance for the coil, the concentric circle model in Fig. 2.1(c) is considered. The eddy loss resistance of each circular turn consists of its self eddy loss resistance and its mutual eddy loss resistance [31]. The self eddy loss resistance of one circular conductor ($R_{eddy,self,n}$ for the n^{th} turn) represents the power loss caused by the eddy currents produced by its own electromagnetic field. On the other hand the mutual eddy loss resistance of the circular conductor ($R_{eddy,mut,n}$ for the n^{th} turn) represents the total power loss caused in the it owing to the eddy currents generated by the other circular conductors in the coil.

As per the definition, Kraichman's formula [75] essentially gives the expression for the self eddy loss resistance of each turn. So the expression for the n^{th} turn can be directly obtained using (2.8), and the total self eddy loss resistance of the coil is obtained by summing

up for all the turns, as

$$R_{eddy,self} = \sum_{n=1}^{N} \omega_s \mu_0 a_n \left[\frac{4}{3}(\beta a_n)^2 - \frac{\pi}{3}(\beta a_n)^3 + \frac{2\pi}{15}(\beta a_n)^5 - \cdots \right] . \tag{2.9}$$

The mutual eddy loss resistance of each circular conductor with any other circular conductor in the coil is obtained by modifying the resistance integral presented in [75] for a pair of coils. Considering filament type conductors with thin insulation layers, the wire radius can be neglected. The resulting situation is a special scenario of the mutual impedance integral presented in [31], where the integrals are to be evaluated for each pair of concentric circular conductors as shown in Fig. 2.3. Then for the first two turns the mutual resistance integral can be written as

$$R_{eddy,mut,12} = \frac{\omega_s \mu_0}{4\pi} \int \int \frac{\sin(\beta r_{12})}{r_{12}} \cos(\psi) ds_1 ds_2 , \tag{2.10}$$

where

$$r_{12} = \sqrt{{a_1}^2 + {a_2}^2 - 2a_1 a_2 \cos(\psi)} . \tag{2.11}$$

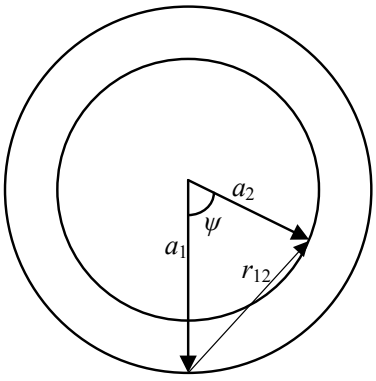

Fig. 2.3: Filamentary conductor model of turns 1 and 2 demonstrating the application of the integral in [31] for the circular coil.

The simplification of the integral in (2.10) and generalization for each pair of circular conductors in the coil lead to the complete mutual eddy loss resistance of the coil. The expression of r_{12} in (2.11) suggests that the integral in (2.10) involves elliptical integrals. These are simplified using the standard approximate forms for the complete elliptical integrals of the first kind ($K(\cdot)$) and second kind ($E(\cdot)$). The simplified relations are obtained as

$$R_{eddy,mut,12} = \frac{\omega_s \mu_0 \beta^2 a_1 a_2}{2\pi} \left[I_{1,12} - \frac{2\beta}{3}\pi^2 a_1 a_2 + \frac{2\beta^3}{15}\pi^2 a_1 a_2 (a_1 + a_2)^2 ({\kappa_{12}}^2 - 2) \right] , \quad (2.12)$$

with

$$I_{1,12} = 4\pi(a_1 + a_2) \left[E(\kappa_{12}) - \frac{2\sqrt{1 - {\kappa_{12}}^2}}{3{\kappa_{12}}^2} \left[K\left(\frac{{\kappa_{12}}^2}{{\kappa_{12}}^2 - 1} \right) - (2{\kappa_{12}}^2 - 1) E\left(\frac{{\kappa_{12}}^2}{{\kappa_{12}}^2 - 1} \right) \right] \right] , \quad (2.13)$$

where κ_{12} is the κ factor for circular conductors 1 and 2, given by $2\sqrt{a_1 a_2}/(a_1 + a_2)$. Using this method, the mutual eddy loss resistance between each pair of circular conductor is calculated and their sum gives the total mutual eddy loss resistance of the coil, which can be written in generalized terms as

$$R_{eddy,mutual} = \sum_{i=1}^{N} \sum_{j=1}^{N} \frac{\omega_s \mu_0 \beta^2 a_i a_j}{2\pi} \left[I_1 - \frac{2\beta}{3}\pi^2 a_i a_j + \frac{2\beta^3}{15}\pi^2 a_i a_j (a_i + a_j)^2 ({\kappa_{i,j}}^2 - 2) \right] (1 - \delta_{i,j}) , \quad (2.14)$$

with

$$I_1 = 4\pi(a_i + a_j)\left[E(\kappa_{i,j}) - \frac{2\sqrt{1-{\kappa_{i,j}}^2}}{3{\kappa_{i,j}}^2}\left[K\left(\frac{{\kappa_{i,j}}^2}{{\kappa_{i,j}}^2-1}\right) - (2{\kappa_{i,j}}^2-1)E\left(\frac{{\kappa_{i,j}}^2}{{\kappa_{i,j}}^2-1}\right)\right]\right] , \tag{2.15}$$

where $\delta_{i,j} = 1$ for $i = j$ & $\delta_{i,j} = 0$ for $i \neq j$, $\kappa_{i,j}$ is the κ factor for circular conductors i and j, given by $2\sqrt{a_i a_j}/(a_i + a_j)$. The $\delta_{i,j}$ factor makes sure that the mutual eddy loss resistance is not calculated for $i = j$, in which case the eddy loss resistance is calculated by the self eddy loss resistance formula in (2.9).

The sum of the total self and mutual eddy loss resistances of all the turns in the coil gives the total eddy loss resistance of the spiral coil as

$$R_{eddy} = R_{eddy,self} + R_{eddy,mutual} \ . \tag{2.16}$$

From the configuration in Fig. 2.2, the total ac resistance for each coil in seawater is obtained by

$$R_{ac,sea} = R_{pro} + R_{eddy} \ . \tag{2.17}$$

2.1.3 Self and Mutual Inductance Expressions

Self-inductance and mutual inductance of spiral coils for IPT are the basic properties, and they are available in approximate elliptic integral form in [118] for a concentric-circle model. Hence these can be directly used in the optimization for the model in Fig. 2.1(c). Equations (2.18) and (2.19) show the corresponding expressions, considering no misalignment between the coils and the gap between the coils denoted by g (in m). Subscripts "p" and "s" are used for primary and secondary coils respectively for the mutual inductance expression.

$$L = \sum_{i=1}^{N} \mu_0 a_i \left[\ln\left(\frac{8a_i}{r_w}\right) - 2 \right] + \sum_{i=1}^{N}\sum_{j=1}^{N} \mu_0 \sqrt{a_i a_j} \left[\left(\frac{2}{\kappa_0} - \kappa_0\right) K(\kappa_0) - \frac{2}{\kappa_0} E(\kappa_0) \right] (1 - \delta_{i,j}) \ , \tag{2.18}$$

$$M = \sum_{ip=1}^{N_p} \sum_{js=1}^{N_s} \mu_0 \sqrt{a_{ip} a_{js}} \left[\left(\frac{2}{\kappa_g} - \kappa_g\right) K(\kappa_g) - \frac{2}{\kappa_g} E(\kappa_g) \right] \ , \tag{2.19}$$

where κ_g is the κ factor for windings lying in planes separated by distance g, given by $2\sqrt{a_{ip}a_{js}}/((a_{ip} + a_{js})^2 + g^2)$. For misaligned coils, the Bessel function expressions can be utilized for mutual inductance calculation [118].

The expressions (2.6)-(2.7), (2.9) and (2.14)-(2.19) provide the complete analytical model for the coupled coils of an underwater IPT system. The resistance and self-inductance expressions are to be evaluated for each coil in the setup, whereas the mutual inductance is to be calculated for each pair of coils in the setup.

2.2 Analytical Optimization Method

2.2.1 Optimization constraints and algorithm

The main constraint of an underwater IPT system for small AUV application is the secondary coil size, since it is mounted on the AUV. Hence it is required to optimize the IPT interface for coil size, power transfer distance or seawater gap and operating frequency, with due considerations for the seawater losses modeled as in Section 2.1. Using this model, the analytical optimization is performed by sweeping operating frequencies and coil dimensions.

Commonly IPT systems are optimized according to the maximum achievable efficiency and power transfer capability [121]. However, this may not be achievable under most operation constraints. Hence in this work, the magnetic coupling efficiency (η_{mag}) is used as the optimization variable. Using the equivalent circuit model of an undersea submerged

coil in Fig. 2.2, the equivalent circuit of the underwater IPT coils is obtained as shown in Fig. 2.4. The magnetic coupling efficiency is defined as

$$\begin{aligned}\eta_{mag} &= \frac{P_{out,sec}}{P_{in,pri}} \\ &= \frac{P_{out,sec}}{P_{out,sec} + P_{loss,pri} + P_{loss,sec}} \\ &= \frac{P_{in,pri} - P_{loss,pri} - P_{loss,sec}}{P_{in,pri}} ,\end{aligned} \tag{2.20}$$

where $P_{out,sec}$ is the power output of the secondary coil, $P_{in,pri}$ is the power input to the primary coil, $P_{loss,pri}$ is the losses in primary coil, given by ${I_p}^2 R_{pri,uw}$, $P_{loss,sec}$ is the losses in secondary coil, given by ${I_s}^2 R_{sec,uw}$, I_p is the rms value of primary coil current (i_p), I_s is the rms value of secondary coil current (i_s), $R_{pri,uw}$ is the primary coil ac resistance underwater and $R_{sec,uw}$ is the secondary coil ac resistance underwater, both including their eddy loss resistances.

Using η_{mag} from (2.20) as the optimization variable not only gives more insight into the performance of the magnetics but also brings in the electrical specifications as constraints for optimization. The optimization procedure is shown in the flow-chart in Fig. 2.5, whose steps are performed as

A. At first, the secondary coil outside radius ($r_{out,s}$) is set to fit within the AUV dimensions, with sufficient room for increasing this dimension if required. Choose also a desired seawater gap (g), a target magnetic coupling efficiency (η_{des}) and a target range of frequencies for optimizations.

B. From electrical specifications of the system, range of litz wire dimensions for the primary and secondary coils are chosen. Care is taken to choose the proper strand size for the range of frequencies considered, such that skin effects can be neglected [116], and proper equivalent AWG wires are chosen as per the allowable current densities.

C. Choose range of turns for primary and secondary coils (N_p and N_s) and range of outside radii of primary coil ($r_{out,p}$) for running optimization analysis.

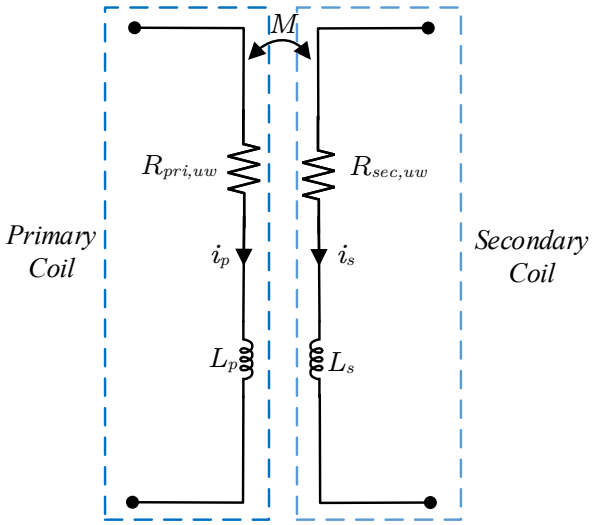

Fig. 2.4: Equivalent circuit representation of the coils in an underwater IPT system.

D. Run analytical optimization by sweeping through the operating frequencies and coil sizes chosen in the earlier steps, using the loss models developed in Section 2.1. Monitor η_{mag} at each step. Also monitor the frequency where the η_{mag} numbers are obtained without violating the current capacity of litz wires.

E. Accept the solution which achieves η_{mag} greater than the preset η_{des} in an acceptable frequency range, while minimizing copper volume.

F. If solution is not found, modify range of primary coil dimensions and re-run the algorithm until the selection criteria of the previous step are met. If they are still not met even with much larger primary than the secondary, then carefully try with larger secondary pads making sure they can be fitted within the AUV dimensions.

2.2.2 Credibility of the Analytical Optimization Method

The analytical optimizations are performed in this work to demonstrate how different dimensions of a spiral coil affect the performances in an underwater IPT. Moreover, this procedure is faster compared to the typically used FEM simulation based methods, while also utilizing less computation resources. However, the analysis is based on an infinite

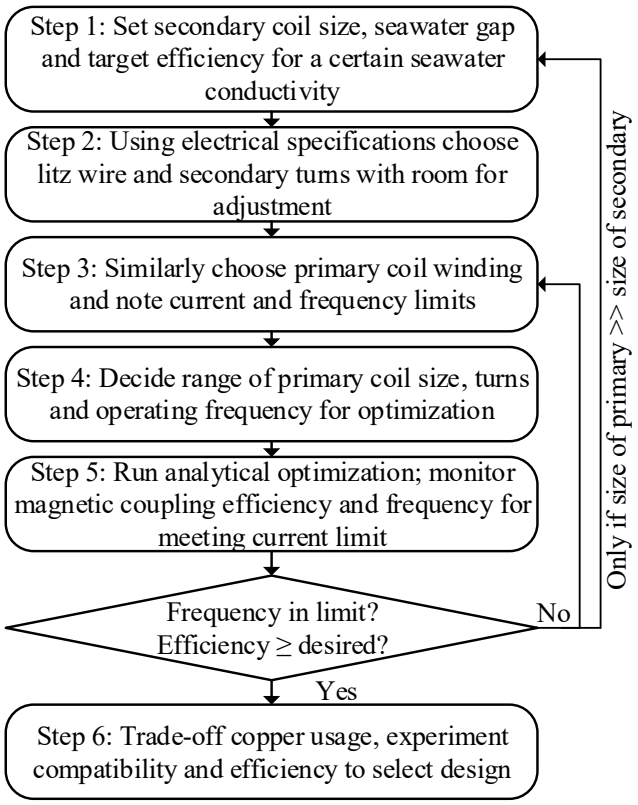

Fig. 2.5: Flow-chart for optimization of small spiral litz coil based for underwater IPT systems.

conducting medium around the coils, which assumes a uniform magnetic field through seawater. This is not the case when ferrite pads are employed to increase power capability and shields are used to limit leakage flux. But the method presented here is still useful in getting a ball-park range of coil dimensions and frequencies, before moving on to FEM simulations with smaller set of parameters to optimize.

The optimization algorithm is used to design coils for a constant voltage input underwater IPT topology, which is used to validate these analysis through experiments. The design of the coils using these optimization steps are demonstrated in Chapter 4, while the effectiveness of the loss model and validations of the optimizations through FEM simulations and experimental results are presented in Chapter 6.

CHAPTER 3

Description and Steady-state Analysis of Underwater IPT Topologies: Development of Constant Current Input Topology

Choice of topologies are important in the design of IPT systems for getting the desired output characteristics. It was shown in Chapter 1 that typical underwater IPT systems use a constant dc voltage input inverter configuration, LC type compensation networks and full-bridge rectifiers on the secondary side. In this dissertation work, at first a typical voltage input underwater IPT system is designed as a proof of concept system, which is also used as the experimental platform to validate the eddy current loss models and optimizations presented in Chapter 2. Afterwards, two versions of a constant dc current input IPT system are developed, to take power output from a constant dc current distribution system and generate a constant voltage output power supply for the AUV. This chapter describes the steady-state analysis of these topologies, which the rest of the works in the dissertation are based on.

3.1 Description of Underwater IPT Topologies Used in This Work

3.1.1 Typical Constant DC Voltage Input Topology With Series-Series (SS) Compensation

The circuit diagram of a typical constant dc voltage input underwater IPT system with series-series (SS) compensation is shown in Fig. 3.1, with its important quantities marked. The MOSFETs Q_1 through Q_4 form the full-bridge inverter (legs A and B), and the power diodes D_1 through D_4 constitute of the full-bridge diode rectifier. The inductances L_p and L_s pertain to the primary and secondary coils, whereas C_p and C_s represent the series compensation capacitors.

The inverter is operated with symmetrical, 50 % duty ratio pulses with a phase shift

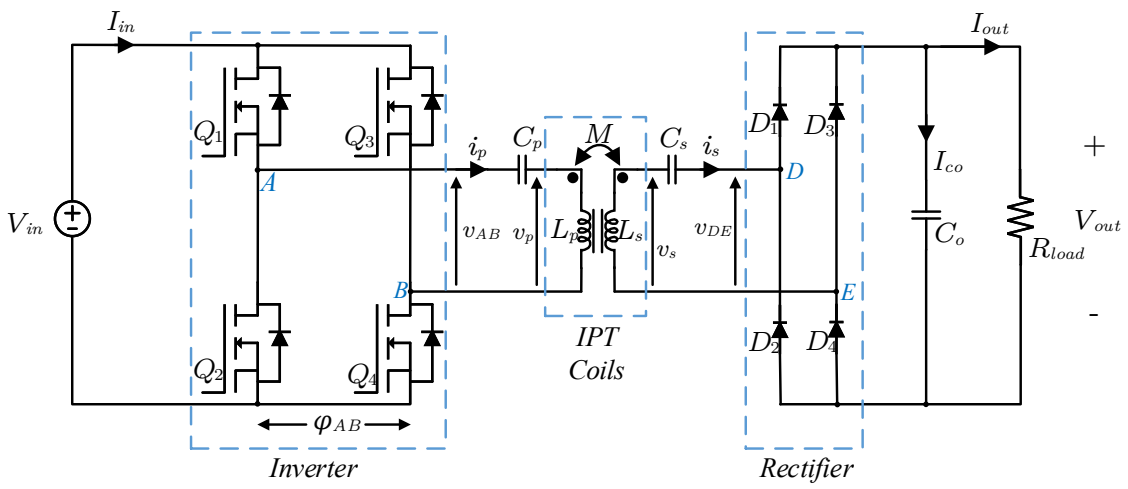

Fig. 3.1: Constant voltage input series-series underwater IPT system circuit diagram.

(φ_{AB}) among them. Both the duty ratio of the switches or the inverter phase shift φ_{AB} are common quantities of controlling the power flow through the IPT system, but the latter results in lower harmonics generated due to to the symmetrical ac waveforms obtained. Hence this dissertation has focused on using φ_{AB} as the control variable. The waveforms of the inverter leg switch nodes and the inverter output voltage v_{AB} (also the IPT network input voltage) are shown in Fig. 3.2. The quantity φ_{AB} is also indicated here which shows the power transfer interval of the inverter. The switches Q_1 and Q_4 conduct during the positive portion of v_{AB}, whereas the switches Q_2 and Q_3 conduct during the negative portion of v_{AB}. The diodes D_1 and D_4 conduct when the secondary current is positive, and the other pair of diodes D_2 and D_3 conduct when the secondary current is negative.

The constant voltage input SS generates a constant current output characteristics [107, 108], details of which are shown later in the chapter. This is not suitable for a constant voltage output application. Moreover it is not able to directly interface with a constant dc current distribution at the input side. Hence the IPT compensation networks were researched to develop two versions of constant dc current input topologies, which can achieve both the above-mentioned targets.

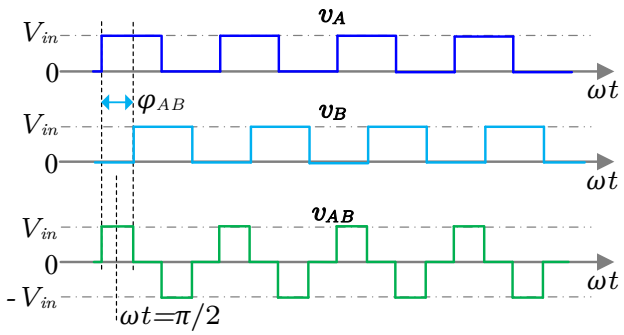

Fig. 3.2: Inverter waveforms pertaining to the constant voltage input underwater IPT topology and transformer-based constant current input underwater IPT topology, both of which use diode rectifier.

3.1.2 Proposed Constant DC Current Input Topology with SS Compensation, Current Boost Transformer and Diode Rectifier

As it was mentioned in Chapter 1, the underwater IPT systems developed in this dissertation are meant for interfacing with a constant dc low-current distribution link, useful in sea-bed installed applications. Typically, identical coils are used in IPT systems to allow best match between the primary and secondary sides. However this is not possible with the underwater IPT system under consideration, owing to the low input current and highly variable input voltages expected. As a first case solution to this, a transformer-based topology is used to boost the primary coil current and reduce the coil voltages, such that almost identical coils can be used in the IPT system.

The transformer-based constant dc current input underwater IPT topology is shown in Fig. 3.3, with its important components marked. The component descriptions are similar to the one presented for the voltage source IPT in the previous section, with the exceptions that a constant input current I_{in} is used at the input, a capacitor C_{in} is used to provide the ripple current to the inverter and a current boost transformer with transformation ratio of m:1 placed between the inverter and the primary resonant network.

Since the voltage-fed inverter structure is used along with the constant current input [62,65], the inverter waveforms shown in Fig. 3.2 are applicable for this topology. This gives simple control of the inverter output current i_{AB} amplitude through the phase shift angle

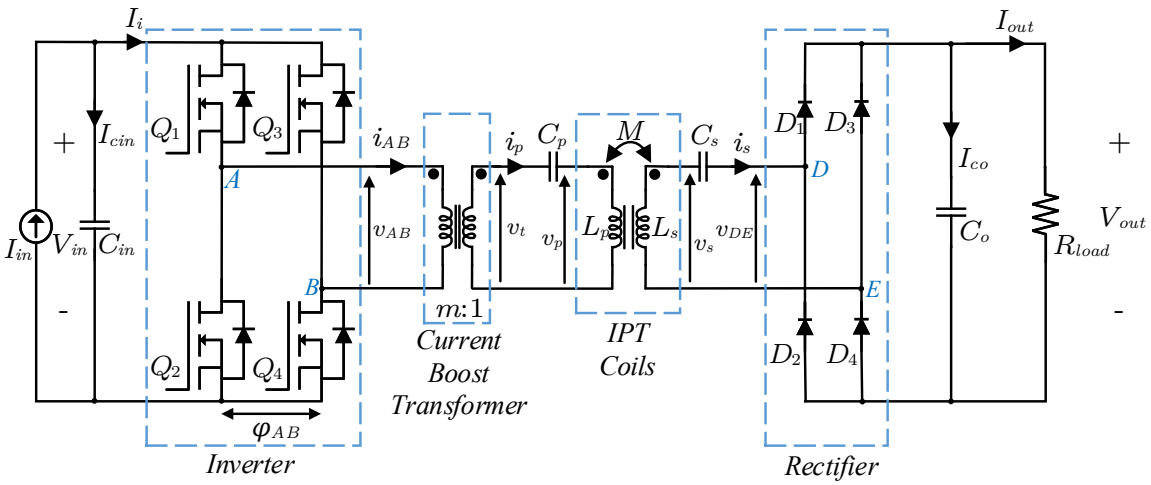

Fig. 3.3: Constant current input series-series underwater IPT system circuit diagram with current boost transformer and diode rectifier.

φ_{AB}. This configuration helps in achieving zero voltage switching (ZVS) in the primary side devices, which is crucial for high voltage operations to maintain low electromagnetic interference (EMI) and boost efficiency [104]. The input capacitor is designed to ensure sufficient ripple current capability.

Now, if the inverter output current or its boosted version is driven through the primary coil, a constant voltage output can be obtained with a series-series compensation [107,108], whose details are shown later in the analysis section of this chapter. This helps is getting the desired constant dc current input to constant dc voltage output conversion through the underwater IPT coils with the minimum volume of resonant network and gives the freedom of using identical IPT coils with the required voltage conversion taken care in the transformer.

In addition to above, this topology has the advantage of scaling down the voltage from the inverter output to the primary coils. This reduces the switching dv/dt across the primary coil. However, the high square wave voltage applied across the current boost transformer leads to higher core volumes and losses. Hence the topology has the tendency of achieve lower efficiency and lower power density. Also, the diodes used on the rectifier produce higher losses as the output current goes higher. This not only causes additional

losses in the system, but also leads to higher droop in output voltage with load. Hence another version of the topology is proposed to improve on these drawbacks.

3.1.3 Proposed Constant DC Current Input Topology with SS Compensation, Synchronous Rectifier and No Transformer

An improved version of the topology is also developed in this dissertation, as shown in Fig. 3.4, where the current-boost transformer is removed and the diode rectifier is replaced by a synchronous rectifier. While the inverter configuration and the IPT networks resemble the other two topologies described earlier, the rectifier consists of the MOSFETs Q_5 through Q_8 (legs D and E). The effect of the current boost transformer is absorbed in the IPT coupler design, such that desired current to voltage conversion is obtained. The synchronous rectification helps in improving the efficiency, reducing the voltage droop and driving the MOSFETs from the secondary side without any communication with the primary side.

The voltage and current waveforms for the transformer-less and synchronous rectification based constant current input underwater IPT topology are shown in Fig. 3.5, which shows the inverter phase angle φ_{AB} and the 180° conduction modes of rectifier. When the secondary current i_s goes positive, the switches Q_5 and Q_8 are turned on. When the current goes negative, the opposite pair, Q_6 and Q_7 are turned on. This helps emulate a full-bridge diode rectifier behavior. Hence for analysis the synchronous rectifier can be considered to work as a diode rectifier without loss of accuracy. A current transformer along with a hysteresis comparator is used for this purpose, details of which are shown in Appendix A.

The next sections present the steady-state analysis of the above topologies. At first the equivalent circuits are analyzed to get general impedance relations. Then the dc voltage and current expressions are derived by neglecting non-idealities, to demonstrate the output characteristics. Further, the effects of the non-idealities are analyzed for the constant dc current input transformer-less topology, for usage in design considerations later in the dissertation.

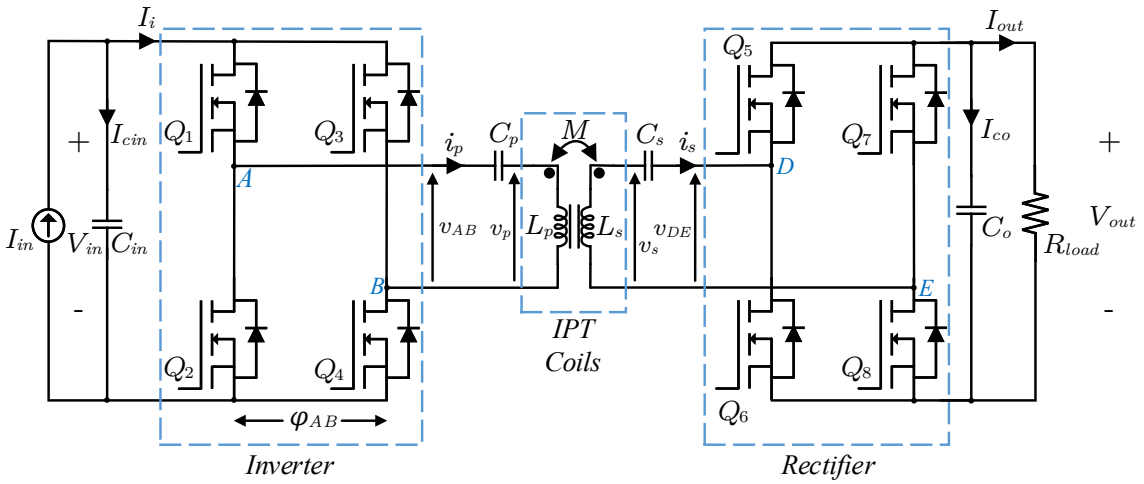

Fig. 3.4: Constant current input series-series underwater IPT system circuit diagram without current boost transformer and with synchronous rectifier.

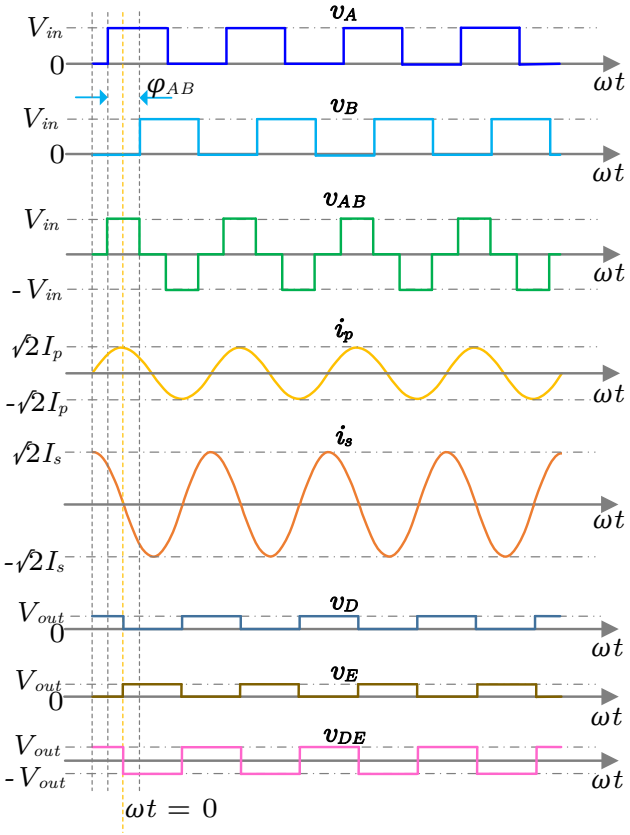

Fig. 3.5: Inverter and active rectifier waveforms pertaining to the transformer-less constant current input underwater IPT topology using synchronous rectification.

3.2 Circuit Analysis

3.2.1 Analysis of the IPT Network Equivalent Circuit

From Fig. 3.1, Fig. 3.3 and Fig. 3.4, it can be identified that the IPT network looks identical for all the above topologies. Also, the rectifiers in all the above topologies can be analyzed as diode rectifiers as explained above. Hence a common equivalent circuit of the SS compensated underwater IPT system is used for the analysis here, which is shown in Fig. 3.6(a). The tank input voltage is the inverter output voltage v_{AB} for the topologies in Fig. 3.1 and Fig. 3.4, which do not have any transformers. For the transformer-based constant current input topology in Fig. 3.3, the tank input voltage is the transformer secondary voltage v_t. The mutual inductance model of IPT network is used in Fig. 3.6(a), as this helps in analyzing the system as two coupled series resonant networks [122]. Fundamental harmonic approximation (FHA) [123] is applied to the analysis, as the bulk power is transmitted through the fundamental harmonic under most loading conditions. Also, X_y is used to denote the rms value of the corresponding ac quantity x_y.

In Fig. 3.6(a), v_r and v_{oc} represent the mutual coupling induced voltages in the primary and secondary coils. Using the mutual inductance principle, the relations between primary coil rms current (I_p), the secondary coil rms current (I_s) and rms values of v_r and v_{oc} (V_r and V_{oc} respectively) are obtained as

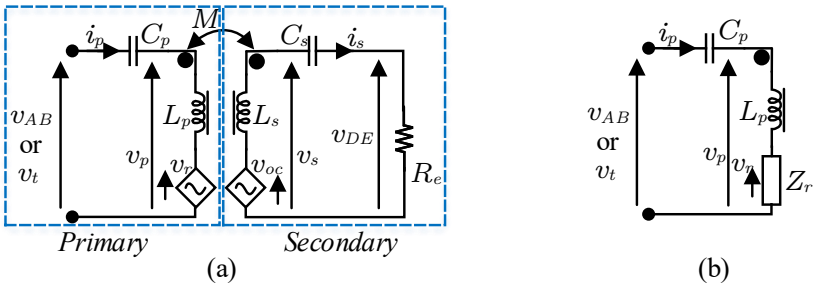

Fig. 3.6: Equivalent circuit model of series-series compensation based underwater IPT topologies (a) Mutual inductance model of the IPT interface showing the two series resonant tanks, (b) Model of the primary resonant tank showing the reflected impedance Z_r.

$$V_r = \omega_s M I_s \ , \tag{3.1}$$

$$V_{oc} = \omega_s M I_p \ , \tag{3.2}$$

where $\omega_s = 2\pi f_s$ is the angular frequency of the primary coil current (i_p) and the secondary coil current (i_s), with f_s representing the frequency of the currents. Using the above expressions, the primary coil induced voltage V_r can be written in terms of I_p and the reflected impedance Z_r. This leads to the primary tank equivalent circuit shown in Fig. 3.6(b), where V_r is the voltage across Z_r.

To get the expressions, at first the equivalent circuit of the full-bridge rectifier with capacitive dc side filter is considered from Fig. 3.6(a). For the resistive loads shown in Fig. 3.1, Fig. 3.3 and Fig. 3.4, the equivalent resistance seen by the secondary tank in the equivalent circuit can be expressed as

$$R_e = \frac{8}{\pi^2} R_{load} \ , \tag{3.3}$$

where R_{load} is the load resistance. Defining the primary and secondary tank resonant frequencies (ω_{op} and ω_{os}), normalized switching frequencies (F_p and F_s), characteristic impedances (Z_{op} and Z_{os}) and the secondary tank loaded quality factor (Q_{sl}) as

$$\omega_{op} = 2\pi f_{op} = \frac{1}{\sqrt{L_p C_p}} \ , \tag{3.4}$$

$$\omega_{os} = 2\pi f_{os} = \frac{1}{\sqrt{L_s C_s}} \ , \tag{3.5}$$

$$F_p = \frac{\omega_s}{\omega_{op}} = \frac{f_s}{f_{op}} \ , \tag{3.6}$$

$$F_s = \frac{\omega_s}{\omega_{os}} = \frac{f_s}{f_{os}} \ , \tag{3.7}$$

$$Z_{op} = \omega_{op} L_p = \frac{1}{\omega_{op} C_p} \ , \tag{3.8}$$

$$Z_{os} = \omega_{os} L_s = \frac{1}{\omega_{os} C_s} \ , \tag{3.9}$$

$$Q_{sl} = \frac{Z_{os}}{R_e} \ . \tag{3.10}$$

The secondary tank impedance (Z_s), reflected impedance (Z_r) and primary tank impedance (Z_p) can be obtained as

$$Z_s = R_e + j\left(\omega_s L_s - \frac{1}{\omega_s C_s}\right) = |Z_s| \angle \varphi_s \ , \tag{3.11}$$

$$Z_r = \frac{{\omega_s}^2 M^2}{Z_s} = |Z_r| \angle \varphi_r \ , \tag{3.12}$$

$$Z_p = j\left(\omega_s L_s - \frac{1}{\omega_s C_s}\right) + Z_r = |Z_p| \angle \varphi_p \ , \tag{3.13}$$

where, the impedance magnitude and phase expressions are

$$|Z_s| = R_e\sqrt{1 + {Q_{sl}}^2\left(F_s - \frac{1}{F_s}\right)^2}\ , \tag{3.14}$$

$$\varphi_s = \tan^{-1}\left[Q_{sl}\left(F_s - \frac{1}{F_s}\right)\right]\ , \tag{3.15}$$

$$|Z_r| = \frac{{\omega_s}^2 M^2}{|Z_s|}\ , \tag{3.16}$$

$$\varphi_r = -\varphi_s\ , \tag{3.17}$$

$$|Z_p| = \frac{{\omega_s}^2 M^2\sqrt{1+G^2}}{R_e\left[1 + {Q_{sl}}^2\left(F_s - \frac{1}{F_s}\right)^2\right]}\ , \tag{3.18}$$

$$\varphi_p = \tan^{-1}(G)\ , \tag{3.19}$$

where the expression of the polynomial G is

$$G = \frac{Z_{op}\left(F_p - \frac{1}{F_p}\right)R_e\left[1 + {Q_{sl}}^2\left(F_s - \frac{1}{F_s}\right)^2\right]}{{\omega_s}^2 M^2} - Q_{sl}\left(F_s - \frac{1}{F_s}\right)\ . \tag{3.20}$$

3.2.2 Analysis of The Inverter and Rectifier

The inverter and rectifier configurations of all the topologies considered follow the full-bridge inverter and rectifier configurations [62,68]. Corresponding to that, the inverter and rectifier relations using the rms magnitudes can be written as

$$V_{AB} = \frac{2\sqrt{2}}{\pi}V_{in}\sin\left(\frac{\varphi_{AB}}{2}\right)\ , \tag{3.21}$$

$$I_{AB} = \frac{\pi I_{in}}{2\sqrt{2}\sin\left(\frac{\varphi_{AB}}{2}\right)\cos(\varphi_p)}\ , \tag{3.22}$$

$$V_{out} = \frac{\pi}{2\sqrt{2}}V_{DE}\ , \tag{3.23}$$

$$I_{out} = \frac{2\sqrt{2}I_s}{\pi}\ . \tag{3.24}$$

Now, these general expressions are utilized to derive the ideal characteristics of these topologies in steady-state.

3.3 Ideal Characteristics Analysis of the Considered Topologies

Under ideal conditions, operation of both resonant tanks are considered at resonance and at unity power factor, expressed as

$$F_p \approx F_s \approx 1 \ , \tag{3.25}$$

$$\cos(\varphi_p) \approx \cos(\varphi_s) \approx 1 \ , \tag{3.26}$$

Hence at ideal conditions the tank impedance relations modify to

$$Z_s = R_e \ , \tag{3.27}$$

$$Z_r = \frac{{\omega_s}^2 M^2}{R_e} = R_r \ , \tag{3.28}$$

$$Z_p = R_r \ , \tag{3.29}$$

Using the above, the steady-state voltage and current relations and characteristics of the different topologies in consideration are found, as shown in the following sections.

3.3.1 Expressions and Characteristics for the Constant DC Voltage Input Underwater IPT Topology

For the constant dc voltage input underwater IPT topology in Fig. 3.1, the input to the system is a constant dc voltage V_{in}. Also, from the equivalent circuits in Fig. 3.6, the following relations are obtained for this topology:

$$V_{AB} = V_r \ , \tag{3.30}$$

$$V_{oc} = V_{DE} \ . \tag{3.31}$$

Then, using (3.1), (3.2), (3.21) and (3.23), I_p and I_s can be expressed as

$$I_p = \frac{V_{DE}}{\omega_s M} = \frac{2\sqrt{2}}{\pi}\frac{V_{out}}{\omega_s M} \ , \tag{3.32}$$

$$I_s = \frac{V_{AB}}{\omega_s M} = \frac{2\sqrt{2}}{\pi}\frac{V_{in}}{\omega_s M}\sin\left(\frac{\varphi_{AB}}{2}\right) \ . \tag{3.33}$$

Then, using the above expression of I_s in (3.24), the output current is obtained as

$$I_{out} = \frac{8}{\pi^2}\frac{V_{in}}{\omega_s M}\sin\left(\frac{\varphi_{AB}}{2}\right) \ . \tag{3.34}$$

The expressions (3.33) and (3.34) demonstrate that the secondary tank current and load current in the constant dc voltage input IPT topology are load-independent. Hence, the output voltage from this topology is load-dependent, obtained as

$$V_{out} = I_{out}R_{load} = \frac{8}{\pi^2}\frac{V_{in}R_{load}}{\omega_s M}\sin\left(\frac{\varphi_{AB}}{2}\right) \ . \tag{3.35}$$

This is why the constant dc voltage output topologies fed from constant dc current source are proposed in this dissertation.

3.3.2 Expressions and Characteristics for Transformer-based Constant DC Current Input Underwater IPT Topology

For the transformer-based constant current input underwater IPT topology, a transformer of voltage ration m:1 is put between the inverter and IPT coils. The design is made

in such a way that even operating with square wave voltage, the effective transformation ratio is achieved at the fundamental harmonic. Then using the transformer relation, the expression (3.30) transforms to

$$V_t = \frac{V_{AB}}{m} = V_r \ . \tag{3.36}$$

On the other hand, (3.31) is applicable without modification. However, both these topologies use a constant current I_{in} at the input.

Then, using (3.1), (3.2), (3.22) and (3.23), I_{AB}, I_p and V_{DE} can be expressed as

$$I_{AB} = \frac{\pi}{2\sqrt{2}\sin\left(\frac{\varphi_{AB}}{2}\right)} I_{in} \ , \tag{3.37}$$

$$I_p = mI_{AB} = \frac{m\pi}{2\sqrt{2}\sin\left(\frac{\varphi_{AB}}{2}\right)} I_{in} \ , \tag{3.38}$$

$$V_{DE} = V_{oc} = \frac{m\pi\omega_s M}{2\sqrt{2}\sin\left(\frac{\varphi_{AB}}{2}\right)} I_{in} \ . \tag{3.39}$$

Then, using the above expression of V_{DE} in (3.39) , the output current is obtained as

$$V_{out} = \frac{\pi^2}{8} \frac{m\omega_s M I_{in}}{\sin\left(\frac{\varphi_{AB}}{2}\right)} \ . \tag{3.40}$$

Further, using the above, expressions of I_{out} and V_{in} can be found as

$$I_{out} = \frac{V_{out}}{R_{load}} = \frac{\pi^2 m\omega_s M I_{in}}{8R_{load}\sin\left(\frac{\varphi_{AB}}{2}\right)} \ , \tag{3.41}$$

$$V_{in} = \frac{P_{out}}{I_{in}} = \frac{m^2\pi^4{\omega_s}^2 M^2 I_{in}}{64R_{load}\sin^2\left(\frac{\varphi_{AB}}{2}\right)} \ . \tag{3.42}$$

The expression (3.40) demonstrates the constant voltage output characteristics of the topology, which indicates a load-independent V_{out} with a fixed I_{in} and φ_{AB}. The expression

of I_p in (3.38) also shows load and coupling independent characteristics of the primary coil current. On the other hand, the input voltage is found to be load-dependent as shown in (3.42). As output power increases, the input voltage also increases.

In this topology, With a proper choice of transformer ratio m, identical values of the coils can be utilized to get the desired output voltage. As per the structure of the topology, the primary compensation capacitor can be kept on either the transformer input side or the transformer output side. The second one is typically a better choice as lower voltage ratings will be required and the total effect of the transformer leakage inductance can be compensated. As a result, this topology is suitable for very low currents on the input, such that the transformer can be used to match the coil currents, while at the cost of introducing a potentially high-volume transformer in the circuit.

3.3.3 Expressions and Characteristics for the Transformer-less Constant DC Current Input Underwater IPT Topology

Both (3.30) and (3.31) are applicable without modifications to the transformer-less constant dc current input underwater IPT topology. Moreover, the expressions for the transformer-less topology are obtained simply by omitting the transformer ratio m from the transformer-based topology. Hence the relevant expressions for this topology can be written as

$$I_p = I_{AB} = \frac{\pi}{2\sqrt{2}\sin\left(\frac{\varphi_{AB}}{2}\right)} I_{in} \ , \tag{3.43}$$

$$V_{oc} = \frac{\pi\omega_s M}{2\sqrt{2}\sin\left(\frac{\varphi_{AB}}{2}\right)} I_{in} \ , \tag{3.44}$$

$$V_{out} = \frac{\pi^2}{8}\frac{m\omega_s M I_{in}}{\sin\left(\frac{\varphi_{AB}}{2}\right)} \ , \tag{3.45}$$

$$I_{out} = \frac{V_{out}}{R_{load}} = \frac{\pi^2\omega_s M I_{in}}{8R_{load}\sin\left(\frac{\varphi_{AB}}{2}\right)} \ , \tag{3.46}$$

$$V_{in} = \frac{P_{out}}{I_{in}} = \frac{\pi^4{\omega_s}^2 M^2 I_{in}}{64R_{load}\sin^2\left(\frac{\varphi_{AB}}{2}\right)} \ . \tag{3.47}$$

Similar to the transformer-based topology, this topology too has the load-independent output voltage and primary current characteristics as per (3.45) and (3.43), while having load-dependent input voltage as shown in (3.47).

As the transformer current boost ratio of m is not available in this, the equivalent current to voltage conversion ratio is needed to be achieved through the mutual inductance, considering operating at the same I_{in} and φ_{AB} as compared to the transformer-based topology. As a result, comparatively larger coil inductances are required and matched coils cannot be used for high mismatches in input and output voltage levels. However careful consideration of the magnetics leads to achieve a similar performance to the transformer-based topology along with a higher power density, which is why this topology is designed for the full power operation in this dissertation.

3.4 Effects of Non-idealities

In real designs, there are mistuning due to component tolerances and misalignment between IPT coils, changes in coupling due to misalignment and parasitic ESRs associated with the coils, devices and capacitors, which make the output voltage deviate from its design point and typical characteristics. These are especially important with inevitable misalignment in the underwater environment and eddy current losses in seawater [5]. In this section, the effects of mistuning and ESRs are analyzed for the transformer-less constant dc current input underwater IPT topology, as this is the one later utilized for full power design considerations in Chapter 4 and also for its small-signal model development in Chapter 5. The effect of losses on the transformer-based topology is shown by suitable incorporation of the turns ratio m, which is also used in its small-signal modeling work in Chapter 5.

3.4.1 Effect of Mistuning

Under mistuned conditions, the ideal condition assumptions (3.25) and (3.26) do not apply. Hence, the expressions in (3.11)-(3.20) are to be considered exactly for the impedances. Correspondingly, the magnitude relations between V_{AB}, I_p, V_{oc} and V_{DE} modify to

$$V_{AB} = |Z_p| I_p \ , \tag{3.48}$$

$$V_{oc} = |Z_s| I_s = \frac{|Z_s|}{R_e} V_{DE} \ . \tag{3.49}$$

Using (3.19) in (3.22) the expression of I_p modifies to

$$I_p = \frac{\pi I_{in}}{2\sqrt{2}\sin\left(\frac{\varphi_{AB}}{2}\right)\frac{1}{\sqrt{1+G^2}}} = \frac{\pi\sqrt{1+G^2} I_{in}}{2\sqrt{2}\sin\left(\frac{\varphi_{AB}}{2}\right)} \ , \tag{3.50}$$

with G as expressed in (3.20). The induced voltage V_{oc} still follows the expression (3.44). Then, the expression of V_{DE} can be written from (3.14) and (3.49) as

$$\begin{aligned} V_{DE} &= \frac{R_e}{|Z_s|} \cdot \omega_s M I_p \\ &= \frac{\omega_s M}{\sqrt{1 + {Q_{sl}}^2 \left(F_s - \frac{1}{F_s}\right)^2}} \frac{\pi\sqrt{1+G^2} I_{in}}{2\sqrt{2}\sin\left(\frac{\varphi_{AB}}{2}\right)} \ . \end{aligned} \tag{3.51}$$

Using (3.23) into the above, the expression of V_{out} in terms of I_{in} is found as

$$V_{out} = \frac{\pi^2 \omega_s M \sqrt{1+G^2} I_{in}}{8\sqrt{1 + {Q_{sl}}^2 \left(F_s - \frac{1}{F_s}\right)^2}\sin\left(\frac{\varphi_{AB}}{2}\right)} \ . \tag{3.52}$$

Using in (3.18) and (3.21) into (3.48) the expression of V_{in} is obtained as

$$V_{in} = \frac{\pi^4 {\omega_s}^2 M^2 (1+G^2) I_{in}}{64\left[1 + {Q_{sl}}^2 \left(F_s - \frac{1}{F_s}\right)^2\right]\sin^2\left(\frac{\varphi_{AB}}{2}\right) R_{load}} \ . \tag{3.53}$$

The expressions (3.50) and (3.52) demonstrate that both I_p and V_{out} become load dependent, as the power factor becomes load dependent under mistuning.

3.4.2 Effect of Equivalent Series Resistances (ESR)

On the other hand, for finding the effect of ESR the assumptions in (3.25) and (3.26) are considered, but the equivalent circuit is modified to show the ESRs. The equivalent circuit of the IPT network with the ESRs included is shown in Fig. 3.7(a), whereas the primary side equivalent is shown in Fig. 3.7(b). The primary side equivalent ESR is represented as R_p which includes underwater equivalent ac resistance of the primary coil ($R_{pri,uw}$) as explained in Chapter 2, ESR of the compensation capacitors (R_{cp}) and the effect of the primary MOSFET on-state resistance ($R_{ds,on,p}$). Similarly, the secondary tank ESR is represented as R_s including underwater equivalent ac resistance of the secondary coil ($R_{sec,uw}$), ESR of the compensation capacitors (R_{cs}) and the effect of the secondary MOSFET on-state resistance ($R_{ds,on,s}$). Considering these the tank impedances can be written as

$$Z_{s,esr} = R_e + R_s \ , \tag{3.54}$$

$$Z_{r,esr} = \frac{{\omega_s}^2 M^2}{R_e + R_s} \ , \tag{3.55}$$

$$Z_{p,esr} = Z_{r,esr} + R_p \ . \tag{3.56}$$

As the tanks are considered at resonance, the power factors are at unity. So (3.44) is applicable for V_{oc}. Also, the relations between V_{AB} and I_p and V_{oc} and V_{DE} in this case

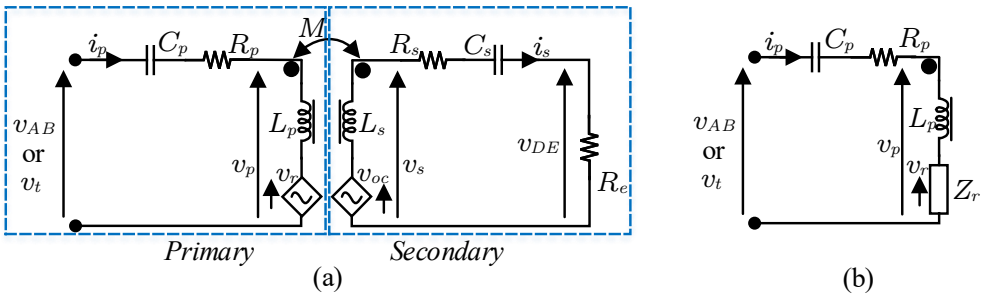

Fig. 3.7: Equivalent circuit model of series-series compensation based underwater IPT topologies including ESRs (a) Mutual inductance model of the IPT interface showing the two series resonant tanks, (b) Model of the primary resonant tank showing the reflected impedance Z_r.

can be written as

$$V_{AB} = Z_{p,esr} I_p \ , \tag{3.57}$$

$$V_{oc} = Z_{s,esr} I_s = \frac{Z_{s,esr}}{R_e} V_{DE} \ . \tag{3.58}$$

Using (3.23), (3.44) and (3.58), the expression of V_{out} is obtained as

$$V_{out} = \frac{\pi^2 \omega_s M I_{in}}{8\left(1 + \frac{R_s}{R_e}\right) \sin\left(\frac{\varphi_{AB}}{2}\right)} \ , \tag{3.59}$$

On the other hand, plugging in (3.21) and (3.56) in (3.57), the expression of V_{in} in presence of ESRs is obtained as

$$V_{in} = \frac{\pi^4 {\omega_s}^2 M^2 I_{in}}{64 \sin^2\left(\frac{\varphi_{AB}}{2}\right) R_{load}} \frac{1 + R_p \frac{R_s + R_e}{{\omega_s}^2 M^2}}{1 + \frac{R_s}{R_e}} \ . \tag{3.60}$$

The expression in (3.59) shows that the ESRs also make the output voltage load dependent, but only the secondary tank ESR causes the droop in output voltage. However, the effect of the primary tank ESRs are evident in the input voltage, as shown in (3.60), as more losses are occurred in the system. The primary tank current does not change with load, but to regulate a desired V_{out}, changing I_p is necessary with load.

3.5 Advantages and Drawbacks of the Proposed Constant Current Input SS IPT Topologies

In addition to providing the desired constant current to constant voltage conversions, the constant dc current input SS IPT topologies provide a few additional advantages, which inspired the selection of them for this work. First of all, these topologies are operable at no-load as well as under uncoupled conditions, transferring zero power in each case, as primary

coil current is load and coupling independent at resonant operation of both tanks. Also, the input voltage shows load-dependent behavior, reducing to zero as no-load or zero-coupling conditions are encountered. These demonstrate that these topologies avoid the principal drawback of a typical constant dc voltage input SS IPT system, which tends to draw large primary coil currents at no-load and also tends to transfer larger power with low efficiencies as the coupling goes down. The proposed topologies also avoids these situations without additional compensation tank elements such as in the $LCCL$ compensations [3].

Secondly, these topologies offer simple control of the output voltage through the inverter phase shift φ_{AB}, which helps in operating the switches with fixed frequency and duty ratio such that near resonant operation can be maintained without causing additional electromagnetic interference. Also the voltage-fed inverter topology helps in achieving zero voltage switching of the high-voltage MOSFETs, either through the tank current (if operating at lagging power factor) or through an additional active ZVS assistance leg [104]. Hence the system can operate with the least amount of EMI generation.

On the other hand, the main drawback of these topologies is that the non-idealities, especially the tank mistuning, lead to deviation from the above-mentioned characteristics. Optimized design of the secondary coil and selection of low-loss MOSFETs can lead to minimize the effect of ESR on the voltage droop, but careful design of the resonant networks are necessary to control the effects of mistuning. Another potential drawback is that, in SS IPT system the high dv/dt occurring due to the MOSFET switching appears across the coils. Hence the coil voltages have sufficient harmonics even though the power transfer happens mostly through the fundamental harmonic. These step changes in coil voltages drive high-frequency oscillations in the tank currents, by triggering resonance with the coils and their parasitic capacitances. In addition, in underwater IPT, the presence of saline water between the coils lead to increased common-mode coupling capacitance, which can lead to increased common-mode currents driven by the coil voltage dv/dt, a brief account of which is given in Appendix C.

The above drawbacks indicate that different design criteria are required to be carefully

considered so that the constant voltage characteristics can be maintained over a wide load range and with a high voltage in the input. The following chapter explains optimized coil designs for the constant dc voltage input underwater IPT topology applying the methods highlighted in Chapter 2 and the design considerations for the constant dc current input underwater SS IPT topologies, which are used to achieve the above-mentioned characteristics with real designs.

CHAPTER 4

Designs of the Constant DC Voltage Input and Proposed Constant DC Current Input Underwater IPT Topologies

The steady-state analysis of the state-of-the-art constant dc voltage input and proposed constant dc current input underwater IPT topologies presented in the previous chapter demonstrate their output characteristics, but to achieve them in real designs certain considerations are required. As in this dissertation the constant dc voltage input topology is only used to validate the seawater loss characterizations and coil optimizations, the design only shows how the expressions in Chapter 2 and Chapter 3 are used to build a proof-of-concept system with an input voltage of 48 V, for operation with air core coils up to 48 V, 1 kW output. Further, the proposed constant dc current input topology with current boost transformer is also designed as a proof-of-concept for a system with 1 A input, 16 V output, operable up to 330 W. Finally, the full design considerations of a constant dc current input underwater SS IPT topology to achieve constant output voltage in a wide load range with high efficiency and low system volume are presented, to the development of a 1 A input, 75 V output underwater IPT system for operation up to 1 kW under different alignment conditions.

4.1 Design of Constant Voltage Input SS IPT System

The constant dc voltage input underwater IPT system was designed for a target magnetic coupling efficiency (η_{mag}) of 96 %, such that a dc-dc efficiency of 90 % can be achieved, with considerations for the losses in the devices and compensation capacitors. In addition, the system was designed considering the diameter of the AUV to be around 120 mm, such that the secondary coil should be designed small enough to fit within it.

4.1.1 Choice of Coil Dimensions

To fit the above AUV dimensions with sufficient room for optimizations, initial value of the secondary coil outside radius $r_{out,s}$ was set to be 35 mm such that it can be fitted within the AUV along with other accessories. The nominal seawater conductivity of 5 S/m was considered [120]. For such small IPT systems, spiral coils with uniform pitch equal to the diameter of the winding and compact systems with small gap between the coils is preferable [70]. Hence spiral coils with uniform pitch were considered in this optimization with a nominal seawater gap g of 8 mm.

For the specifications mentioned above, neglecting the losses of the associated power electronics and capacitor ESRs, the currents of the two tanks were obtained as

$$I_p = \frac{\pi}{2\sqrt{2}} \frac{P_{out}}{V_{in}\eta_{mag}} = 24.1\,\text{A}\ , \tag{4.1}$$

$$I_s = \frac{\pi}{2\sqrt{2}} \frac{P_{out}}{V_{out}} = 23.14\,\text{A}\ . \tag{4.2}$$

Hence, wires for both coils were chosen considering a maximum rms current of 30 A, leading to the selection of equivalent AWG#10 litz wire with 2625 AWG#44 strands, having an winding area (A_w) of 6.77 mm^2 with optimum frequency range of operation of 100 kHz to 850 kHz [116].

With this choice of litz wire, the secondary coil number of turns N_s was set as 5, which keeps some space near the coil center for adjustments, if necessary. Now the system was analyzed for primary coil outside radius $r_{out,p}$ in the range 35 mm to 55 mm, primary coil number of turns N_p in the range 4 to 12 and f_s in the range 100 kHz to 500 kHz.

The inverter was operated with V_{in} of 48 V and 180° phase shift between the legs. Phase shift control was not incorporated in this design as the high-current inverter configuration requires larger ZVS assistance currents with phase shift control [104]. With this in consideration, the coil designs helping to achieve V_{in} of 48 V were considered for further analysis from the optimization plots. For the qualified designs, η_{mag} and the frequency where the

η_{mag} occurs (to be termed as optimal frequency $f_{s,opt}$) values were plotted against N_p for the considered range of $r_{out,p}$. The plots are shown in Fig. 4.1.

The marked points on the maroon plots show that the primary coil with $N_p = 7$, $r_{out,p} = 40\,\text{mm}$ at $f_{s,opt} = 325\,\text{kHz}$ would provide the best η_{mag} of 97.3 %. Hence this was the optimal design. However, due to the presence of prototype electronics optimized for operation around 250 kHz in the laboratory, the plots in Fig. 4.1 were re-examined for an operating point, meeting $\eta_{mag,des}$ of 96 %. From the marked points on the purple plots in Fig. 4.1, the design with $N_p = 8$, $r_{out,p} = 50\,\text{mm}$ at $f_{s,opt} = 252\,\text{kHz}$ was found to be meeting it closest to 250 kHz with minimum primary coil copper volume. Hence this design was selected for the experiments, with predicted magnetic coupling efficiency of 96.7 %. The parameters of the system are shown in Table 4.1.

4.1.2 Component Sizing

The system was designed to operate at resonance, such that the impedance of the tanks are minimized. So the compensation capacitor values are obtained as

$$C_p = \frac{1}{{\omega_s}^2 L_p}\ , C_s = \frac{1}{{\omega_s}^2 L_s}\ . \tag{4.3}$$

The capacitance parameters are listed in Table 4.1. Then, the capacitor voltage ratings are obtained as

Table 4.1: Design and setup parameters for proof-of-concept constant voltage input underwater IPT system.

Parameter	**Values**
L_p	4.98 µH
L_s	2.14 µH
C_p	75 nF
C_s	185 nF
Q_1-Q_4	IRFP4310ZPBF, 100 V, 120 A
D_1-D_4	APT30S20B(G), 200 V, 45 A

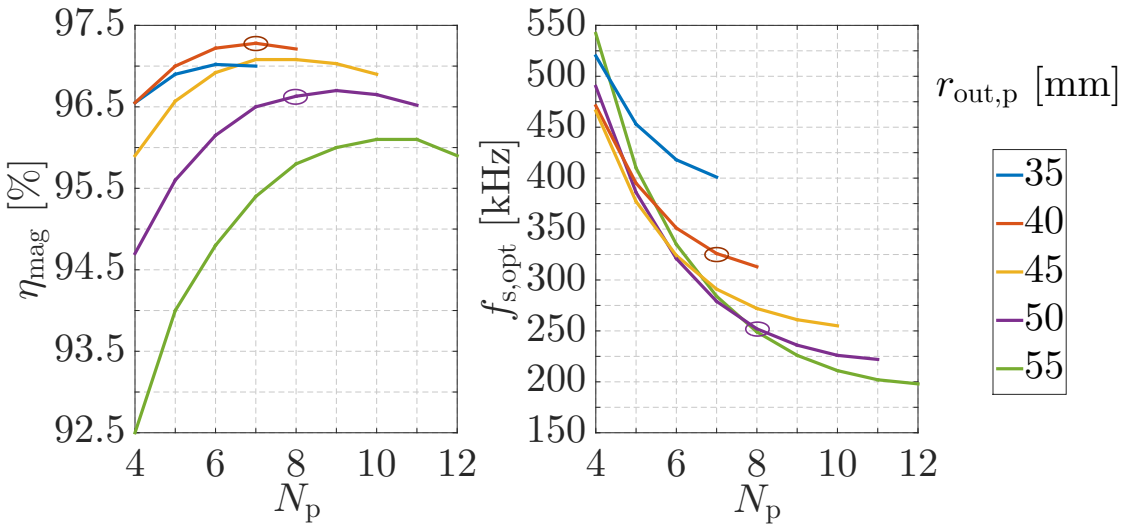

Fig. 4.1: Plots of magnetic efficiency (η_{mag}) and optimal frequency ($f_{s,opt}$) with respect to primary coil number of turns (N_p) for primary coil outside radius ($r_{out,p}$) in the range 35 mm to 55 mm and input voltage (V_{in}) = 48 V.

$$V_{cp,pk} = \frac{\sqrt{2}I_p}{\omega C_p} \, , V_{cs,pk} = \frac{\sqrt{2}I_s}{\omega C_s} \, . \tag{4.4}$$

Ceramic capacitors with sufficient ac voltage ratings at 250 kHz were chosen according to the above relations.

The primary bridge switches were driven at 50 % duty ratio. At full power the diode rectifier also operates at continuous conduction mode (CCM), which indicates operating with a duty ratio of 50 %. Then the device current ratings were found using the current expressions in (4.1)-(4.2) as

$$I_{qp,rat} = \frac{I_p}{\sqrt{2}} \, , I_{ds,rat} = \frac{I_s}{\sqrt{2}} \, . \tag{4.5}$$

The peak voltage across each primary switch was determined by the input voltage, while the peak voltage across each rectifier diode was the output voltage at peak load, both

of which were 48 V. According to the above rating requirements of the switches and diodes, the parts listed in Table 4.1 were selected for use.

4.2 Design of the Transformer-based Constant Current Input Underwater SS IPT System

The transformer-based constant dc current input underwater IPT topology was designed as a proof-of-concept for showing the constant current to constant voltage conversion through a wireless link. This design was made to operate with the same coils used in the voltage source IPT system, but with ferrite backplates to boost mutual inductance and use larger seawater gap. As a very low input current of 1 A was used for this work, the voltage expressions for this topology in Chapter 3 shows the importance of having a large mutual inductance. Along with them, this design uses the current-boost transformer to show how the transformer design helps in design of the topology with any set of coils. With the range of mutual inductance available from this setup with a seawater gap of 18 mm, the system was designed for 16 V output with up to 330 W output power.

4.2.1 Input Current to Output Voltage Gain Considerations

From the output voltage expression of the transformer-based topology in Chapter 3 the input current to output voltage gain ($Z_{t,tr}$) can be expressed as

$$Z_{t,tr} = \frac{m\pi^2\omega_s M}{8\sin\left(\frac{\varphi_{AB}}{2}\right)} \ , \tag{4.6}$$

From the above, the current boost transformer turns ratio is found as

$$m = \frac{8\sin\left(\frac{\varphi_{AB}}{2}\right) Z_{t,tr}}{\pi^2\omega_s M} \ , \tag{4.7}$$

The coil parameters obtained from the above-mentioned setup are shown in Table 4.2.

The system was designed for an ideal inverter phase shift angle (φ_{AB}) of around 120°, as this limits the third harmonic voltage injection into the IPT network from the voltage-fed inverter output [124]. Under these conditions, the transformer turns ratio of 5:1 was obtained to generate 16 V at the output operating at 250 kHz, which is mentioned in Table 4.2.

4.3 Design of the Transformer

The only item designed specifically for this topology was the current-boost transformer. The primary current rating of the transformer was obtained from the worst case φ_{AB} of 100° using the inverter output current expressions in Chapter 3. Accordingly, equivalent AWG#18 wires with AWG#42 strands were selected for operation at 250 kHz.

For operating up to 330 W from a constant 1 A input current, a minimum peak voltage of 330 V is expected at the input. Keeping sufficient safety margins, the isolation requirements between the transformer primary and secondary windings can be assumed to be around 650 V, which is typically achieved with insulating tapes. Hence a transformer with a single layer primary and single layer secondary was considered, with the secondary winding wound over the primary with an insulating tape layer in between. A schematic view of the transformer construction is shown in Fig. 4.2.

Since a high square-wave voltage is expected at the input, the peak input voltage of about 450 V was assumed for the transformer. For a transformer with such square-wave voltage, the turns are decided by the following expression to keep the peak flux density

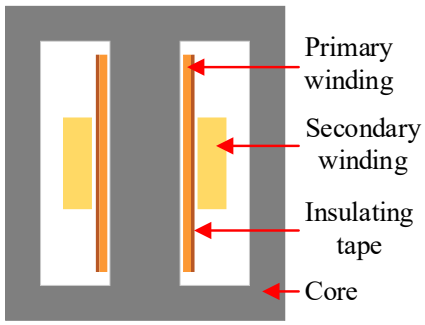

Fig. 4.2: Pictorial view of the current boost transformer.

Table 4.2: Design and setup parameters for proof-of-concept constant voltage input underwater IPT system.

Parameter	**Values**
L_p	7.25 µH
L_s	2.91 µH
k	0.32
C_p	36.8 nF
C_s	136 nF
m	5
$N_{p,tr}$, $N_{s,tr}$	50, 10
Core	0R49928EC
Q_1-Q_4	C2M1000170D, 1700 V, 5 A
D_1-D_4	APT30S20B(G), 200 V, 45 A
L_{za}	50 µH

below a desired level B_{max}:

$$N \geq \frac{V_{pk}}{A_{core} f_s B_{max}} \ , \tag{4.8}$$

where A_{core} is the core cross-section area perpendicular to the flux path. The flux density is typically kept below 50 mT to minimize core losses at high frequency. A high-voltage transformer core available in lab was used with material 0R from Magnetics Inc., which with a choice of 50 turns in the primary keeps the maximum flux density to 12 mT. Correspondingly the secondary turns were selected as per the desired ratio. The transformer parameters are mentioned in Table 4.2.

4.3.1 Tank Quality Factor Considerations

The steady-state analysis presented in Chapter 3 demonstrates that the constant voltage characteristics are obtained when the fundamental harmonic approximations are applicable. As the system consists of two resonant tanks, their quality factors determine how sinusoidal the currents are expected to be. With the secondary tank quality factor (Q_{sl})

presented in Chapter 3, it can be identified that Q_{sl} increases with load. Hence the secondary tank has higher harmonics during lower power operating points. Further, the diode rectifier goes into discontinuous conduction mode (DCM) at very light loads, leading to further deviations in output voltage from the expression derived in Chapter 3 [123].

On the other hand, the primary tank loaded quality factor can be expressed as

$$Q_{pl} = \frac{Z_{op}}{Z_r} \ , \tag{4.9}$$

which, at the tuned operating point, transforms to

$$Q_{pl} = \frac{\omega L_p R_e}{\omega M^2} = \frac{1}{k^2 Q_{sl}} \ , \tag{4.10}$$

which shows that it is inversely proportional to Q_{sl}. So the primary tank is expected to have non-sinusoidal currents at higher load. To maintain appreciably high quality factors in both tanks, the system was operated in the load range of 75 W to 310 W, with operations in the range 34 W to 75 W were conducted to show the diode rectifier operating in DCM. The corresponding variation in tank quality factors and total harmonic distortion in the tanks are shown in Fig. 4.3, which shows that in the power range 75 W to 310 W the tanks maintain appreciable quality factors and below 10 % current THD.

4.3.2 Component Sizing

The same expressions used in the sizing of the components are applicable for this design. As higher voltage is expected for this setup on the input side, higher voltage switches using silicon carbide (SiC) devices were used. The same diode rectifier as the voltage input IPT system was used for this work, as this too had a low output voltage. The devices used in the setup are mentioned in Table 4.2. In addition, ZVS was ensured for all devices, using active ZVS assistance for the leading inverter leg A with phase shift control [104]. The ZVS

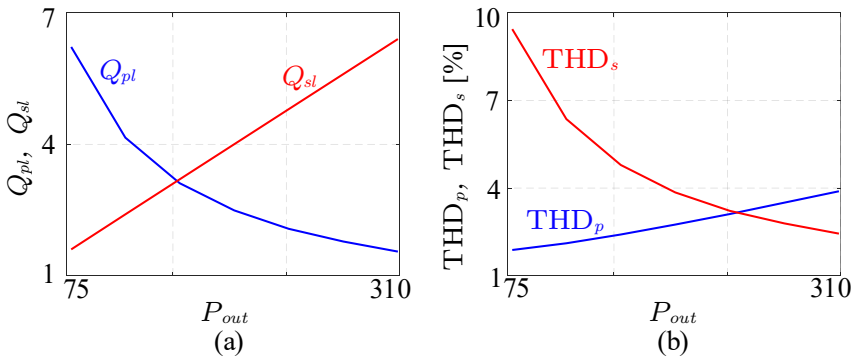

Fig. 4.3: Simulated plots of tank quality factors and current total harmonic distortions over P_{out} in the range 75 W to 310 W (a) Q_{pl} and Q_{sl} vs P_{out}, (b) THD_p and THD_s vs P_{out}.

assistance requirement and corresponding value of ZVS assistance inductor (L_{za}) was found from the primary tank waveforms as per the method in [104]. The setup parameters and the value of L_{za} is also shown in Table 4.3.

4.4 Design Considerations for the Transformer-less Constant DC Current Input Underwater SS IPT System

For the design of the transformer-less topology up to 1 kW with 75 V output, the effect of the tank parameters are more carefully considered, such that the constant voltage characteristics can be maintained with high operating efficiency and lower volume of the coils. For this, the generalized analysis with under the mistuned conditions are used from Chapter 3, such that effect of misalignment can be addressed. The considerations include the choice of range of inverter phase angle (φ_{AB}) to keep desired current to voltage conversion ratio under different misalignment conditions, the Volt-Ampere (VA) rating of the coils, discontinuous conduction mode of the rectifier, the output power characteristics with change in load impedance and component sizing for worst case operating conditions.

4.4.1 Input Current to Output Voltage Gain Considerations

Similar to the design of the transformer-based topology, the first consideration is to achieve the required constant dc current to constant dc voltage conversion ratio. From the output voltage expression of the transformer-less topology with mistuning in Chapter 3 the

input current to output voltage gain (Z_t) can be expressed as

$$Z_t = \frac{\pi^2 \omega M \sqrt{1+G^2}}{8\sqrt{1+{Q_{sl}}^2\left(F_s - \frac{1}{F_s}\right)^2}\sin\left(\frac{\varphi_{AB}}{2}\right)} \ , \tag{4.11}$$

where G is as expressed in (3.20) in Chapter 3. Notably, Z_t is a function of the mutual inductance (M), the normalized switching frequencies of the primary and secondary tanks (F_p and F_s), the secondary tank loaded quality factor (Q_{sl}) and the control input φ_{AB}. To ensure a desired Z_t, variations in these quantities owing to misalignment, load changes and component tolerances are needed to be considered. The upper limit of φ_{AB} is 180°, but the lower limit ($\varphi_{AB,min}$) can be chosen based on the maximum current capability of the primary coil ($I_{p,max}$). Hence the design requirements for selecting the band of mutual inductances to obtain a desired current to voltage gain (Z_{td}) can be summarised as

$$M_{max} \leq \frac{8Z_{td}\sqrt{1+{Q_{sl}}^2\left(F_s - \frac{1}{F_s}\right)^2}}{\pi^2\omega\sqrt{1+G^2}} \ , \tag{4.12}$$

$$\varphi_{AB,min} = 2\sin^{-1}\left(\frac{\pi I_{in}}{2\sqrt{2}I_{p,max}[\cos(\varphi_p)]_{min}}\right) \ , \tag{4.13}$$

$$M_{min} \geq \frac{8Z_{td}\sqrt{1+{Q_{sl}}^2\left(F_s - \frac{1}{F_s}\right)^2}\sin\left(\frac{\varphi_{AB,min}}{2}\right)}{\pi^2\omega\sqrt{1+G^2}} \ , \tag{4.14}$$

where (4.12) is to be satisfied at the lowest power operating point and (4.13)-(4.14) are to be satisfied at the full power operating point. Sufficient mutual inductance is required in this case as the current boost transformer is not present in this topology. Hence this design requires large number of turns on the primary coil wound with thinner wires, such that a large inductance can be obtained with small coils.

4.4.2 Coil VA Considerations

The coil VA ratings are carefully considered in this design to optimize the copper

volume of the system. Larger VA requirements of the coils require larger inductances, and hence larger coils. Hence the coil VA ratings determine the copper volume of an IPT system. The coil VA ratings are determined by the output power and the coil loaded quality factors. It is typically beneficial to minimize the coil VA at the nominal load, as that gives the best volume density. The coil VA ratings (S_p and S_s) can be expressed in terms of the output power and the quality factors as

$$S_s = Q_{sl} P_{out} \ , S_p = Q_{pl} P_{out} \ , \tag{4.15}$$

where using the relations between Q_{pl} and Q_{sl} from (4.10), the total VA rating of the coils are obtained as

$$S_{tot} = S_s + S_p = \left(Q_{sl} + \frac{1}{k^2 Q_{sl}} \right) P_{out} \ . \tag{4.16}$$

Differentiating the above expression with Q_{sl} and equating it to zero, the condition for total minimum VA rating is obtained as

$$Q_{sl} = \frac{1}{k} \ . \tag{4.17}$$

It is interesting to note that the condition derived in (4.17) coincides with the selection of nominal operating conditions in typical WPT systems with identical primary and secondary coils to ensure maximum efficiency [3]. Hence the choice of minimizing total VA rating at nominal power is expected to help the system attain peak efficiency near the nominal load.

4.4.3 Discontinuous Conduction Mode Considerations

The tank quality factor conditions and the occurrence of DCM conditions considered

briefly during the transformer-based design is applicable for this topology as well, since the operations are similar. Even though synchronous rectification is used, it is not possible to avoid DCM without multi-angle control, which is challenging in WPT. The DCM causes a zero interval in the secondary tank current, causing the output voltage to go higher than the fundamental harmonic approximation (FHA) predicted values [123]. However the quality factor analysis is insufficient to explain the loads where DCM occurs, as time-domain analysis is required [123]. This is considered in the design of the transformer-less constant current input SS IPT topology to ensure a wide range of output power where DCM is not encountered even with choosing the smallest possible coils.

While applying the VA consideration and the DCM consideration to the design of the system, it is found that they are contradictory to each other. Equation (4.17) suggests that higher couplings, typically targeted in IPT system designs for higher efficiencies [71], require the Q_{sl} to be lower for minimizing VA at a desired output power point. However lower secondary quality factors are prone to driving the system to DCM [123]. Hence a figure of merit (FOM) as shown in (4.18) is introduced for the design of this system:

$$\text{FOM} = \frac{P_{S,min}}{P_{th,DCM}} \ , \tag{4.18}$$

where $P_{S,min}$ represent the load where the coils minimize the total VA required as per (4.17) and $P_{th,DCM}$ represent the load threshold below which the secondary goes into DCM according to [123]. Plots of variation of $P_{S,min}$, $P_{th,DCM}$ and FOM with respect to different secondary coil inductances (L_s) are shown in Fig. 4.4, where lower L_s corresponds to lower Q_{sl}.

From the plots in Fig. 4.4, it can be identified if lower L_s is used for higher $P_{S,min}$, CCM operation with sinusoidal secondary tank current cannot be maintained in the desired load range of P_{min} to P_{max}. If higher L_s is chosen to rectify that, $P_{VA,min}$ falls such that the coils do not minimize total VA at the maximum power point. However, under this condition, using a lower k, FOM can be maximized, such that $P_{th,DCM}$ is sufficiently below

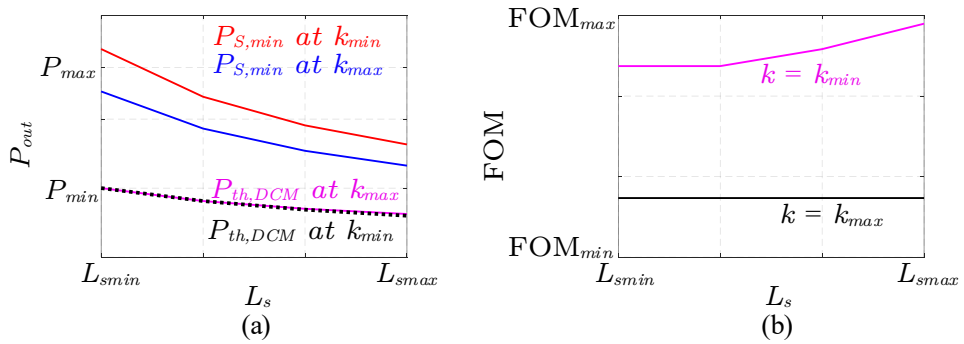

Fig. 4.4: Plots to demonstrate characteristics of $P_{S,min}$, $P_{th,DCM}$ and FOM with L_s and k (a) $P_{S,min}$ and $P_{th,DCM}$ vs L_s for different k, (b) FOM vs L_s for different k.

P_{min} and $P_{VA,min}$ is as close to P_{max} as possible. This ensures both the VA and DCM considerations are properly met to ensure constant voltage characteristics with minimized volume and higher efficiency.

4.4.4 Output Power Considerations and tolerance analysis

Another aspect of an output voltage regulated system is that, with an increase in load resistance the dc output power should decrease, and the opposite is true for decrease in load resistance as well. Hence for the constant voltage regulated operation

$$\frac{dP_{out}}{dR_l} < 0 \ . \tag{4.19}$$

With the expression of secondary tank quality factor as defined by (3.10), the above expression can also be transformed as

$$\frac{dP_{out}}{dQ_{sl}} > 0 \ . \tag{4.20}$$

Using this expression, the load range where system strictly demonstrates voltage regulated operation can be determined. Further manipulation of (4.20) leads to the relation for

voltage regulated mode as

$$Q_{sl}{}^2 > \frac{\left(F_p - \frac{1}{F_p}\right)^2}{K_1 - K_2 + K_3} \ , \tag{4.21}$$

where the terms in the denominator are formulated as

$$K_1 = \frac{k^2 F_p F_s}{Z_{op} Z_{os}} \ , \tag{4.22}$$

$$K_2 = \frac{2\left(F_p - \frac{1}{F_p}\right)\left(F_s - \frac{1}{F_s}\right)}{Z_{op} Z_{os}} \ , \tag{4.23}$$

$$K_3 = \left(F_p - \frac{1}{F_p}\right)^2 \left(F_s - \frac{1}{F_s}\right)^2 \ . \tag{4.24}$$

Equation (4.21) demonstrates the condition to maintain constant voltage output characteristics for any load and power factor, provided that DCM is not occurring. It is also useful to find the effects of the component tolerances on the output voltage. These effects are shown in the plots in Fig. 4.5(a)-(d). The normalized deviation in output voltage ($\Delta V_{o,n}$) over the load range P_{min} to P_{max} deviations in F_p is shown in Fig. 4.5(a), whereas the same characteristics with deviation in F_s is shown in Fig. 4.5(b). Then, the plot of required Q_{sl} to achieve constant voltage output with variations in F_p is shown in Fig. 4.5(c) while keeping constant F_s of unity and the plot of ratio of Q_{sl} required and achieved from the circuit under different power conditions keeping $F_p = 1.005$ is shown in Fig. 4.5(d). The typical ranges of change in inductances and capacitors in an IPT system are considered for these plots.

The plots demonstrate that for approximately $0.995 < F_p < 1.005$, nearly constant voltage characteristics is achieved, which corresponds to (3.52) and (4.21). Also, when a low deviation in F_p is present, choice of F_s near unity helps in constant voltage characteristics. Operating at F_p and F_s near unity also helps in avoiding non-zero minimum power transfer through such constant current input systems [62]. Hence the coil quality factors are chosen

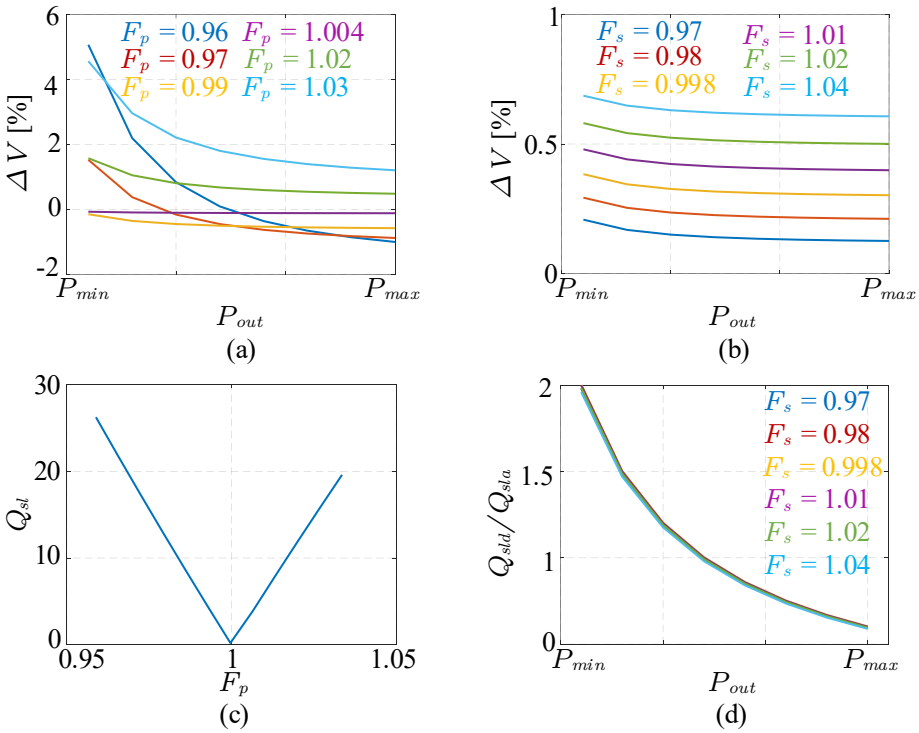

Fig. 4.5: Tolerance analysis plots (a) $\Delta V_{o,n}$ vs P_{out} with varying F_p and fixed $F_s = 1$, (b) $\Delta V_{o,n}$ vs P_{out} with varying F_s and fixed $F_p = 1.005$, (c) Required Q_{sl} vs F_p for fixed $F_s = 1$ to keep constant voltage characteristics, (d) Ratio of required and achieved values of (Q_{slc}/Q_{sla}) vs P_{out} with varying F_s and fixed $F_p = 1.005$.

from the VA rating and DCM conditions, whereas the capacitors are carefully chosen with lowest possible tolerances to keep the effects of mistunings low.

4.4.5 Component Sizing

Another important part of the design are sizing of components, which help in the realizing the design in practice. This includes the values of the components and their electrical ratings for worst case operation.

The coil inductances L_p and L_s are decided from the current to voltage conversion ratio and quality factor considerations. Since the compensation capacitors compensate the reactive powers at the resonant frequency, their values are obtained as

The capacitor and coil voltages can be obtained from the equivalent circuits in Fig. 3.6 in Chapter 3 by considering the time-domain waveforms in Fig. 3.5 in Chapter 3. The time-domain tank current expressions can be written as

$$i_p = \sqrt{2} I_p \cos(\omega t - \varphi_p) \ , \tag{4.25}$$

$$i_s = \sqrt{2} I_s \cos\left(\omega t + \frac{\pi}{2} - \varphi_p - \varphi_s\right) \ . \tag{4.26}$$

From them, the time-domain expression of the capacitor voltages, shown in Fig. 4.6, are obtained as

$$v_{cp} = \frac{i_p}{j\omega C_p} = V_{cp,pk} \cos\left(\omega t - \frac{\pi}{2} - \varphi_p\right) \ , \tag{4.27}$$

$$v_{cs} = \frac{i_s}{j\omega C_s} = V_{cs,pk} \cos\left(\omega t - \varphi_p - \varphi_s\right) \ , \tag{4.28}$$

with the peak capacitor voltages following the same relations in (4.4). Using them, the coil voltages can be obtained as

$$v_p = v_{AB} - \frac{\sqrt{2} I_p}{\omega C_p} \cos\left(\omega t - \frac{\pi}{2} - \varphi_p\right) \ , \tag{4.29}$$

$$v_s = \frac{\sqrt{2} I_s}{\omega C_s} \cos\left(\omega t - \varphi_p - \varphi_s\right) + v_{DE} \ , \tag{4.30}$$

where v_{AB} and v_{DE} functions are defined by the square waves in Fig. 3.5. Since this is a series-series topology, the coil and capacitor rms current ratings on both primary and secondary tanks are equal to the tank rms currents. The worst case primary currents are obtained at the minimum inverter phase angle ($\varphi_{AB,min}$), whereas the worst case secondary tank is obtained at the peak load of 1 kW, which is also the nominal output power (P_{nom}). So the current ratings for the tank elements are found as

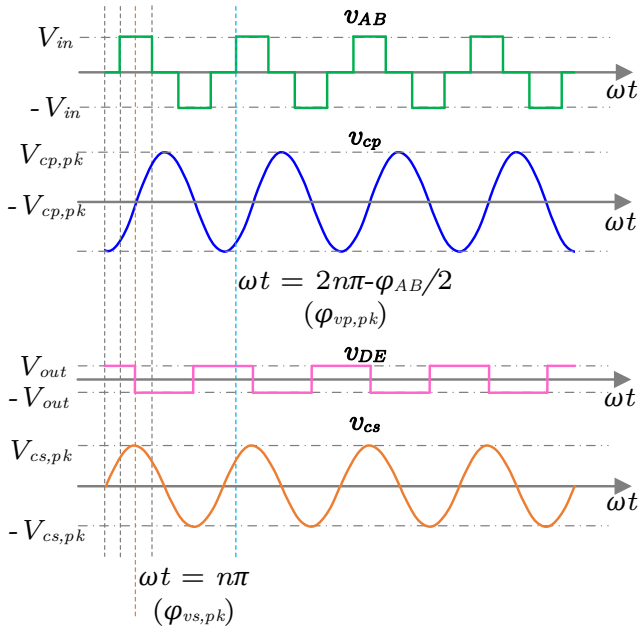

Fig. 4.6: Waveforms of inverter voltage (v_{AB}), primary capacitor voltage (v_{cp}), rectifier voltage (v_{DE}) and secondary capacitor voltage (v_{cs}), showing time instants where the peak coil voltages are reached.

$$I_{p,rat} = \frac{\pi I_{in}}{2\sqrt{2}\sin\left(\frac{\varphi_{AB,min}}{2}\right)\cos(\varphi_p)} \ , \tag{4.31}$$

$$I_{s,rat} = \frac{\pi P_{nom}}{2\sqrt{2}V_{out}} \ . \tag{4.32}$$

The peak capacitor voltages are also obtained during the rms currents at the above values, which define the capacitor voltage ratings as

$$V_{cp,rat} = \frac{\sqrt{2}I_{p,rat}}{\omega C_p} \ , v_{cs,rat} = \frac{\sqrt{2}I_{s,rat}}{\omega C_s} \ . \tag{4.33}$$

Since the input voltage is load and phase angle dependent, the peak input voltage will be obtained at the nominal output power, given by

$$V_{in,pk} = \frac{P_{nom}}{I_{in}} \ . \tag{4.34}$$

Using (4.33)-(4.34) and the value of V_{out}, the peak coil voltages can be obtained from their time-domain expressions and their waveforms shown in Fig. 4.6 as

$$V_{p,pk} = V_{in,pk} + V_{cp,rat} \cos\left(\frac{5\pi}{2} - \frac{\varphi_{AB,min}}{2} - \varphi_p\right) \ , \tag{4.35}$$

$$V_{s,pk} = V_{cs,rat} \cos\left(\varphi_p + \varphi_s\right) + V_{out} \ , \tag{4.36}$$

with v_p reaching its peak at $\omega t = 2n\pi - \frac{\varphi_{AB,min}}{2}$ and v_s reaching its peak at $\omega t = n\pi$, as marked in Fig. 4.6.

The primary bridge switches are driven at 50 % duty ratio with symmetrical phase shift modulation. The secondary bridge, at nominal power operating point, works as a synchronous rectifier in continuous conduction mode (CCM). Hence the secondary switches also can be also assumed to operate with a duty ratio of 50 %. Also, both tanks can be considered operating with sinusoidal currents at the rated rms current conditions, as per CCM synchronous rectification. With them in place, the device current ratings can be obtained as

$$I_{qp,rat} = \frac{I_{p,rat}}{\sqrt{2}} = \frac{\pi I_{in}}{4 \sin\left(\frac{\varphi_{AB,min}}{2}\right) \cos(\varphi_p)} \ , \tag{4.37}$$

$$I_{qs,rat} = \frac{I_{s,rat}}{\sqrt{2}} = \frac{\pi P_{nom}}{4 V_{out}} \ . \tag{4.38}$$

The peak voltage across the primary switches are determined by the input voltage at nominal power output, while the peak voltage across the secondary switches are essentially the output voltage. Hence the device voltage ratings are obtained as

$$V_{qp,rat} = V_{in,pk} = \frac{P_{nom}}{I_{in}} \, , V_{qs,rat} = V_{out} \, . \tag{4.39}$$

4.4.6 Application of the above considerations to the 1 kW system design

The main design areas where all the considerations were required to consider was the coil designs. From the specifications, the current to voltage conversion ratio was found as 75 Ω. The nominal design was chosen to operate as close as possible to φ_{AB} of 120 deg to avoid injection of the third harmonic component in v_{AB}, similar to the transformer-based topology design. Based on that, target mutual inductance value was decided. Then electromangetic simulations were performed with different coil dimensions to find out inductances for nominal and misaligned conditions. A 2D view of the model in nominal position with no misalignment is shown in Fig. 4.7. Both circular and square coils were used in the simulations, with primary coils having diameter in the range of 150 mm to 210 mm (side length in case of square coils) and secondary coils having diameter in the range of 90 mm to 120 mm (side length in case of square coils). The simulations were performed both in air and immersed in seawater in the Ansys environment to monitor the effect of the ac resistances of the coil in seawater. Among competitive designs having similar inductances, the ones achieving lower ac loss resistance were considered for evaluation of the other design constraints.

For getting the maximum inductance, a 10 % reduction in gap with full alignment wass considered, whereas for weakest coupling position a 10 % misalignment in X direction and 10 % increase in gap were considered together. For optimization of ac resistances of the coils and coil dimensions, AWG#18 litz wire was selected for the primary and AWG#10 litz wire was selected for the secondary, each constructed with multiple AWG#42 or smaller guage strands [116,125]. Then from its current capability, and using (4.13)-(4.14), the system was designed to operate always above $\varphi_{AB,min}$ of 70°. The designs which were satisfying these limits are considered for the next steps.

For each design that satisfies the above, the power is calculated where the simulated

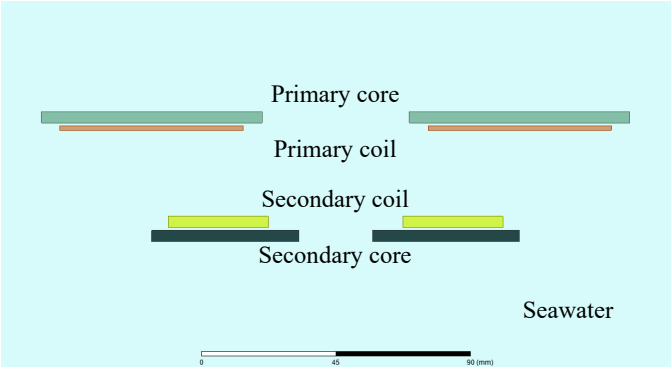

Fig. 4.7: Ansys Maxwell model of simulated coils in seawater - 2D equivalent representation of 3D model.

secondary inductance minimizes total coil VA rating. Also, for each of these designs it is noted if the required minimum operating power is below the point where the secondary tank goes to DCM, using the tool associated with [123]. From these, the value of FOM for each design is evaluated as per (4.18). The selected design minimizes VA at 510 W but does not go into DCM above 150 W. This ensures mostly sinusoidal secondary tank current in the desired load range of 300 W to 1000 W, where constant voltage characteristics are required for the application. The inductance parameters of the selected design with circular pads are shown in Table 4.3, which were constructed with 54 turns in the primary coil and 11 turns in the secondary coil.

The compensation capacitors were found for full compensation at 250 kHz under the nominal gap and alignment conditions. The capacitor values are also provided in Table 4.3. Then, the current and voltage requirements of the capacitors, coils and devices were found from (4.31)-(4.39) at the worst cases, which occur at nominal power with worst case coupling. The required voltages of the capacitors are also mentioned in Table 4.3. The maximum coil voltage per turn are verified for both coils, which were found to be much below the maximum.

For selecting capacitors, sufficiently large packages and derating with frequency were considered. This ensures that the capacitors do not contribute to excessive losses while operating at 250 kHz. The stability of capacitance with voltage and frequency were also

Table 4.3: IPT system design and setup parameters.

Parameter	**Values**
L_p	403 µH
L_s	14.5 µH
k (Nominal)	0.395
k (Maximum)	0.429
k (Minimum)	0.335
M (Nominal)	30.2 µH
M (Maximum)	33.2 µH
M (Minimum)	25.4 µH
C_p	966 pF
$V_{cp,rat}$	2 kV
C_s	26.5 nF
$V_{cs,rat}$	400 V
L_{za}	110 µH
Q_1-Q_4	C2M1000170D, 1700 V, 5 A
Q_5-Q_8	IRFS4115TR, 150 V, 99 A

considered, and so C0G/NP0 type ac capacitors with tightest possible tolerances were chosen to ensure the resonant tuning does not shift too much during operation.

According to the device rating expressions, Silicon carbide (SiC) devices from Cree (Part No. C2M1000170D) with 1700 V rating were selected for the primary bridge and 150 V Silicon devices were used for the secondary bridge. To improve efficiency of the system, two parallel devices were used for each switch in the circuit on both primary and secondary sides. In addition, zero voltage switching (ZVS) was ensured for all devices by using ZVS assistance in leg A with phase shift control [104]. The ZVS assistance requirement and corresponding value of ZVS assistance inductor (L_{za}) was found from the primary tank waveforms as per the method in [104]. The setup parameters and the value of L_{za} is also shown in Table 4.3.

4.4.7 Thermal Management

Thermal management is a critical aspect of power electronic converter designs, such

that even with the maximum power loss conditions the components can operate at safe temperatures. To reduce power dissipation per device, each switch was designed with two parallel devices, ensuring best current sharing such that thermal runaway can be avoided. For the primary bridge with high-voltage clearance requirements, through-hole devices were used in both top and bottom layers with sufficient spaces in between for heat-sink mounting and air flow. On the secondary board, surface mount devices with PCB bottom mounted heat sinks were used. Large copper planes were also kept exposed for better heat dissipation. Forced air cooling was used, such that temperatures can be maintained near room temperature even at peak load.

During our tests, no heat-sinks were used with the coils, as they were operated within a saline water tank. The water environment around the coils helps in cooling. In real designs, an aluminum plate can be used as shield as well as heat sink on the pad back-side, with some in-house air flow directed towards them for better cooling arrangements.

The next chapter proceeds with the small-signal modeling of the constant dc current input SS IPT topologies, before presenting the experimental results in Chapter 6.

CHAPTER 5

Small-signal Modeling of the Constant Current Input Underwater IPT Systems

While the analysis and design considerations presented in Chapter 3 and Chapter 4 define the steady-state performances of the constant dc current input underwater IPT systems, their small-signal modeling is necessary for understanding their dynamic characteristics. These are helpful to design proper control loop for them, so that they can be operated stably with a desired control bandwidth. This dissertation work focuses on the small-signal model development for the proposed constant current input IPT systems, including both the transformerless and transformer based designs. As it was shown in Chapter 3, the effect of the transformer is only seen in the primary current and output voltage magnitudes. Hence, this chapter proceeds with the small-signal modeling for the transformerless design, while the corresponding expressions for the transformer based design are mentioned with careful consideration of the transformer turns ratio m.

Review of different small-signal analysis tools were presented in Chapter 1, which demonstrated that the resonant topologies typically use generalized state-space averaging (GSSA) [18, 109, 126], extended describing function (EDF) [69, 111] or small-signal phasor modeling [61, 67, 68, 113]. This chapter shows which of these are most applicable for the proposed constant current input SS IPT system, and then derives the transfer functions through necessary circuit manipulations.

5.1 Selection of Small-Signal Modeling Technique for the Proposed Underwater IPT Topologies

As per the equivalent circuits presented in Chapter 3 for the proposed underwater IPT topologies, they involve two series resonant tanks coupled through the IPT coils. Moreover, the steady-state analysis and designs demonstrate that it is beneficial to design both tanks for operating at resonance, and select component tolerances such that the resonant condi-

tions do not get disturbed sufficiently over a wide load range. Hence for the small-signal modeling purposes, both tanks can be considered as series resonant tanks operating at or near resonance.

Now, it was shown in Chapter 1 that among the small-signal analysis tools, the small-signal phasor modeling technique provides the best insights into a series resonant converter. Further, a number of approximations can be applied when the series resonant tank is at or near resonance [61,67,113], as shown in Fig. 5.1. The second order approximation model is applicable for near resonance, where the tanks can be approximated as a first-order system, which makes the analysis much easier. Hence for the topologies proposed in this dissertation, the small-signal phasor modeling method is adapted.

However the models from the existing systems cannot be directly employed, as they do not have any considerations for mutual inductances. In a few works for secondary side analysis for constant voltage input SS IPT system, the IPT coils are modeled using the transformer model, which does not clearly allow for applying the approximations as per the series resonant network [68]. Moreover that model is not applicable for a constant current input system, where considerations similar to [61] is required. In this work, the mutual inductance model is used and its small-signal behavior is analyzed along with the series resonant tank models and considerations for the constant input current. Hence the model development and derivation of transfer functions proceed with the following key steps

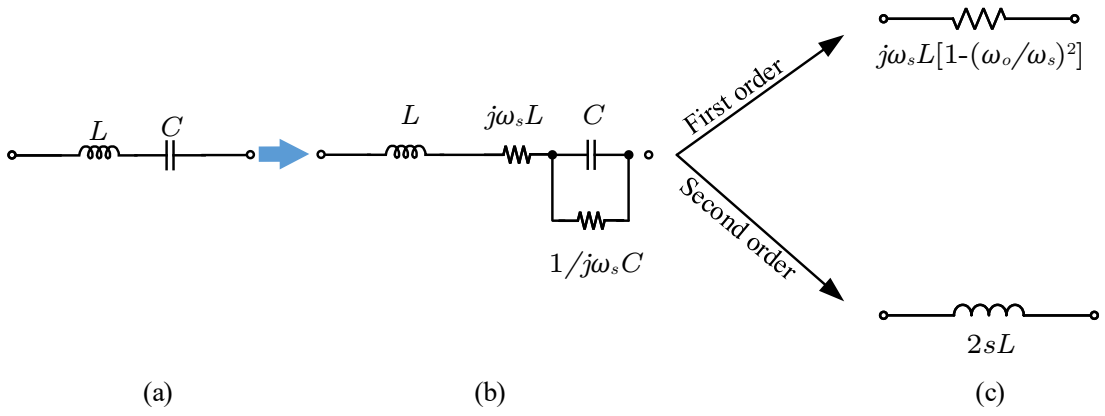

Fig. 5.1: Simplifications applicable to small-signal model of a series resonant tank.

- Brief overview of the phasor transformation blocks useful for this work
- Small signal model development of the resonant tanks as voltage input
- Analysis of the mutual inductance effect
- Considerations for the constant current input

5.2 Phasor Transformations and Small-signal Model Derivations

At the first step, the phasor transformations of the different blocks and small-signal models of the basic circuit elements are re-visited from Chapter 1 and properly modified to fit with the quantities of the constant current input underwater SS IPT topologies, while considering the IPT tank as a constant voltage input system. Then the mutual inductance effect is modeled through applying the small-signal assumption carefully. Further the small-signal model of the input side is considered such that the effects of the constant current input and the phase shift angle φ_{AB} as control input can be found.

5.2.1 Phasor transformations of inverter and rectifier stages

In the phasor transformations, each switching frequency ac quantity in the system is represented by its phasor bearing its instantaneous rms value, e.g. the phasor $\vec{i}_p$ standing for primary coil current (i_p). The phasor transformed model of the voltege-fed full bridge inverter in the transformerless constant current input SS IPT topology follows directly from the forms shown in Chapter 1, which converts the input voltage (V_{in}) to the inverter output voltage phasor ($\vec{v}_{AB}$). In the transformer based topology, the transformer ratio of m:1 is taken as part of the inverter phasor transformation to generate the tank input voltage phasor ($\vec{v}_{AB}$). For the sake of clarity, the phasor transformer models applicable for the inverter stages of these topologies are shown in Fig. 5.2(a)-(b), using the corresponding transformation ratios $\vec{s}_p$ and $\vec{s}_{pt}$, given as

$$\vec{s}_p = \frac{\vec{v}_{AB}}{V_{in}} = \frac{2\sqrt{2}}{\pi} \sin\left(\frac{\varphi_{AB}}{2}\right) \ , \tag{5.1}$$

$$\vec{s}_{pt} = \frac{\vec{v}_t}{V_{in}} = \frac{2\sqrt{2}}{m\pi} \sin\left(\frac{\varphi_{AB}}{2}\right) \ . \tag{5.2}$$

As the MOSFET based full-bridge rectifier with capacitive filter is operated as synchronous rectifier to emulate a diode rectifier behavior in the transformerless topology, its transformation also follows the rectifier transformation shown in Chapter 1. Similar relation is applicable for the transformer based topology using diode rectifiers. For the sake of clarity, the transformer models applicable for the rectifier stages of these topologies are shown in Fig. 5.2(c)-(d) using the transformation ratio

$$\vec{s}_s = \frac{\vec{v}_{DE}}{V_{out}} = \frac{2\sqrt{2}}{\pi} \ . \tag{5.3}$$

5.2.2 The small-signal assumption

For the small-signal model, small variations above the steady-state quantities are considered. Hence, the variations in a dc signal x_y and a phasor $\vec{x}_y$ are represented as

$$x_y = X_y + \hat{x}_y \ , \tag{5.4}$$

$$\vec{x}_y = X_y + \hat{\vec{x}}_y \ . \tag{5.5}$$

where the quantities $\hat{x}_y$ and $\hat{\vec{x}}_y$ represent the small-signal variations. The following are the important assumptions

- The perturbation amplitudes are infinitesimal compared to the switching frequency quantities manifested in form of the phasor RMS values, i.e. $|\hat{\vec{x}}_y| \ll X_y$

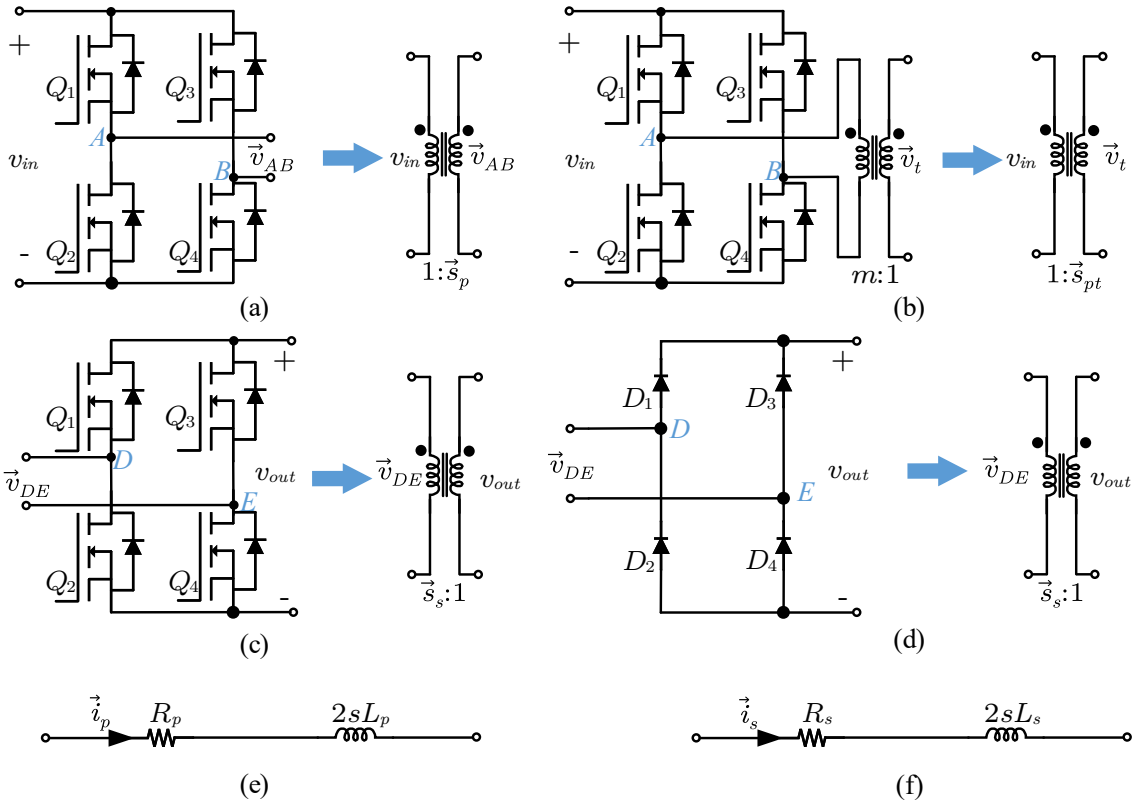

Fig. 5.2: Phasor transformations for the constant current input SS IPT topologies (a) Inverter for transformerless topology, (b) Inverter for transformer based topology including current boost transformer, (c) Synchronous rectifier used in the transformerless topology, (d) Diode rectifier used in the transformer based topology, (e) Primary tank, (f) Secondary tank .

- The phasor frequency s is lower compared to the switching frequency ω, i.e. $|s| \ll \omega$ [68], with an upper limit of $\left(\frac{\omega_s}{2}\right)$ owing to natural sampling induced by the power converter switching

5.2.3 The passive components and the IPT network

Among the passive components, the input and output capacitors do not operate near resonance, and their dynamics at the phasor frequency are important for the small signal model. Hence their phasor frequency models are considered. The tank components are transformed for the small signal model as per the techniques reviewed in Chapter 1. As operation is considered at resonance for both tanks, the second order approximation of series resonant tank is applied for both. Hence, the series combination of L_p and C_p in the primary tank is represented as $2sL_p$, and the series combination of L_s and C_s in the secondary tank is represented as $2sL_s$. Since the resistors stay as resistors in the phasoe domain, the primary tank ESR stays as R_p in the model and the secondary tank ESR stays as R_s in the model. The transformed forms of the primary and secondary tanks are shown in Fig. 5.2(e)-(f).

5.2.4 Model of the mutual inductance

The T-equivalent model of the IPT coils and subsequent approximations are applied in [68] to model the effect of the mutual inductance, but this leads to additional complications as the above series resonant tank approximations cannot be directly applied. Hence the mutual inductance model is used to simplify the model. For this, the mutual inductance equivalent circuit presented in Chapter 3 are considered along with the phasor representations of the coil quantities $\vec{v}_{oc}$, $\vec{v}_r$, $\vec{i}_p$ and $\vec{i}_s$. Using the basic principle of the mutual inductance, the induced voltage expression in phasor domain can be written as

$$\vec{v}_{oc} = M\frac{d\vec{i}_p}{dt} + j\omega_s M\vec{i}_p \ . \tag{5.6}$$

Transforming to Laplace domain, its small-signal version can be written as

$$\hat{\vec{v}}_{oc} = sM\hat{\vec{i}}_p + j\omega_s M\hat{\vec{i}}_p \ . \tag{5.7}$$

Applying the small signal approximations to (5.7), the first term can be neglected with comparison to the last. Hence the small-signal perturbation in secondary coil induced voltage can be written as

$$\hat{\vec{v}}_{oc} \approx j\omega_s M\hat{\vec{i}}_p \ . \tag{5.8}$$

The above expression indicates that the steady-state model of the mutual inductance action, as shown in the equivalent circuit in Chapter 3, is sufficient for the small-signal model. Hence, for the small-signal model, the two coupled resonant compensation tanks can be replaced by their individual small-signal phasor models, and the effect of the mutual inductance will be through the steady-state reflected impedance in the primary tank and the steady-state induced voltage in the secondary tank.

5.2.5 Derivation of the small-signal model

The small-signal model of the IPT tank is obtained by plugging in these phasor transform blocks and considering small-signal variations above the steady-state phasor quantities, which is shown in Fig. 5.3. The small-signal input to the tank is $\hat{\vec{v}}_{AB}$ for the transformerless topology, whereas it is $\hat{\vec{v}}_t$ for the transformer based version.

Now, the load side phasor transformer is appended to the small-signal model to get the full system small signal model. It is so, as the load side phasor transformer conversion ratio does not depend on any small-signal variation. Hence the conversion ratio stays same for small-signal behaviors. The model is shown in Fig. 5.4.

The input side transformer cannot be directly appended to this model, as the conversion

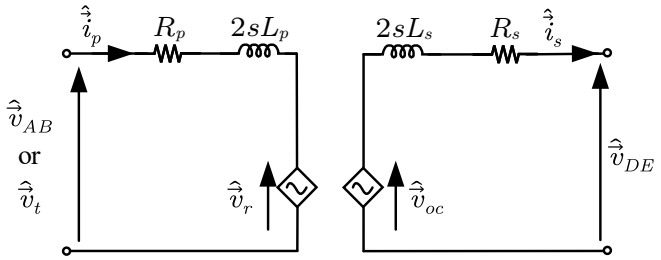

Fig. 5.3: Small-signal phasor model of the underwater SS IPT compensation network.

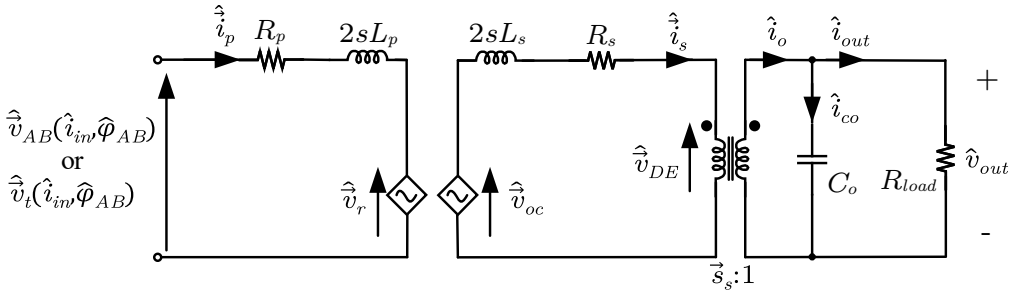

Fig. 5.4: Small-signal phasor model of the dc constant current input underwater SS IPT system.

ratio involves φ_{AB}, whose small-signal change ($\hat{\varphi}_{AB}$) is the control input and needs to be considered. This is done through small-signal analysis of the inverter phasor transformer, to obtain the small-signal representation of the IPT network input voltage as function of small-signal variation in input current $\hat{i}_{in}$ and $\hat{\varphi}_{AB}$, as indicated in Fig. 5.4.

To achieve the above, the small-signal analysis of the input side is also required, which is performed through the input side model as shown in Fig. 5.5. This is so as the small-signal input to the inverter phasor transformer $\hat{v}_{in}$ is not an independent input due to the constant current input configuration. So the input side model is used to get $\hat{v}_{in}$ in terms of $\hat{i}_{in}$ and $\hat{\varphi}_{AB}$, as indicated in Fig. 5.5.

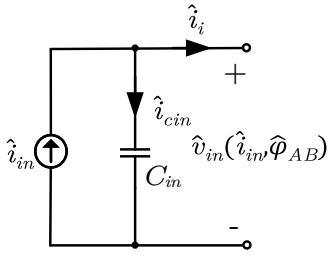

Fig. 5.5: Small-signal phasor model of the input side to take care of the dc constant current input configuration.

5.3 Determination of the Transfer Functions

This section derives the transfer functions between the small-signal variations in output voltage ($\hat{v}_{out}$) and inverter phase angle ($\hat{\varphi}_{AB}$), as the system is designed to operate in voltage regulated operation. During the process the transfer function for the primary current is also developed, which too demonstrate critical dynamic behaviors. As per the models presented above, the derivation proceeds with developing the expressions considering the system as a voltage input system using Fig. 5.4. Then the input side is considered using Fig. 5.5.

5.3.1 Analysis of small-signal tank impedances

At the first step of derivation of the transfer functions, the small-signal tank impedances are obtained from Fig. 5.4. Using the phasor transformation for the rectifier, the reflected load impedance seen by the secondary tank is obtained as

$$Z_{lss} = (\vec{s}_s)^2 \frac{R_{load}}{1 + sC_o R_{load}} = \frac{R_e}{1 + sC_o R_{load}} \ . \tag{5.9}$$

Using this expression along with the tank ac resistances and small-signal transformations, the small-signal impedances are obtained as

$$Z_{sss} = s \cdot 2L_s + R_s + Z_{lss} = R_{ts} \frac{G_s}{1 + sC_o R_{load}} \ , \tag{5.10}$$

$$Z_{pss} = s \cdot 2L_p + R_p + \frac{{\omega_s}^2 M^2}{Z_{sss}} = R_{tp} \frac{G_p}{G_s} \ , \tag{5.11}$$

where R_{ts} is the total ac resistance of the secondary tank, R_{tp} is the total ac resistance of the primary tank, G_s is the secondary tank small-signal impedance characteristic polynomial and G_p is the primary tank small-signal impedance characteristic polynomial, which are given by

$$R_{ts} = R_e \left(1 + \frac{R_s}{R_e}\right) \ , \tag{5.12}$$

$$R_{tp} = R_r \left(\frac{1 + R_p \frac{R_s + R_e}{{\omega_s}^2 M^2}}{1 + \frac{R_s}{R_e}}\right) \ , \tag{5.13}$$

$$G_s = \left(1 + s \cdot K_{ss1} + s^2 \cdot K_{ss2}\right) \ , \tag{5.14}$$

$$G_p = \left(1 + s \cdot K_{pp1} + s^2 \cdot K_{pp2} + s^3 \cdot K_{pp3}\right) \ , \tag{5.15}$$

where K_{ss1}, K_{ss2}, K_{pp1}, K_{pp2} and K_{pp3} are the polynomial coefficients representing effects of the circuit parameters on the model, given by

$$K_{ss1} = \frac{2L_s + C_o R_s R_{load}}{R_{ts}} \ , \tag{5.16}$$

$$K_{ss2} = \frac{2L_s C_o R_{load}}{R_{ts}} \ , \tag{5.17}$$

$$K_{pp1} = \frac{2L_s R_p + C_o R_p R_s R_{load}}{R_{tp} R_{ts}} \ , \tag{5.18}$$

$$K_{pp2} = \frac{4L_p L_s + 2L_p C_o R_s R_{load} + 2L_s C_o R_p R_{load}}{R_{tp} R_{ts}} \ , \tag{5.19}$$

$$K_{pp3} = \frac{4L_p L_s C_o R_{load}}{R_{tp} R_{ts}} \ . \tag{5.20}$$

5.3.2 Derivation of primary tank expressions with constant voltage input

As shown in Fig. 5.4, the system is first considered as a voltage input system, with $\hat{v}_{in}$ being the input into the inverter [61]. For the transformerless topology, from (5.1) $\vec{v}_{AB}$ can be written as

$$\vec{v}_{AB} = V_{in} \vec{s}_p = \frac{2\sqrt{2}}{\pi} V_{in} \sin\left(\frac{\varphi_{AB}}{2}\right). \tag{5.21}$$

Taking partial derivative of both side of (5.21) with respect to v_{in} and φ_{AB}, the small-signal variation in the primary tank input voltage ($\hat{\vec{v}}_{AB}$) is obtained in terms of $\hat{v}_{in}$ and

$\hat{\varphi}_{AB}$ as

$$\hat{\vec{v}}_{AB} = \frac{2\sqrt{2}}{\pi} \sin\left(\frac{\varphi_{AB}}{2}\right) \hat{v}_{in} + \frac{\sqrt{2}}{\pi} V_{in} \cos\left(\frac{\varphi_{AB}}{2}\right) \hat{\varphi}_{AB} \ . \tag{5.22}$$

Then, from the primary tank small-signal impedance expression in (5.11) the primary tank current phasor is obtained as

$$\hat{\vec{i}}_p = \frac{\hat{\vec{v}}_{AB}}{Z_{pss}} = \frac{2\sqrt{2}}{\pi R_{tp}} \frac{G_s}{G_p} \sin\left(\frac{\varphi_{AB}}{2}\right) \hat{v}_{in} + \frac{\sqrt{2} V_{in}}{\pi R_{tp}} \frac{G_s}{G_p} \cos\left(\frac{\varphi_{AB}}{2}\right) \hat{\varphi}_{AB} \ . \tag{5.23}$$

Now, focusing on the current transformation owing to the inverter, the relation is obtained from the phasor transformation in (5.1) as

$$i_i = \mathrm{Re}[\vec{i}_p \cdot \vec{s}_p] = \frac{2\sqrt{2}}{\pi} \vec{i}_p \sin\left(\frac{\varphi_{AB}}{2}\right) \ . \tag{5.24}$$

Taking partial derivative of (5.24) in terms of $\vec{i}_p$ and $\hat{\varphi}_{AB}$, the small-signal variation in inverter input current ($\hat{i}_i$) is obtained in terms of $\hat{\vec{i}}_p$ and $\hat{\varphi}_{AB}$ as

$$\hat{i}_i = \frac{2\sqrt{2}}{\pi} \sin\left(\frac{\varphi_{AB}}{2}\right) \hat{\vec{i}}_p + \frac{\sqrt{2}}{\pi} I_p \cos\left(\frac{\varphi_{AB}}{2}\right) \hat{\varphi}_{AB} \ . \tag{5.25}$$

5.3.3 Considerations for the input side of the model

On the other hand, from the dc input side of the small-signal model shown in Fig. 5.5, considering the small-signal current through the input capacitor C_{in} ($\hat{i}_{cin}$), the relation between $\hat{i}_{in}$ and $\hat{v}_{in}$ is found as

$$\hat{i}_i = \hat{i}_{in} - \hat{i}_{cin} = \hat{i}_{in} - sC_{in}\hat{v}_{in} \ . \tag{5.26}$$

Plugging in the steady-state value of I_p from Chapter 3 and the expression of $\hat{i}_i$ from (5.26) in (5.25), the expression of $\hat{i}_i$ modifies to

$$\begin{aligned}\hat{i}_i &= \hat{i}_{in} - sC_{in}\hat{v}_{in} \\ &= \frac{2\sqrt{2}}{\pi}\sin\left(\frac{\varphi_{AB}}{2}\right)\hat{\vec{i}}_p + \frac{\sqrt{2}}{\pi}\frac{\pi I_{in}}{2\sqrt{2}\sin\left(\frac{\varphi_{AB}}{2}\right)}\cos\left(\frac{\varphi_{AB}}{2}\right)\hat{\varphi}_{AB} \ .\end{aligned} \tag{5.27}$$

Simplification of (5.27) and grouping of terms give the expression of $\hat{v}_{in}$ in terms of $\hat{i}_{in}$ and $\hat{\varphi}_{AB}$ as

$$\hat{v}_{in} = \frac{V_{in}}{I_{in}}\frac{G_p}{G_{iin}}\hat{i}_{in} - \frac{V_{in}}{2\tan\left(\frac{\varphi_{AB}}{2}\right)}\frac{G_{\varphi AB}}{G_{iin}}\hat{\varphi}_{AB} \ , \tag{5.28}$$

where the polynomials G_{iin} and $G_{\varphi AB}$ are given by

$$\begin{aligned}G_{iin} &= sC_{in}\frac{V_{in}}{I_{in}}G_p + G_s \\ &= 1 + \left(K_{ss1} + C_{in}\frac{V_{in}}{I_{in}}\right)s + \left(K_{ss2} + K_{pp1}C_{in}\frac{V_{in}}{I_{in}}\right)s^2 + K_{pp2}C_{in}\frac{V_{in}}{I_{in}}s^3 + K_{pp3}C_{in}\frac{V_{in}}{I_{in}}s^4 \ ,\end{aligned} \tag{5.29}$$

$$G_{\varphi AB} = G_p + G_s \ . \tag{5.30}$$

5.3.4 Development of primary current transfer function

Using the above derivations, the small-signal change in primary current ($\hat{\vec{i}}_p$) can be found in terms of the small-signal variations in the independent variables $\hat{i}_{in}$ and $\hat{\varphi}_{AB}$, which can be used to find the primary current transfer function. Since $\hat{\varphi}_{AB}$ is considered as the control input, the disturbance input $\hat{i}_{in}$ is set to zero to find the desired transfer functions.

Then, substitution of (5.28) in (5.23) gives

$$\hat{\vec{i}}_p = \frac{2\sqrt{2}}{\pi R_{tp}} \frac{G_s}{G_p} \sin\left(\frac{\varphi_{AB}}{2}\right) \left(-\frac{V_{in}}{2\tan\left(\frac{\varphi_{AB}}{2}\right)} \frac{G_{\varphi AB}}{G_{iin}} \hat{\varphi}_{AB} \right) + \frac{\sqrt{2} V_{in}}{\pi R_{tp}} \frac{G_s}{G_p} \cos\left(\frac{\varphi_{AB}}{2}\right) \hat{\varphi}_{AB} \ , \tag{5.31}$$

simplification of which by using the steady-state analysis results from Chapter 3 and the expression of Z_{pss} from (5.11), $\hat{\vec{i}}_p$ is obtained in terms of $\hat{\varphi}_{AB}$ as

$$\hat{\vec{i}}_p = -\frac{\pi I_{in}}{2\sqrt{2}\sin\left(\frac{\varphi_{AB}}{2}\right)\tan\left(\frac{\varphi_{AB}}{2}\right)} \frac{G_s(G_{\varphi AB} - G_{iin})}{G_{iin} G_p} \hat{\varphi}_{AB} \ , \tag{5.32}$$

which gives the primary current transfer function ($\hat{\varphi}_{AB}$ to $\hat{\vec{i}}_p$) as

$$G_{i\varphi} = \frac{\hat{\vec{i}}_p}{\hat{\varphi}_{AB}} = -\frac{\pi I_{in}}{2\sqrt{2}\sin\left(\frac{\varphi_{AB}}{2}\right)\tan\left(\frac{\varphi_{AB}}{2}\right)} \frac{G_s(G_{\varphi AB} - G_{iin})}{G_{iin} G_p} \ . \tag{5.33}$$

Further, plugging in the polynomials $G_{\varphi AB}$ and G_{iin}, the transfer function takes the form

$$G_{i\varphi} = -\frac{\pi I_{in}}{2\sqrt{2}\sin\left(\frac{\varphi_{AB}}{2}\right)\tan\left(\frac{\varphi_{AB}}{2}\right)} \frac{G_s(1 - sC_{in}\frac{V_{in}}{I_{in}})}{G_{iin}} \ . \tag{5.34}$$

5.3.5 Derivations of the secondary tank expressions

For the small-signal expressions of the secondary tank, the mutual inductance effect is considered to obtain $\hat{\vec{v}}_{oc}$ as shown in (5.8). Then, the small-signal rectifier input voltage is found from the secondary resonant compensation tank, with the input as $\hat{\vec{v}}_{oc}$, the secondary tank impedance from (5.10) and reflected load impedance from (5.9) as

$$\hat{\vec{v}}_{DE} = \hat{\vec{v}}_{oc}\frac{Z_{lss}}{Z_{sss}} = j\frac{\omega_s M \hat{\vec{i}}_p}{G_s\left(1+\frac{R_s}{R_e}\right)} \ . \tag{5.35}$$

5.3.6 Development of output voltage transfer functions

Now, the small-signal output voltage is obtained by using the voltage transformation of the rectifier, which is same as the relation in steady-state developed in Chapter 3. Then the small-signal variation in output voltage $\hat{v}_{out}$ is obtained in terms of $\hat{\vec{i}}_p$ as

$$\hat{v}_{out} = \frac{\hat{\vec{v}}_{DE}}{\vec{s}_s} = j\frac{\pi}{2\sqrt{2}}\frac{\omega_s M \hat{\vec{i}}_p}{G_s\left(1+\frac{R_s}{R_e}\right)} \ . \tag{5.36}$$

Then the transfer function of primary current to output voltage ($\hat{\vec{i}}_p$ to $\hat{v}_{out}$) is obtained as

$$G_{vi} = \frac{\hat{v}_{out}}{\hat{\vec{i}}_p} = j\frac{\pi\omega_s M}{2\sqrt{2}\left(1+\frac{R_s}{R_e}\right)}\frac{1}{G_s} \ . \tag{5.37}$$

Product of (5.34) and (5.37) and its manipulation gives the control-to-output transfer function ($\hat{\varphi}_{AB}$ to $\hat{v}_{out}$) as

$$G_{v\varphi} = \frac{\hat{v}_{out}}{\hat{\vec{\varphi}}_{AB}} = -j\frac{\pi^2\omega_s M I_{in}}{16\sin\left(\frac{\varphi_{AB}}{2}\right)\tan\left(\frac{\varphi_{AB}}{2}\right)\left(1+\frac{R_s}{R_e}\right)}\frac{1-sC_{in}\frac{V_{in}}{I_{in}}}{G_{iin}} \ . \tag{5.38}$$

5.3.7 Transfer functions for the transformer based topology

Considering the current boost transformer turns ratio of m and the corresponding inverter phasor transformation ratio as shown in (5.2), the primary current and output voltage transfer functions for the transformer based constant dc current input underwater SS IPT are obtained as

$$G_{i\varphi,tr} = \frac{\hat{\vec{i}}_p}{\hat{\varphi}_{AB}} = -\frac{m\pi I_{in}}{2\sqrt{2}\sin\left(\frac{\varphi_{AB}}{2}\right)\tan\left(\frac{\varphi_{AB}}{2}\right)} \frac{G_s(1 - sC_{in}\frac{V_{in}}{I_{in}})}{G_{iin}} \ . \tag{5.39}$$

$$G_{v\varphi,tr} = \frac{\hat{\vec{v}}_{out}}{\hat{\vec{\varphi}}_{AB}} = -j\frac{m\pi^2\omega_s M I_{in}}{16\sin\left(\frac{\varphi_{AB}}{2}\right)\tan\left(\frac{\varphi_{AB}}{2}\right)\left(1 + \frac{R_s}{R_e}\right)} \frac{1 - sC_{in}\frac{V_{in}}{I_{in}}}{G_{iin}} \ . \tag{5.40}$$

5.4 Discussions About the Small-Signal Model and Transfer Functions

A few key properties of the system and how they depend on the system parameters are observed from the developed small-signal model. Also, a suitable control loop structure can be formed based on the characteristics of these transsfer functions. These are discussed here.

5.4.1 DC gain and low frequency characteristics

The obtained transfer functions $G_{i\varphi}$, $G_{v\varphi}$, $G_{i\varphi,tr}$ and $G_{v\varphi,tr}$ demonstrate the negative dc gain characteristics, which are commensurate with the dc constant current input systems with phase shift control [61]. This negative dc gain provides a phase shift of -180° in dc and low-frequency region. However, there is a phase lead in $G_{i\varphi}$ and $G_{i\varphi,tr}$ caused by the mutual inductance action, which makes the secondary voltage lead the primary voltage by 90°. The combined effect gives a low-frequency phase of -90° in the low frequency region.

5.4.2 Pole and zero locations

The characteristic polynomials of all the transfer functions is G_{iin}, whose expression in (5.29) demonstrates a fourth order polynomial. Hence the small-signal model behaves as a fourth order system. By plugging in system parameters in (5.29), the pole and zero locations can be found for dynamic characterization of the system.

Also, all the transfer functions have a right half plane (RHP) zero at the frequency of

$$\omega_{zrh} = \frac{I_{in}}{C_{in} V_{in}} \ , \tag{5.41}$$

which demonstrates that the input capacitor sets the location of the RHP zero, and the constant current input configuration causes this zero. Hence if the RHP causes control loop issues, the input capacitor value can be adjusted to control its effects without sufficiently hampering any of the resonant tank operations.

Further, the secondary tank impedance polynomial G_s constitutes of the additional pair of conjugate left-half plane zeros in the primary tank current transfer function. This shows that in dynamics the secondary side adds dynamics to the primary tank current, which is not visible in the output voltage. The locations of these complex conjugate zeros in the primary current transfer functions can be found by plugging the necessary system parameters in (5.14).

5.4.3 Potential control scheme

A potential control loop structure applicable for such constant dc current input IPT systems is shown in Fig. 5.6. This is similar in structure for dc current input underwater series resonant converters [61]. The negative gain is compensated by subtracting the controller output from 180°.

Further, in this topology the controls are on the primary side, whether the controlled

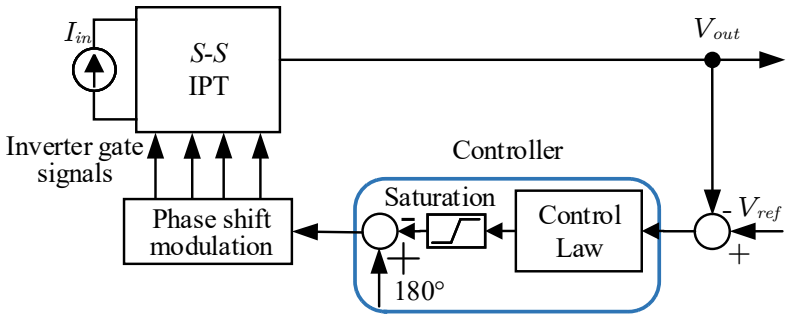

Fig. 5.6: Potential control loop block diagram for constant dc current input underwater SS IPT system.

variable is on the secondary side. Hence a good communication is required to implement the above control loop. The implementation of the control loop is outside the scope of this work, as the model developed here can be easily used to design controllers as per requirement.

5.4.4 Effect of mistuning of resonant tanks

The model is developed for a nominal design with fully aligned coils and assuming the tanks operate at resonance and unity power factor, so that tank currents can be approximated by fundamental harmonic approximation. The couplings, coil inductances and their equivalent ac resistances in seawater are directly obtainable from finite element simulations and experimental measurements. However, mistunings can make the small-signal model assumptions inaccurate, as the second order approximations are applicable at a narrow zone around the resonant operation [67]. However as it is shown in Chapter 4, the system is designed in such a way, so that the mistunings are kept within a very narrow band around the resonant frequency even at the worst case misaligned operations. Hence the model is accurately applicable for all operating conditions of the system.

With the steady-state designs and small-signal models of the constant dc current input IPT topologies presented so far, the next chapter presents the simulation and experimental results for both the steady-state designs and the small-signal models.

CHAPTER 6

Experimental Results for the Underwater IPT Designs

The steady-state analysis, design considerations and small-signal modelings presented for the different underwater IPT topologies used in this dissertation were validated through simulations and experimental results. The simulated plots for different design aspects and associated system design parameters are provided in detail in Chapter 4. These parameters were closely replicated in experimental setups, whose details and results obtained from them are presented here.

For the constant dc voltage input IPT topology, the results are demonstrated through comparison of eddy loss resistances from analysis, simulation and experimental measurements and power tests at 940 W output to obtain a loss distribution model. For the transformer based constant dc current input topology, the steady-state experimental results are provided in the range 34 W to 300 W to demonstrate the output characteristics. The small-signal model for this is also validated through comparison with simulations and dynamic plot of primary current. For the 1 kW prototype with transformerless constant dc current IPT network, the steady-state experimental results are presented for 300 W to 1000 W to demonstrate the output characteristics under different alignment conditions. Further, the frequency response and pole-zero locations of the small-signal model of this topology are presented, which can be in future validated through experiments.

6.1 Setup and Experimental for Constant DC Voltage Input Topology and Optimization Validations

6.1.1 Setup Description

The experimental setup for these set of experiments are shown in Fig. 6.1, which used the parameters provided in Table 4.1. The full-bridge inverter was built in the primary

printed circuit board (PCB), whereas the secondary board housed the full-bridge diode rectifier and the secondary compensation capacitors. Owing to the higher voltage requirements of the primary compensation capacitors, off-board capacitor modules were used. The controller board was used to generate the gate pulses for the inverter switches. The coils were wound with heat-shrink tube wrapped litz wires to keep the seawater from seeping into them. Then they were put in a setup with gap of 8 mm and immersed in a saline water tank. The saline water tank was prepared with 3.7 kg of table salt dissolved in 100 L of water, having conductivity of 5 S/m at room temperature of 20 °C to emulate typical seawater conditions [120].

Due to the limited availability of the primary capacitor modules, both the tanks were tuned at 255 kHz, with the 8-turn primary coil and the 5-turn secondary coil. The setup works as a current source on the output as per the analysis in Chapter 3, and hence a constant voltage load of up to 48 V was used on output for different power conditions. The experiments were performed both with the coils in air and dipped in the saline water tank. Owing to the power limitations of the bench-top supply, experiments were performed up to 940 W, which corresponds to a constant current output of 19.6 A.

6.1.2 Validation of Seawater Eddy Loss Model with Experiments

At first, the ac resistance measurements of the coils were performed using a HIOKI IM3536 LCR meter having an accuracy of ±10 % with proper calibration. Measurements were performed with the coils kept in air and also with the coils kept in saline water tank. If the measurements in air and underwater are denoted as $R_{ac,air}$ and $R_{ac,sea}$ respectively, then the eddy loss resistance is obtained as [72]

$$R_{eddy} = R_{ac,sea} - R_{ac,air} \ . \tag{6.1}$$

The measurements were performed for both the 8-turn primary coil and the 5-turn secondary coil in the frequency range of 100 kHz to 500 kHz used in the optimizations in

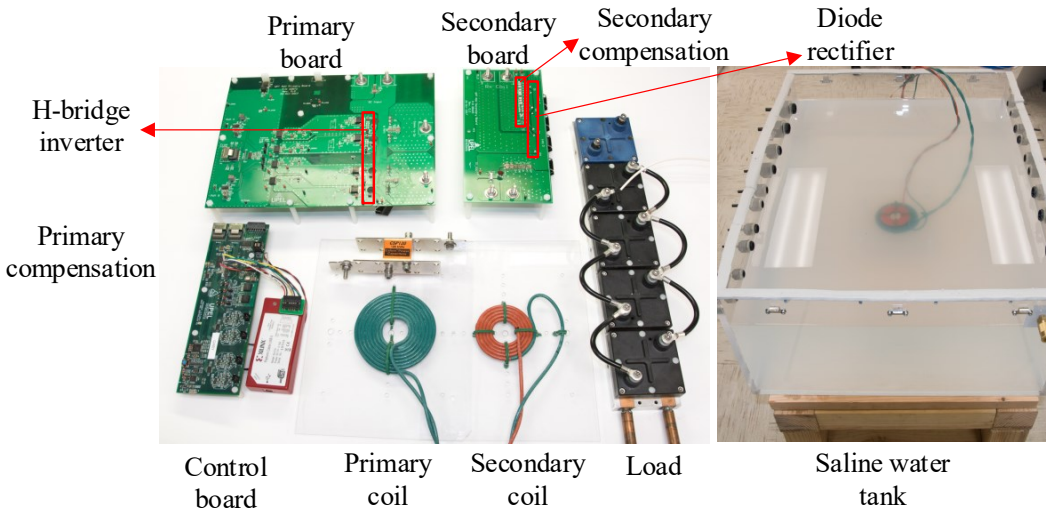

Fig. 6.1: Experimental setup for the constant dc voltage input underwater IPT system.

Chapter 4. The measured eddy loss resistance values were compared with the ones calculated from the derived expressions in Chapter 2. In addition, the system with an infinite seawater surrounding the coils were simulated using finite element method (FEM) in Ansys Maxwell (the model was similar to the pictorial view shown in Fig. 4.7, but the cores were not used as air core coils were considered for these set of experiments). The FEM simulation results were also compared with the calculated and measured eddy loss resistance values. The corresponding comparison plots are shown in Fig. 6.2.

Notably the analytical model was found to correctly estimate the eddy loss trend vs

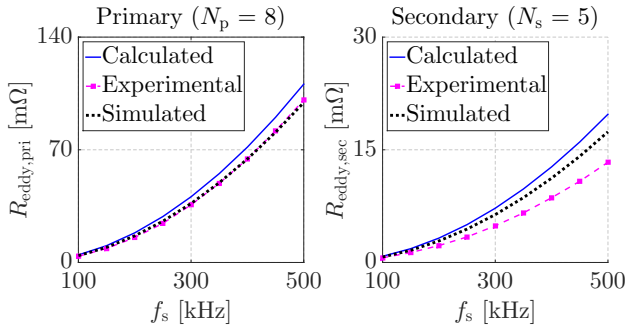

Fig. 6.2: Plots of calculated, experimental and simulated values of eddy loss resistance for primary coil with $N_p = 8$ ($R_{eddy,pri}$) and secondary coil with $N_s = 5$ ($R_{eddy,sec}$), for operating frequency (f_s) in the range 100 kHz to 500 kHz.

frequency with the percentage error being consistently within 15 % over the whole frequency range, which is acceptable for usage in analytical optimization. The estimation error can be attributed to the approximations associated with the integrals in Chapter 2 and also the simplifications in form of the approximate elliptical integrals, whereas the lumped copper forms used in FEM simulations do not contribute to the estimation errors. The errors were also more prominent for the secondary coils with lower resistance, as the LCR reading accuracy gets affected at such low resistance measurements.

6.1.3 Experimental Results and Loss Distribution Model

The voltage and current waveforms for the underwater operation at output power of 940 W are shown in Fig. 6.3(a) and Fig. 6.3(b). Both the figures show the primary tank current (i_p) and secondary tank current (i_s) waveforms. Along with them, Fig. 6.3(a) shows the inverter output voltage (v_{AB}) and rectifier input voltage (v_{DE}) waveforms and Fig. 6.3(b) shows the waveforms of primary coil voltage (v_p) and secondary coil voltage (v_s). Similar waveforms were obtained with operation in air, which is why they are not shown.

From the dc readings of the input and output quantities, an underwater efficiency of 83 % was obtained from this setup. Hence the loss distribution analysis was performed to find losses among different parts of the setup. In addition to conduction losses in the inverter and diode rectifier, the inverter had partial hard switching losses as it was not possible to

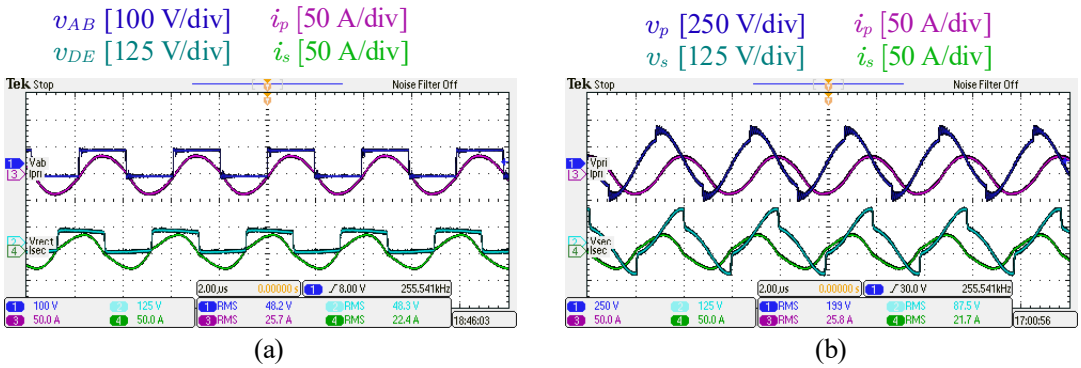

Fig. 6.3: Experimental waveforms for underwater operation at output power of 940 W with $f_s = 255$ kHz (a) v_{AB}, v_{DE}, i_p, i_s waveforms, (b) v_p, v_s, i_p, i_s waveforms.

operate at the exact resonant frequency due to component tolerances. Moreover the ac resistance of the compensation capacitors and the underwater resistance of the coils were measured using the LCR meter for this purpose. The waveform data of the tank voltages and currents were captured from the scope to used them for the loss distribution analysis. The resulting loss distribution for in air and underwater operation are shown in Table 6.1. The loss distribution is also pictorially demonstrated in Fig. 6.4.

From the loss distribution, the magnetic coupling efficiency for in-air and underwater operation can be obtained as

$$\eta_{mag} = \frac{P_{in} - P_{loss,inv} - P_{loss,cp} - P_{loss,p} - P_{loss,s}}{P_{in} - P_{loss,inv} - P_{loss,cp}} \ , \tag{6.2}$$

where P_{in} is the input power calculated from the input dc readings. For the above-mentioned experiments, using (6.2), the magnetic coupling efficiencies in air and underwater operation were found as 98.2 % and 96.4 % respectively, which was commensurate with the optimized design presented in Chapter 4. The target dc to dc efficiency of the design was 90 %, but owing to the high losses in ESR of the capacitors (includes connection wires), diode rectifier voltage drop and partially hard-switched inverter, the dc input to dc output efficiencies for in-air and underwater operation were obtained as 85 % and 83 % respectively. However, the loss distribution table and graph demonstrate that the degradation in efficiency in

Table 6.1: Distribution of losses in different stages of the system for in air and underwater experiments at 940 W output power with seawater losses included as part of the coil losses.

Loss component [in W]	**In air**	**Underwater**
Inverter losses ($P_{loss,inv}$)	40.1	41.4
Primary capacitor losses ($P_{loss,cp}$)	38.3	38.9
Primary coil losses ($P_{loss,p}$)	12.7	28.9
Secondary coil losses ($P_{loss,s}$)	6.5	10.1
Secondary capacitor losses ($P_{loss,cs}$)	34.7	34.1
Rectifier losses ($P_{loss,rec}$)	35.6	35.5

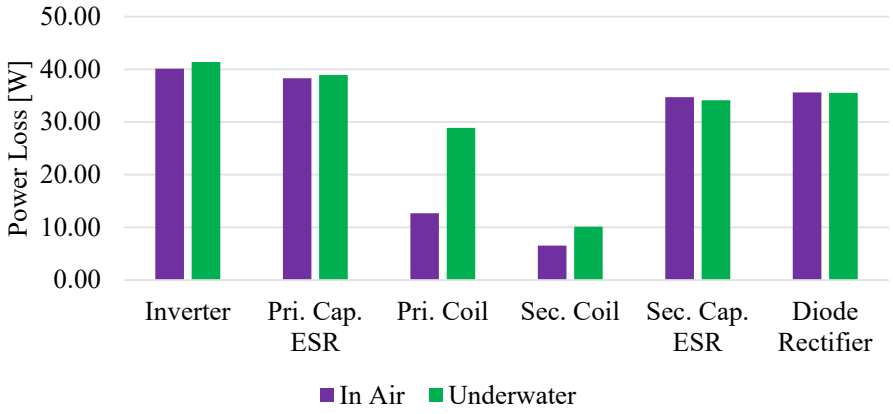

Fig. 6.4: Loss distribution chart for the system with in air and underwater operations.

underwater operation occurred predominantly in the seawater eddy currents, manifested in the higher coil losses. Hence the experimental results were found to validate the seawater eddy loss model of the circular coils presented in Chapter 2 and the subsequent optimized designs presented therein and later with specific numbers and simulation plots in Chapter 4.

6.2 Experimental Setup and Results for Transformer-based 330 W Prototype

6.2.1 Setup Details

As explained in Chapter 4, for this set of experiments the coils from the voltage source IPT design were used, but with ferrite backplates and with a gap of 18 mm. The coil inductance values were as shown in Table 4.2. The transformer with the parameters as in Table 4.2 was also fabricated, and the primary compensation capacitor modules and the PCB mount capacitors for secondary compensation were modified to obtain the values as in Table 4.2. The experimental setup is shown in Fig. 6.5 with different sections marked. The experiments were carried out in the output power range of 34 W to 330 W, to fully validate the operation in DCM for lower output powers and the operation at the maximum power point of the setup. A constant dc current input of 1 A and switching frequency of 250 kHz were used, with the tanks tuned to the switching frequency. The same saline water tank was used to emulate the seawater environment, as also shown in Fig. 6.5.

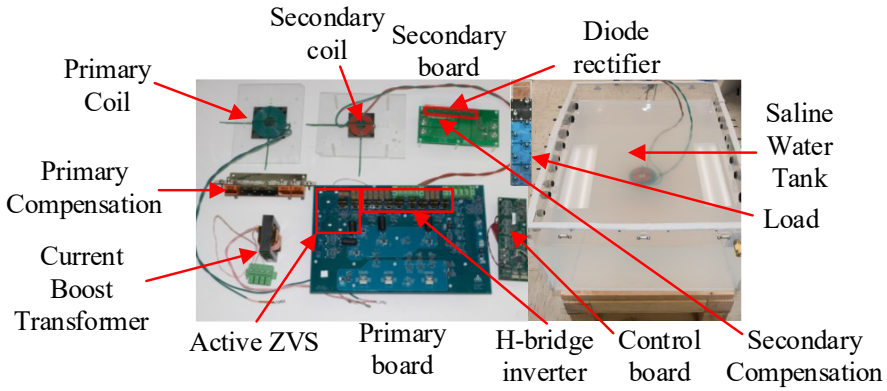

Fig. 6.5: Experimental setup for the transformer based constant dc current input underwater IPT system.

6.2.2 Experimental Results and Discussions - Steady-state Operation

The waveforms of the ac quantities inverter output voltage (v_{AB}), rectifier input voltage (v_{DE}), primary tank current (i_p) and secondary tank current (i_s) while maintaining a fixed phase angle of $\varphi_{AB} = 120°$ are shown in Fig. 6.6(a) and Fig. 6.6(b) for $P_{out} = 34\,\text{W}$ and $P_{out} = 330\,\text{W}$ cases respectively. The waveform of i_s in Fig. 6.6(a) demonstrates the DCM operation of the rectifier at $P_{out} = 34\,\text{W}$. The change in input voltage from P_{out} of 34 W to 330 W is observable from the amplitude of the waveforms of v_{AB}, whereas the relatively constant output voltage of 16 V is visible from the amplitude of the rectifier input voltage v_{DE}.The rms current readings of i_p shows that the primary current remains fairly constant during the whole power range whereas the secondary current (i_s) amplitude varies with load.

The waveforms of the same tank quantities while regulating V_{out} to 16 V by changing φ_{AB} are shown in Fig. 6.6(a) and Fig. 6.6(b) for $P_{out} = 34\,\text{W}$ and $P_{out} = 330\,\text{W}$ cases respectively. It can be seen the output voltage regulation in the wide power range is possible with minimal change in the inverter phase angle. This also demonstrates that the system has constant output voltage characteristics with control through φ_{AB}.

The waveforms of i_p and i_s in both figures also show that i_s has higher distortions at lower P_{out}, whereas at higher P_{out}, i_p has higher distortion. This is commensurate with the analysis that the tank quality factors vary reciprocally with Q_{sl} being high at higher load

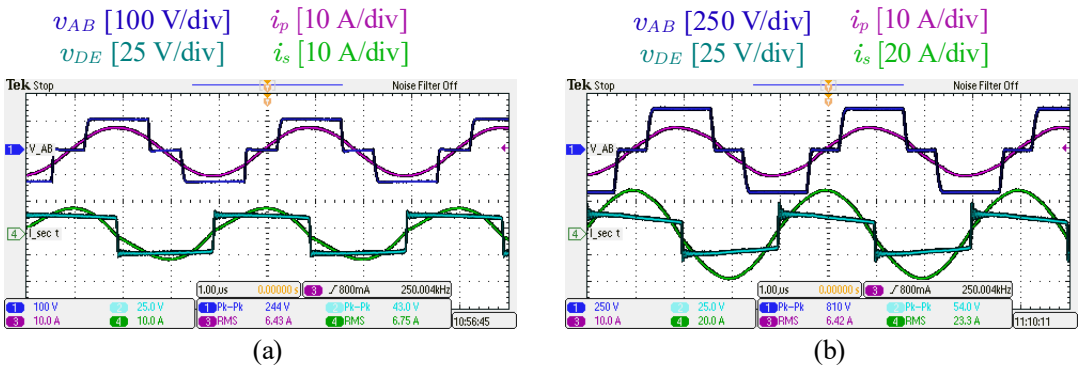

Fig. 6.6: Experimental waveforms of v_{AB}, v_{DE}, i_p and i_s for a fixed $\varphi_{AB} = 120°$ (a) at P_{out} = 34 W, (b) at P_{out} = 330 W.

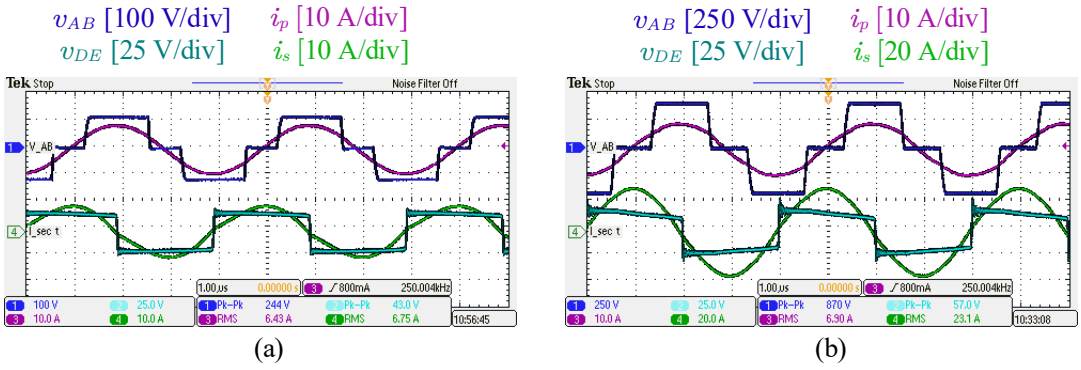

Fig. 6.7: Experimental waveforms of v_{AB}, v_{DE}, i_p and i_s for while regulating V_{out} = 16 V (a) at P_{out} = 34 W, (b) at P_{out} = 330 W.

while Q_{pl} becoming low at higher loads.

To further demonstrate the output voltage characteristics, the variation of V_{out} is plotted over the full power range with a fixed phase angle of $\varphi_{AB} = 120°$, which is shown in Fig. 6.8(a). It shows that V_{out} changes only by 11 % over the considered power range, with higher voltages obtained at light loads due to DCM. The plot of φ_{AB} with P_{out} to keep constant V_{out} of 16 V is also shown in Fig. 6.8(b), which shows that a 15° variation is sufficient to keep the output voltage at the desired value. Higher φ_{AB} is required to keep output at a desired voltage at lighter loads as V_{out} goes higher due to DCM. Thus the experimental results successfully validate the steady-state analysis and the basic design considerations used for the transformer-based topology design in Chapter 3 and Chapter 4.

At the operating point of P_{out} = 330 W with V_{out} = 16 V, the total system loss from

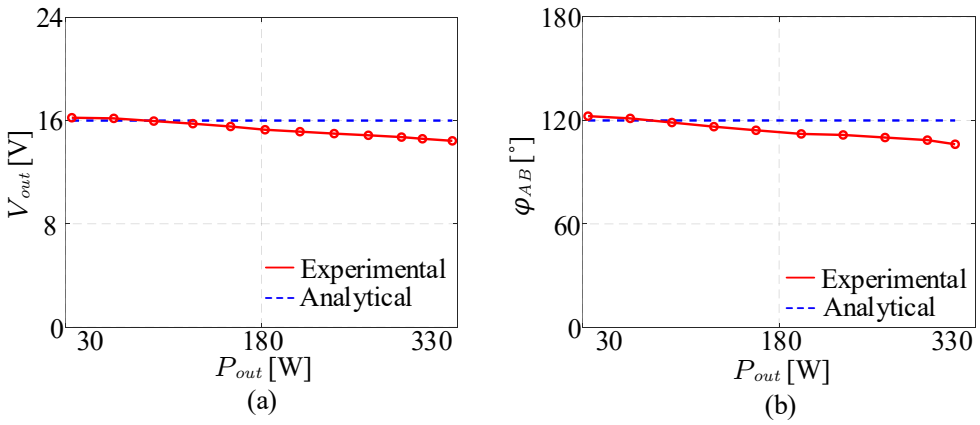

Fig. 6.8: Analytical and experimental plots of V_{out} and φ_{AB} over P_{out} in the range 34 W to 330 W (a) V_{out} vs P_{out} for fixed $\varphi_{AB} = 120°$, (b) φ_{AB} vs P_{out} while regulating $V_{out} = 16$ V.

dc input to dc output was found to be approximately 93 W, which corresponds to a power transfer efficiency of 75 %. Over the full power range, the peak efficiency was around 83 % achieved at around $P_{out} = 150$ W. The low efficiencies can be attributed to a number of factors such as usage of a diode rectifier with high current output, terminal strips connecting the off-board primary capacitor modules, the HV transformer losses in the high-volume core and the usage of non-optimized coils. Especially regarding the coils, the quality factor plots in Fig. 4.3 show that appreciably large quality factors were used for this setup, which can be carefully minimized to minimize the copper volume to improve coupler efficiency. The ferrite plates were also non-optimized as ferrite bars available in the lab were used for this proof of concept experiments. All these factors were carefully considered in the design and experiments of the 1 kW system, whose results are presented later in this chapter.

6.2.3 Validation of Small-signal Model

The small-signal model and associated transfer functions developed for this topology in Chapter 5 are also validated through simulations and experiments. The output voltage transfer function ($G_{v\varphi}$) frequency response is validated through comparison with the response obtained with MATLAB/PLECS based switching model simulation results with "multitone" analysis tool. The comparison is shown in Fig. 6.9. The plots demonstrate

good match between the responses predicted by the analytical and the simulation model, which validates the presented small-signal model.

Next, the model was verified through the comparison of the dynamic response of the primary current transfer function ($G_{i\varphi}$) through experimental results using the hardware setup shown in Fig. 6.5. The experimental results were obtained under the application of a step change in φ_{AB} of $+6^\circ$ over an initial value of 114°. The nominal operating point with 100 W output power was chosen so that both the resonant tanks operate with near sinusoidal currents, as per the quality factor analysis in Chapter 4. The experimental waveforms obtained using single-trigger mode of the oscilloscope are shown in Fig. 6.10(a), which shows the variation of the primary coil current waveforms under the application of φ_{AB} step change. It also shows the input current (I_{in}) revealing that it is kept constant throughout the φ_{AB} step change and the subsequent dynamics interval. The waveform data is captured and the primary coil current data is plotted superimposed with its analytically predicted envelope, which are shown in Fig. 6.10. Since we are interested in comparing the envelope of the experimental waveform and the analytical one, the figure shows the waveform zoomed near the peak. From Fig. 6.10(b), a good match between the small-signal model predicted envelope and the experimental i_p waveform is observed during the transients following the step change in φ_{AB}.

The above results validate the small-signal model to predict the dynamics of the system.

6.3 Experimental Results for Transformerless Constant DC Current Input 1 kW Prototype

6.3.1 Experimental Setup

The experimental setup is shown in Fig. 6.11, where the different parts are marked. This setup was built with the parameters in Table 4.3. Due to large number of turns in the primary coil, this setup could not be built with heat-shrink tubed litz wires. Among different options to keep the coils away from water, using epoxy potting on the coils and putting the coils in an underwater box setup were considered. While the first option lets

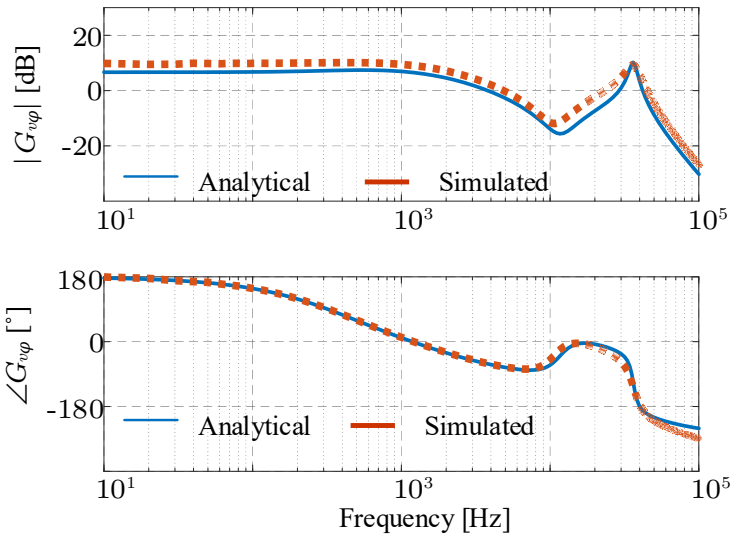

Fig. 6.9: Comparison of bode plots of $G_{v\varphi}$ obtained from small-signal model and MATLAB/PLECS switching model simulation.

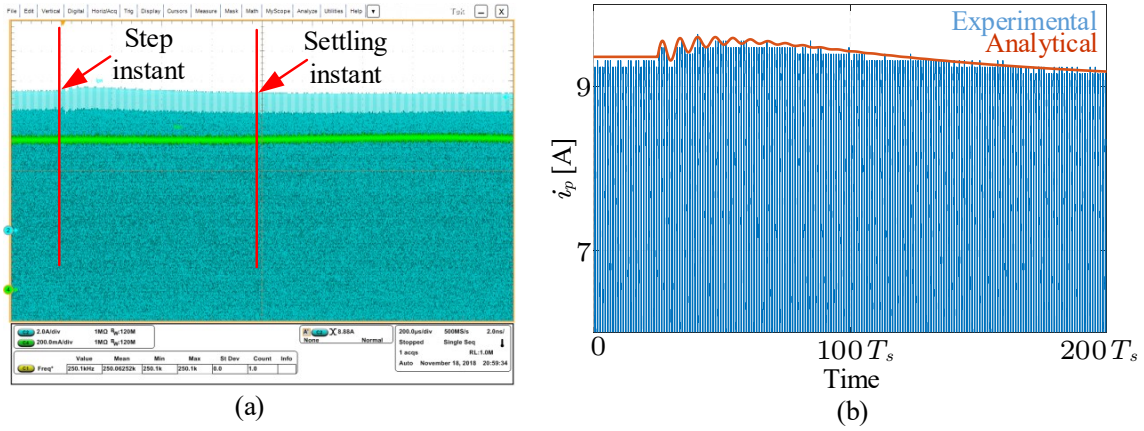

Fig. 6.10: Experimental results for dynamics of i_p on application of step change in φ_{AB} of $+6°$ over an initial value of $114°$: (a) oscilloscope capture, (b) experimental waveform superimposed upon the envelope predicted by the small-signal model. Experimental waveform of primary coil current superimposed upon the envelope predicted by the small-signal model.

the coils to be fully immersed in seawater, the second one presents an arrangement closer to an actual AUV wireless charging system. In a typical AUV wireless charging, the primary coil is housed in a hermetically sealed charging station, with the coils placed on the wall inside the station facing the seawater. The AUV docks into the charging wall or comes closer to the station, aligns with the help of communications and then gets power, with the secondary coils and electronics mounted within the AUV. Hence the coils never see infinite seawater around them, while the power transfer still happens through the seawater gap [32]. In the underwater box arrangement, the coils were enclosed in two plastic boxes to emulate the docking station and AUV housing, with the saline water gap between them adjusted to achieve a total coil to coil nominal gap of 1 in. The arrangement is shown in Fig. 6.11.

Circuit boards with pluggable connectors was used for the compensaiton capacitors such that multiple parallel capacitors can be used to reduce effects of ESR. The primary board was made with high-voltage clearances for the H-bridge and optimizing the layout to reduce switching loop effects and ESR between the switches and the pluggable connectors. On the secondary board, the surface mount MOSFETs were used along with pluggable gate drivers to optimize the high-current path impedance. Both primary and secondary boards were also designed with plugged in FPGA based control boards for gate signal generations and other sensor data processing. AC and dc current sensors were placed for the secondary tank current and dc output current respectively. The tank current sensor output is passed through a comparator to generate pulses for synchronous rectification, which is taken to the FPGA. Output voltage sensor was also kept for small-signal model data capturing and future control designs.

6.3.2 Experimental Results for Steady-state Operations

Experiments were performed both in air and in the saline water tank, and under all the gap and alignment settings considered in the designs in Chapter 4. Operations by keeping φ_{AB} constant and also by varying φ_{AB} to keep V_{out} at 75 V, in the output power range of 300 W to 1000 W were verified. This load range was used as below 300 W full pulse width synchronous rectification was not possible owing to current transformer magnetization

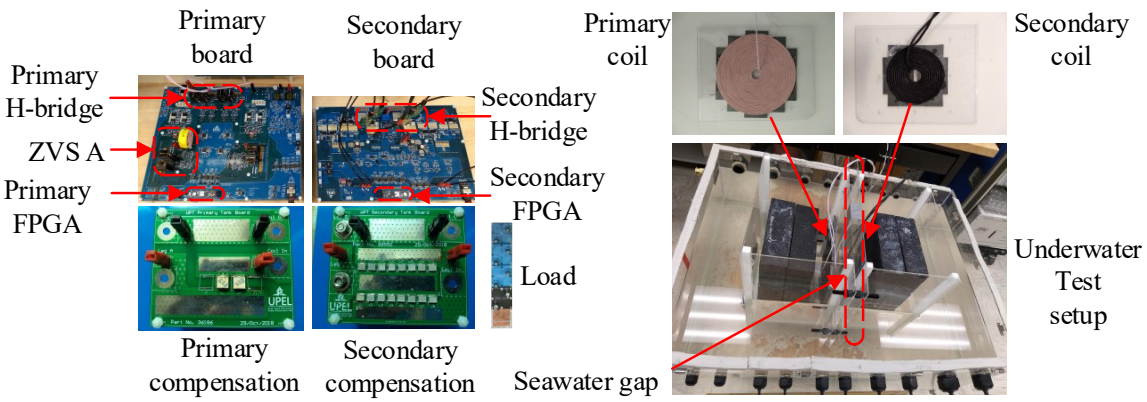

Fig. 6.11: Experimental setup for the transformerless constant dc current input underwater IPT system.

inductance effects in the synchronous rectification circuit.

The underwater experiment waveforms of the tank quantities such as primary H-bridge output voltage (v_{AB}), primary current (i_p), secondary H-bridge input voltage (v_{DE}) and secondary current (i_s) with a fixed phase angle of $\varphi_{AB} = 106.2°$ are shown in Fig. 6.12 for the nominal position of 1 in coil-to-coil gap and full alignment. The waveforms at 300 W operating point is shown in Fig. 6.12(a) whereas in Fig. 6.12(b) the waveforms are shown for 1 kW operating point keeping. It can be seen that even though amplitude of v_{AB}, and i_s got changed with change in load, the amplitude of v_{DE} remains relatively constant with small deviation. This shows that input voltage V_{in} is load dependent whereas output voltage V_{out} is relatively more independent on load.

Again, experiments were performed with φ_{AB} adjusted to regulate V_{out} to 75 V at all points. The waveforms for these tests at 300 W and 1 kW are shown in Fig. 6.13. This too shows that with small adjustment in φ_{AB}, V_{out} is successfully regulated at the desired value over the wide load range of 300 W to 1000 W. All these waveforms demonstrate the constant voltage output characteristics similar to the ones obtained with the transformer based topology earlier.

Experiments were also performed with the considered misaligned positions, so that the maximum coupling and minimum coupling as mentioned in Table 4.3 are obtained. For maximum coupling position a reduction in gap of 10 % of nominal with full alignment is

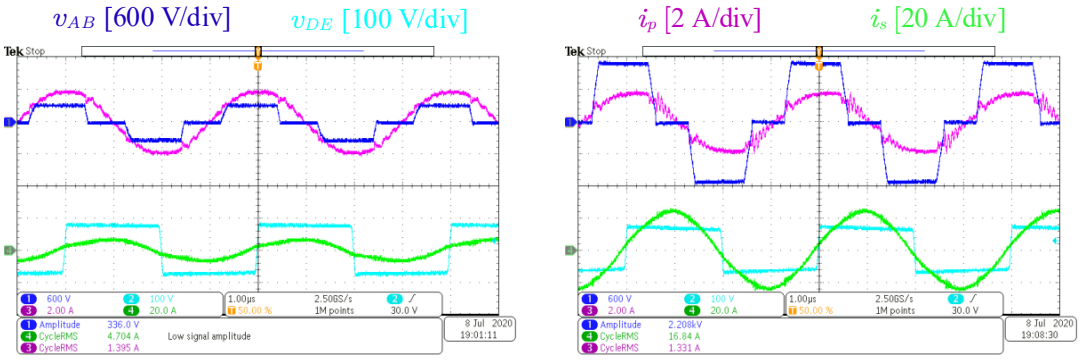

Fig. 6.12: Experimental waveforms of v_{AB}, v_{DE}, i_p and i_s for underwater operation with nominal gap, full alignment and a fixed $\varphi_{AB} = 106.2°$ - (a) at $P_{out} = 300\,\text{W}$, (b) at $P_{out} = 1\,\text{kW}$.

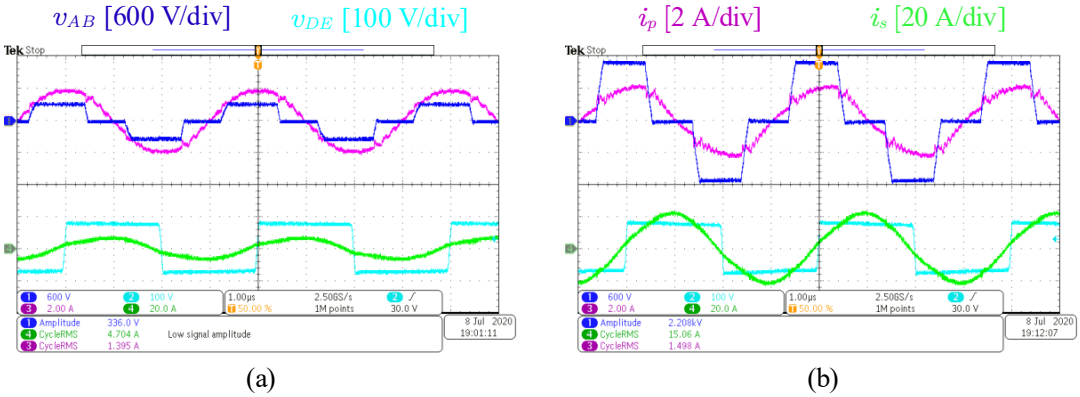

Fig. 6.13: Experimental waveforms of v_{AB}, v_{DE}, i_p and i_s for underwater operation with nominal gap, full alignment and V_{out} regulated to 75 V - (a) at $P_{out} = 300\,\text{W}$, (b) at $P_{out} = 1\,\text{kW}$.

considered, while for minimum coupling position, an increase in gap of 10 % of nominal with X-direction misalignment of 10 % of the primary coil outside radius is considered. The same set of experimental waveforms are shown in Fig. 6.14. The system demonstrates similar operating characteristics even under these mistuned cases, with φ_{AB} sufficiently lower than the maximum of 180° for the maximum coupling position and the maximum rms value of i_p being less than 1.9 A, which is acceptable for the chosen wire gauge.

To further validate the load-independent nature of the output voltage, the plot of V_{out} vs P_{out} with a fixed phase angle of $\varphi_{AB} = 106.2°$ is shown in Fig. 6.15(a) for nominal coupling conditions. It shows that in the load range of 30 % to full load, the drop in V_{out} is approximately 11 %, which is acceptable for demonstrating a load independent output characteristics. It is also validated from the plot of φ_{AB} vs P_{out} for nominal coupling conditions in Fig. 6.15(b), which shows that a change of 11° in φ_{AB} is needed to regulate V_{out} to 75 V over the considered load range, with an initial angle of $\varphi_{AB} = 106.2°$. Both plots are also compared with the analytical values in these figures, which show good correlation between analytical and experimental results. However, these variations are slightly higher in percentage than the results shown with the transformer based topology, as slightly lower tank quality factors are used with higher couplings.

In addition, the plots of φ_{AB} vs P_{out} with the maximum and minimum coupling positions are shown in Fig. 6.15(b) to validate the control range of φ_{AB} for maintaining V_{out} to 75 V over the considered load range. While larger variations in φ_{AB} are expected at these settings owing to the mistuning of the tanks, the plots demonstrate appreciable performance in terms of variation range of φ_{AB}. The maximum φ_{AB} needed to regulate V_{out} at the strongest coupling and lowest power point of 300 W was 122°, and the minimum φ_{AB} needed to regulate V_{out} at the weakest coupling and maximum power point of 1 kW was 75°. Both these values are within the desired range of controlling φ_{AB} needed to regulate V_{out} with the considered misalignments.

As the coils for this system were designed with careful consideration between the coil size and quality factor required for constant voltage characteristics, the efficiency plots are

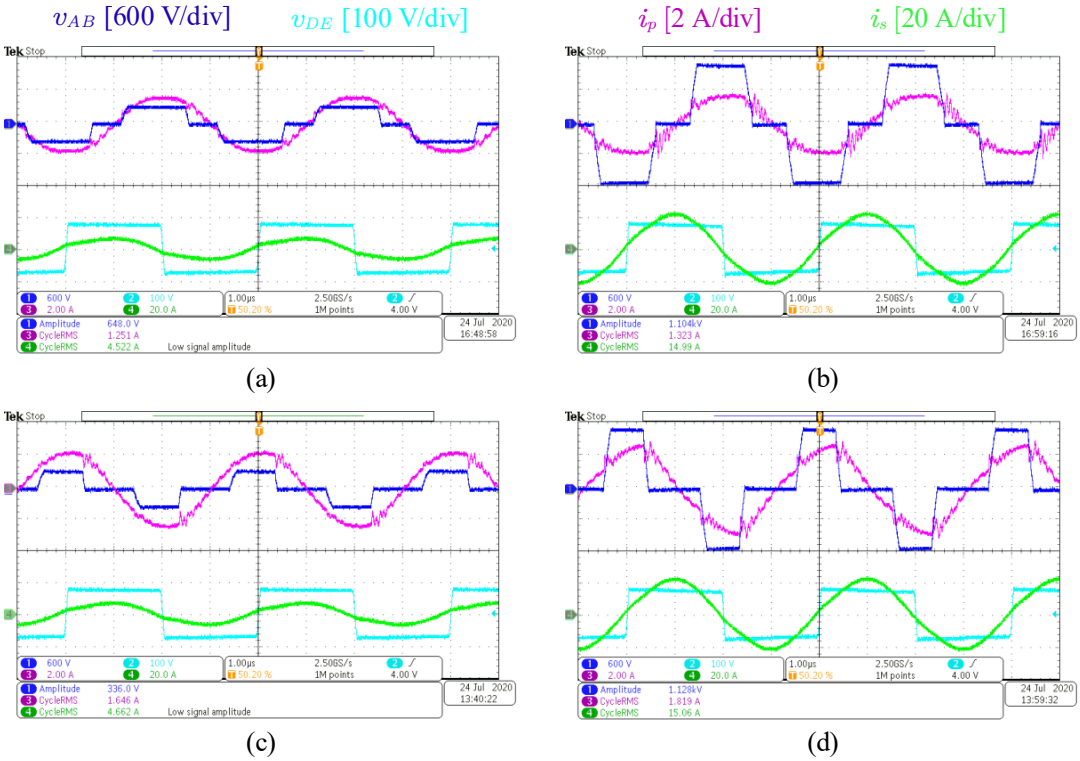

Fig. 6.14: Experimental waveforms of v_{AB}, v_{DE}, i_p and i_s for underwater operation with maximum and minimum coupling positions, while regulating V_{out} to 75 V - (a) at P_{out} = 300 W with maximum k, (b) at P_{out} = 1 kW with maximum k, (c) at P_{out} = 300 W with minimum k, (d) at P_{out} = 1 kW with minimum k.

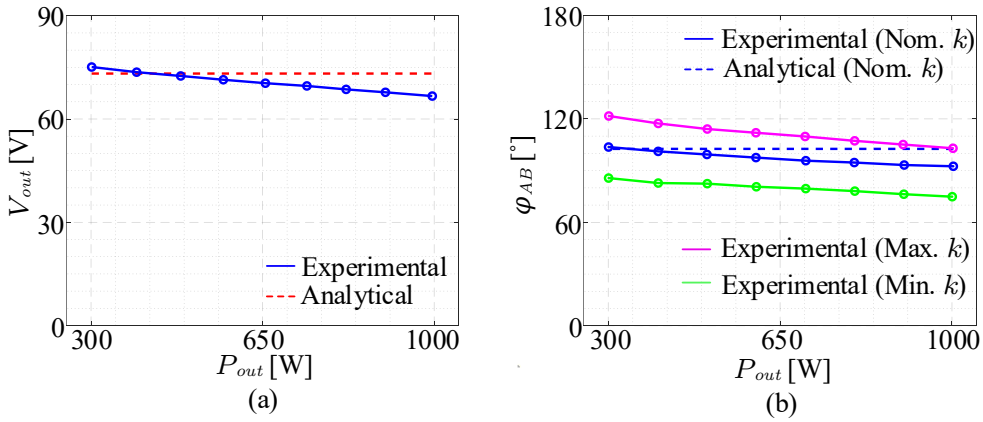

Fig. 6.15: Plots of V_{out} and φ_{AB} for underwater experiments over the load range of 300 W to 1000 W - (a) V_{out} vs P_{out} with $\varphi_{AB} = 106.2°$ under nominal coupling conditions, (b) φ_{AB} vs P_{out} to regulate V_{out} = 75 V, at nominal, maximum and minimum coupling conditions.

observed. The plots of underwater operation efficiencies are obtained with varying load power for the different coupling positions, which are shown in Fig. 6.16. It can be seen that appreciable underwater power transfer efficiency at 1 kW of 90.5 % is obtained with peak efficiency of 91.5 % under the nominal conditions. The efficiencies were found to drop for operations with the minimum coupling position due to larger primary tank currents. However the plots demonstrate that all the positions achieve more than 90 % underwater power transfer efficiency in the considered wide load range.

In addition to the above experiments, step changes of ±100 W were applied to the load around a steady-state load of 700 W and the variation in I_{out}, V_{in} and V_{out} were captured. These waveforms are shown together in Fig. 6.17. It can be seen with both load steps, negligible change is observed in the steady-state V_{out}, further corroborating the constant output voltage characteristics of the system.

These results are achieved with the secondary coil radius being 55 mm, such that it can fit into small AUVs as per the target of the application. Hence the results presented successfully validate the steady-state analysis and design considerations of the system in Chapter 3 and Chapter 4.

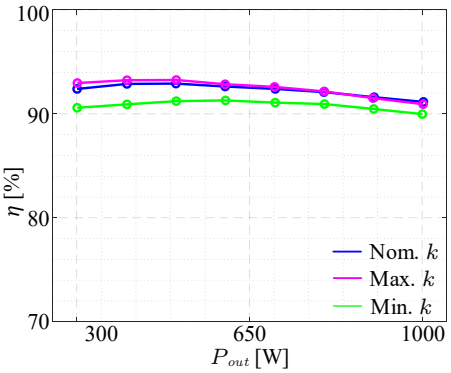

Fig. 6.16: Plots of Efficiency vs P_{out} while regulating $V_{out} = 75$ V, at nominal, maximum and minimum coupling conditions.

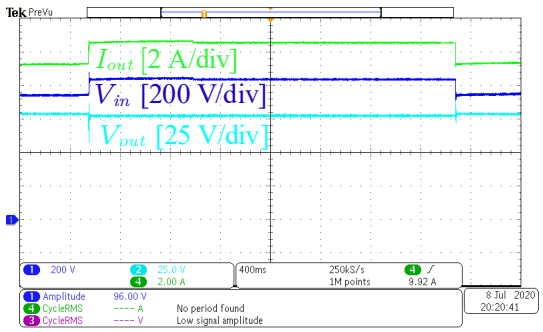

Fig. 6.17: Experimental waveforms of I_{out}, V_{in} and V_{out} with a load step change from 700 W to 800 W and back.

6.3.3 Small-signal Model Plots for this Topology

Using the parameter values in Table 4.3 in the small-signal model developed in Chapter 5, the frequency response and pole-zero locations of the output voltage transfer function ($G_{v\varphi}$) are obtained. The frequency response plot is shown in Fig. 6.18.

From the pole-sero location analysis of $G_{v\varphi}$, the right half plane (RHP) zero is found to be located at 113 Hz, whereas the low-frequency complex poles were located at 222 Hz. This is expected as the RHP zero is only caused by the input capacitor which is typically chosen large for such applications. Also, the pair of conjugate poles and the RHP zero result in a dynamic response with multiple gain crossover frequency. Hence controls should be carefully exercised to sufficiently attenuate frequency components near the resonant peak, occurring around 56 kHz. In future these can be validated in experiments.

This chapter concludes the design and experimental validations performed concerning the IPT system development for AUV applications in underwater current distribution. The next chapter shifts the focus to the review of topologies in EV DWPT for their control analysis purposes.

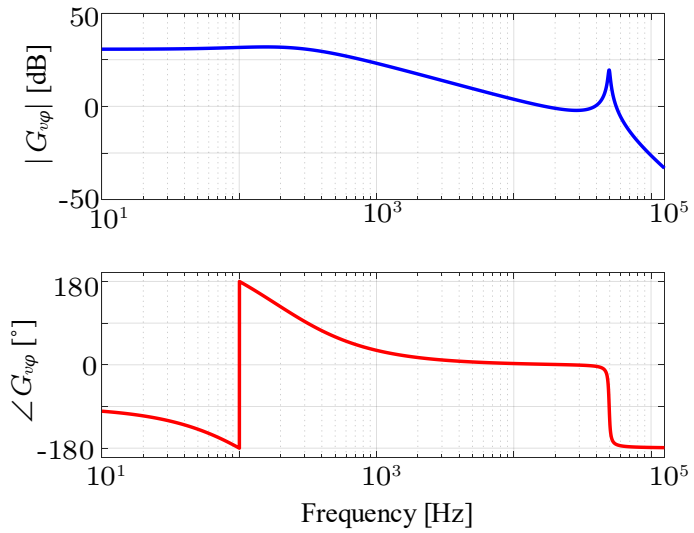

Fig. 6.18: Frequency response plot of $G_{v\varphi}$ for the transformerless constant dc current input SS IPT topology obtained from its small-signal model.

CHAPTER 7

Analysis of Topologies and Control Implementations for EV DWPT Controls

The other emerging application area of wireless power transfer (WPT) this dissertation has looked into is analysis of controls in electric vehicle dynamic wireless power transfer (EV DWPT). The literature review presented for this part of the dissertation in Chapter 1 highlighted the numerous coupler, converter, compensation topologies and control methods being developed for EV DWPT. It was also identified that the reliability of controls in the face of fast varying coupling and interoperability considerations among different configurations form a relevant research problem in EV DWPT. This chapter presents a critical analysis of the existing coupler, converter, compensation topologies and control methods to highlight how they contribute towards power flow controls in an EV DWPT system. Then the analytical power expressions for different compensation topologies and the analytical expressions between different control inputs and the IPT tank quantities they regulate are presented. These expressions are later utilized in Chapter 8 to perform control performance comparisons.

7.1 Magnetic Couplers and Their Contributions to DWPT Controls

7.1.1 Analysis of Coupler Configurations

The main purposes of the different EV DWPT coupler formations, shown in Chapter 1, are to generate different shapes of magnetic flux along the roadway. A critical analysis of the couplers bring out that three different types of flux patterns are produced, namely Double-sided waterfall type, Single-sided N-S flux across the road type and Single-sided N-S flux along the road type. A pictorial view of these patterns on the road are shown in Fig. 7.1, using the DWPT test-track at Utah State University [127], and the details of the rail and pad type couplers helping to achieve these patterns are put in Table 7.1.

The double-sided waterfall type couplers typically couple to circular/rectangular shaped secondary coils. On the other hand, the single sided N-S across road flux patterns typically couples to DD secondary coils with similarly oriented poles. It can be seen that the single-sided flux configurations allow for directional coupling features, often resulting in benefits such as eliminating accidental coupling with unnecessary pads. An advantage with these coils is that these primary coils can be wound as an elongated primary coil to minimize variations in coupling and reduce the amount of power electronics that is required. On the other hand, the single-sided flux with N-S along road configuration can couple to both circular/rectangular coils as well as DD coil topologies which is beneficial from an interoperability point of view. These are also recommended for compatibility with stationary WPT standards. However, since the north and south poles alternate as the vehicle drives along the road, any single-coil topology will eventually have a null-spot in the coupling factor profile. The null points cause large power pulsations so this is typically addressed by using multi-coil secondary pad topologies to ensure that at least one secondary coil is coupled at all times. However this leads to a doubling up of some power electronics and additional weight on the vehicle [16].

The rail-type structures typically energize all coils in the system through one inverter, leading to higher leakage flux and conduction losses. The multiple-pad structures improve on this, but they require segmentation controls to turn on the proper coils as per vehicle position. Synchronization between the inverters are also necessary. To improve over the transition zone low coupling with the DD type primaries, crossed and overlapped pad couplers are proposed [87, 92]. However, their practical application may be limited due to

Fig. 7.1: Flux patterns generated by couplers along the road (a) Double-sided waterfall type, (b) Single-sided N-S across the road type, (c) Single-sided N-S along the road type.

Table 7.1: Flux patterns and characteristics obtained from typical magnetic couplers in DWPT.

Flux pattern	**Couplers**	**Characteristics**
Waterfall	• Rails: E-type [11], W-type [80], π-type [15] • Pads: Circular [88], Rectangular [18], Cylindrical [28]	• Double-sided flux • Lower coupling • Higher leakage field • Good continuity of flux along the roadway
N-S poles across road	• Rails: U-type [10] • Pads: DD [21], Bipolar [94] (when directed perpendicular to road)	• Single-sided flux • Higher coupling • Higher leakage field on roadside • Continuous flux tunnel along the roadway
Alternate N-S poles along road	• Rails: I-type [14], S-type [12], n-type [16] • Pads: DD [21], Bipolar [94] (when directed along the road)	• Single-sided flux • Higher coupling • Lower leakage field • Alternate poles along roadway, with zero coupling zones in between

control and implementation complexity.

7.1.2 Effects of Couplers on DWPT Controls

The magnetic couplers define the coupling profile along the roadway. The coupling tends to be fairly constant when the primary and secondary pads are mostly aligned, whereas after a certain amount of misalignment the coupling falls off exponentially. Other important factors that need to be considered with the coil design are the rate of change of coupling as well as the spacing between neighbouring primary pads to determine how much the coupling factors profiles overlap. If one of the objectives is to maintain constant power to the vehicle then the rate of change of coupling and the overlapping between the coupling profiles dictate the control bandwidth requirements. A typical DWPT system coupling profile and how the rate of change of coupling dictates the control bandwidth requirements are shown in Chapter 8.

7.2 Converter Topologies in EV DWPT and Their Roles in Controls

7.2.1 Analysis of the EV DWPT Converter Topologies

A typical grid-to-vehicle EV DWPT system involve four stages of conversion, was shown in Fig. 1.12, including front-end converters and high-frequency inverters on the primary side and rectifiers and back-end dc-dc converters on the secondary side. The overview of different converter topologies used in these stages were presented in Chapter 1. The control handles of these stages were marked in Fig. 1.12, which are used here to analyze roles of the converter stages in EV DWPT controls.

The front-end stage consisting of power factor correction (PFC) and DC-DC stages can employ DC-DC converter duty ratio (D_i) controls to control the input to the EV DWPT system. The inverter is controlled through the duty ratio of the inverter switches (D_{inv}) or the phase shift between the legs (ϕ_{inv}). The rectifiers in EV DWPT typically employ diode rectifier which do not provide any control options. However secondary DC-DC converters can employ their duty ratio (D_o) controls for implementing secondary side controls.

Using a buck converter at the frond-end is beneficial for lower voltage inverter designs. The secondary side converters are chosen based on the current or voltage driven nature of the rectifier. Hence buck converters are most suitable with secondary side series or *LCCL* compensations, whereas boost converters are suitable with secondary parallel compensations. Buck-boost converters with suitable designs can be used with both configurations [1].

7.2.2 Role of Converters in EV DWPT Controls

The above-mentioned control handles of the different stages are the main contributions of the converters in EV DWPT controls. In EV DWPT systems without front-end or back-end converters, power flow controls can be only exercised in the inverter and/or rectifier stages. Among them inverter phase shift control is typically used, while passive rectifiers have been the preferred configuration for rectifiers. The major drawback of inverter controls is the variation of soft-switching conditions, which are essential to maintian high efficiency and reduction of EMI. Having the controls shifted to front or back end converters help in ensuring soft-switching in the DWPT stage, at the cost of additional stages in the system. However the primary side converters are required to have the capability to control turning on or off the proper coils as per vehicle position, and having a secondary side converter help in charging with high-speed vehicles, as is shown in the discussions in Chapter 8.

Typically multiple single phase schemes with communications are employed for segmentation controls. While multi-phase inverters or single inverter driving multiple pads can ease the segmentation control procedure, they come with the drawback of complicated hardware.

7.3 Analysis of Compensations and Their Roles in Controls for DWPT

7.3.1 Different Compensation Characteristics in DWPT

From the overview of different compensation topologies of EV DWPT presented in Chapter 1, the important topologies can be classified into a few major categories, as shown in Fig. 7.2. These include second order *LC* topologies such as SS [76], SP [88] and PP [23] and

higher order categories such as $LCCL$-S [3], $LCCL$-P [25], $LCCL$-$LCCL$ [4] and Series Hybrid (SH) [21]. Among the non-conventional higher order topologies, the CCC-T topology [77] functions as an SS compensation, the LSP-S topology [93] functions as an $LCCL$-S compensation and the LCC-LCC topology [28] works similar to a SP compensation. Hence these topologies are considered as part of these categories in the analysis. The LCC-LCC topology with multiple primaries in parallel and another series compensation based topology with the leakage inductance compensations of the primary help in detection of the most coupled coils [28, 84]. However the leakage inductance compensation may not be ideal as it varies with change in coupling. The characteristics of the re-configurable compensation networks also fall within these categories, while the mode switching action provides different operating modes to them. The series hybrid topology is shown to work better for DWPT applications compared to parallel hybrid [21, 30], and subsequently only the series hybrid topology is considered for comparisons in this dissertation.

In general the higher order compensations provide better control over the primary current which is typically regulated to be constant in EV DWPT controls. However they increase compensation complexity. The hybrid compensation topologies help in combining the advantages of the LC and higher-order compensations. However they are not typically interoperable with other topologies.

7.3.2 Role of Compensation Networks in DWPT Controls

In addition to the advantages of reactive power compensation and soft-switching, the compensation networks modify the relation between coupling, power flow and the control efforts such as inverter phase shift angle and dc-dc converter duty ratios. The compensation topologies which help in smoothing out the power flow profile with higher ripple in mutual inductance profile are the best suited for EV DWPT applications, as they help designing the system with simpler magnetic configurations.

7.4 Analysis of Control Objectives, Implementations and Communications in DWPT Controls

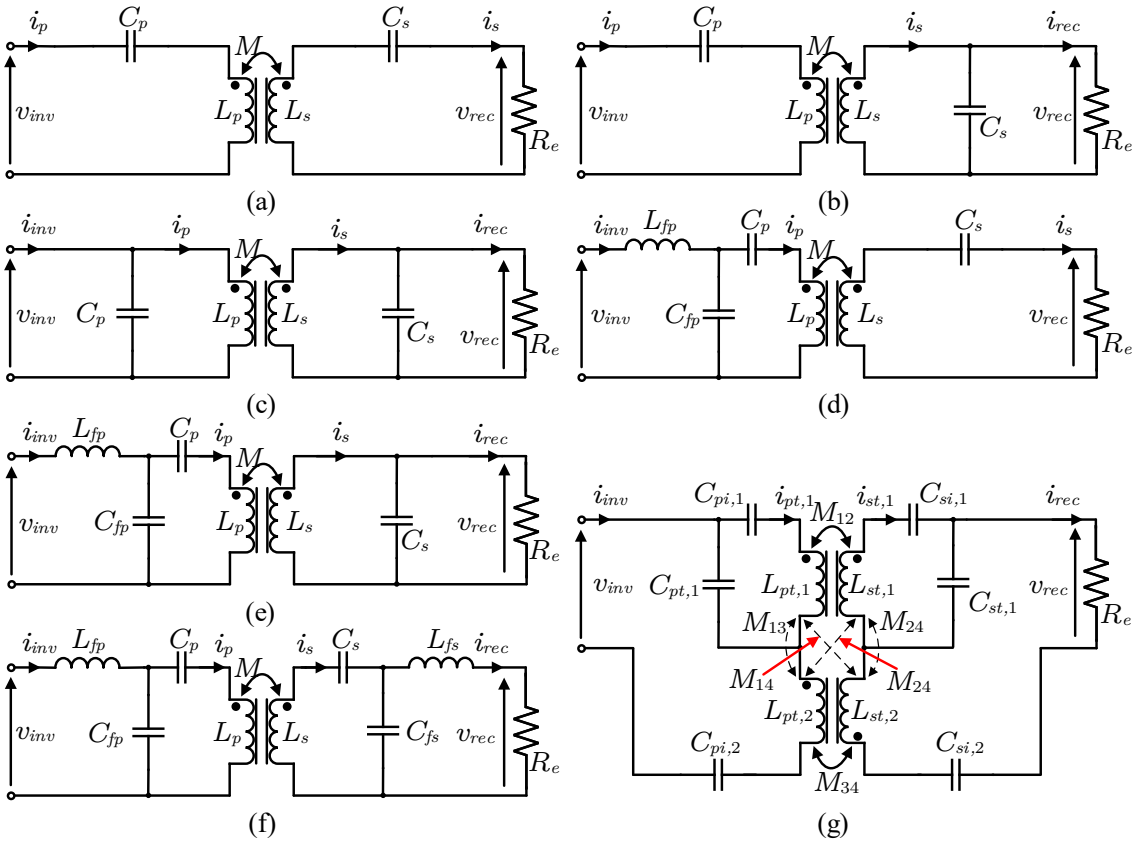

Fig. 7.2: Different compensation characteristics relevant in DWPT (a) Series-Series (SS), (b) Series-Parallel (SP), (c) Parallel-Parallel (PP), (d) *LCCL*-Series (*LCCL*-S), (e) *LCCL*-Parallel (*LCCL*-P), (f) *LCCL-LCCL*, (g) Series Hybrid (SH).

7.4.1 Analysis of Control Objectives, Implementations and Communications in DWPT

The overview of control objectives and implementation schemes in Chapter 1 demonstrate that power flow control to keep a steady, desired power flow with a moving vehicle is the most important control objective in a DWPT system, while the other ones are supporting objectives. While the open-loop configurations result in full independence from control loop designs and communications, the closed-loop systems are more practical. Typical open-loop controlled EV DWPT systems use larger or complicated pad formations [4,87,92], complicated compensation topologies [21, 28, 84] or re-configurable architecture through mode-switching [94, 103]. These lead to mostly difficult or sometime impractical solutions. Hence closed-loop controls are recommended for easier and more interoperable system designs and better stability.

Among the closed loop methods, the primary side and dual side controls typically need communication between primary and secondary sides, while that is not required for secondary side controlled systems. On the other hand, keeping all the controls on the secondary side leads to higher workload on the vehicle side power electronics, which is typically difficult.

7.4.2 Roles of Different Control Implementation Schemes and Communications in DWPT Controls

The effectiveness of the different control implementation schemes are decided by the control handles used, which are determined by the used converters in the system. In general secondary side controls are preferable as dependency on communications can be avoided. For primary and dual side controls, the delay in communications can affect control bandwidth, which need to be carefully considered.

7.5 Areas to Look for Analysis of Effectiveness of DWPT Controls

The above sections bring out that choice of compensation topologies, control handles and analysis of effect of communications are the main areas to look for to analyze effective-

ness of DWPT controls. Proper combination of compensation topology and control handle can lead to flat power flow profile with negligible change in control effort and high resolution control of desired power flow, even with considerable variations in coupling. This leads to the most interoperable DWPT systems. Also the control bandwidth should be sufficient to overcome effect of communication delays, which can cause stability issues while charging high-speed vehicles.

Hence analytical expressions pertaining to different compensation topologies and control handles are noted together in the next section, which are then used in Chapter 8 to compare control performances and communication effects.

7.6 Analytical Expressions for Usage in Control Comparisons

7.6.1 Expressions Pertaining to Different Compensation Topologies

For the comparison of control performances of different topologies, their steady-state expressions of secondary quality factor (Q_{sl}), reflected impedance (Z_r) and primary current (I_p) are used. The $LCCL$ networks in these topologies are analyzed as generalized T-type network, as shown in Fig. 7.3. The expressions for the characteristic topologies SS, SP, PP, $LCCL$-S, $LCCL$-P and $LCCL$-$LCCL$ topologies are shown in Table 7.2. In the expressions, V_{inv} and I_{inv} denote the inverter output voltage and current as shown in Fig. 7.2, Z_{op} denotes the characteristic impedance of the primary tank as explained in Chapter 3 and F_p denotes the ratio between operating frequency and the resonant frequency in series compensated primary as explained in Chapter 3. The T-model parameters α and β of the higher order compensations can be expressed from [2] as

$$\alpha = {\omega_s}^2 L_{fp} C_{fp}, \tag{7.1}$$

$$\beta = {\omega_s}^2 L_p C_{fp} - \frac{C_{fp}}{C_p}. \tag{7.2}$$

The hybrid topologies are derived as series or parallel combinations of $LCCL$ and S

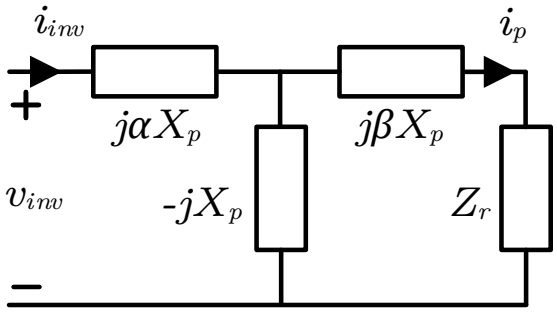

Fig. 7.3: Generalized diagram of T-type compensations.

topologies on each side. They have different currents flowing through each D coil in their DD structure. The different current and power expressions are available from the works by L. Zhao *et al.* [21, 30] as

$$P_{out,sh} = \frac{{V_{inv}}^2 R_e}{\omega^2 \left(\frac{L_{pt,2(LCL)} L_{st,2(LCL)}}{M_{12}} + M_{34}\right)^2}, \tag{7.3}$$

$$m = \sqrt{\frac{L_{pt,2(LCL)}}{L_{pt,1} L_{pt,2}} \frac{L_{st,2(LCL)}}{L_{st,1} L_{st,2}}}, \tag{7.4}$$

7.6.2 Expressions Pertaining to Different Converters and Their Control Handles

The controls are achieved through the control inputs regulating primary or secondary tank quantities. The primary side control inputs regulate the inverter output voltage fed into the primary tank (V_{inv}). The secondary side control inputs regulate the secondary tank quality factors. Voltage and current-fed inverters and capacitive and LC filters on the secondary side also modify these relationships. Considering these, the relations are tabulated in Table 7.3.

Table 7.2: Analytical expressions for the considered compensation topologies.

Topology	Q_{sl}	Zr	$\lvert Ip \rvert$
SS	$\frac{\omega_s L_s}{R_e}$	$\frac{k^2 {\omega_s}^2 L_p L_s}{R_e}$	$\frac{V_{inv}}{F_p Z_{op}\sqrt{{Q_{sl}}^2+\left(1-\frac{1}{{F_p}^2}\right)^2}}$
SP	$\frac{R_e}{\omega_s L_s}$	$\underbrace{k^2 {\omega_s}^2 L_p C_s R_e}_{\Re(Z_r)} - j\underbrace{k^2 \omega_s L_p}_{\Im(Z_r)}$	$\frac{V_{inv}}{F_p Z_{op}\sqrt{k^4 {Q_{sl}}^2+\left(1-\frac{1}{{F_p}^2}-k^2\right)^2}}$
PP	$\frac{R_e}{\omega_s L_s}$	$\underbrace{k^2 {\omega_s}^2 L_p C_s R_e}_{\Re(Z_r)} - j\underbrace{k^2 \omega_s L_p}_{\Im(Z_r)}$	$\frac{V_{inv}}{F_p Z_{op}\sqrt{k^4 {Q_{sl}}^2+(1-k^2)^2}}$
***LCCL*-S**	$\frac{\omega_s L_s}{R_e}$	$\frac{k^2 {\omega_s}^2 L_p L_s}{R_e}$	$\frac{V_{inv}}{\sqrt{Z_r(1-\alpha)^2+\frac{(\alpha+\beta-\alpha\beta)^2}{{\omega_s}^2 {C_{fp}}^2}}}$
***LCCL*-P**	$\frac{R_e}{\omega_s L_s}$	$\underbrace{k^2 {\omega_s}^2 L_p C_s R_e}_{\Re(Z_r)} - j\underbrace{k^2 \omega_s L_p}_{\Im(Z_r)}$	$\frac{V_{inv}}{\sqrt{\Re(Z_r)(1-\alpha)^2+\left(\Im(Z_r)+\frac{\alpha+\beta-\alpha\beta}{\omega_s C_{fp}}\right)^2}}$
LCCL*-*LCCL	$\frac{L_s R_e}{\omega_s {L_{fs}}^2}$	$\frac{k^2 {\omega_s}^2 L_p L_s C_{fs} R_e}{L_{fs}}$	$\frac{V_{inv}}{\sqrt{Z_r(1-\alpha)^2+\frac{(\alpha+\beta-\alpha\beta)^2}{{\omega_s}^2 {C_{fp}}^2}}}$

Table 7.3: Relations between control efforts and DWPT tank quantities. [1,2].

Inverter	$V_{inv}(\phi_{inv})$	$V_{inv}(D_i)$	**Secondary dc-dc**	$R_e(D_o)$
Voltage-fed	$\frac{2\sqrt{2}V_{in}}{\pi}\sin\left(\frac{\phi_{inv}}{2}\right)$	$\frac{2\sqrt{2}V_s D_i}{\pi}$	***C*-filter and buck**	$\frac{8R_{load}}{\pi^2 {D_o}^2}$
			***C*-filter and buck-boost**	$\frac{8R_{load}(1-D_o)^2}{\pi^2 {D_o}^2}$
Current-fed	$\frac{\pi V_{in}}{2\sqrt{2}\sin\left(\frac{\phi_{inv}}{2}\right)}$	$\frac{\pi V_s D_i}{2\sqrt{2}}$	***LC*-filter and boost**	$\frac{\pi^2 R_{load}(1-D_o)^2}{8}$
			***LC*-filter and buck-boost**	$\frac{\pi^2 R_{load}(1-D_o)^2}{8{D_o}^2}$

CHAPTER 8

Control Performance Comparisons and Effects of Communications in DWPT Systems

The analytical expressions for different compensation topologies and control handles in DWPT, discussed in Chapter 7 are used here to compare their control performance. In track with the main goals of DWPT controls stipulated in Chapter 7, the control performances are judged based on their capability to achieve good regulation with varying coupling k and high resolution controls. At first, performance metrics are developed to ascertain the above factors, and based on them the control performances are compared through simulation plots for an example 50 kW DWPT system.

8.1 Performance Metrics

For defining the control performance metrics, the ideal target of achieving full decoupling between output power (P_{out}) and changes in coupling (k) is considered. The ideal scenario can be explained as

$$\frac{dP_{out}}{dk} = 0 \ . \tag{8.1}$$

Since this is not achievable in practice, controls are used. The requirement of variations in control inputs for desired regulation in P_{out} can be figured out by expanding the expression of $\left(\frac{dP_{out}}{dk}\right)$ in terms of a general control input c as

$$\frac{dP_{out}}{dk} = \frac{dc}{dk}\frac{dP_{out}}{dc} = \frac{dc}{dk}\left(\frac{dc}{dP_{out}}\right)^{-1} \ . \tag{8.2}$$

From (8.2), it can be inferred that minimizing $\left(\frac{dc}{dk}\right)$ and maximizing $\left(\frac{dc}{dP_{out}}\right)$ will help achieve control performances closest to (8.1). The former indicates a low required change

in control with variation in k for power regulation. This allows for easier controls with even larger changes in k. The latter indicates a low sensitivity between P_{out} and the control input. This helps in achieving precise control in power flow. Hence their combination leads to precise control over P_{out} with minimal variation with k, which are the desired objectives in EV DWPT controls. For example, the push-pull topology used along with PP compensation and primary side converter control [36] achieves a high $\left(\frac{dc}{dk}\right)$ at varying loads. Thus it requires very precise control from the primary converter in the face of coupling variations.

Also, both the factors $\left(\frac{dc}{dk}\right)$ and $\left(\frac{dc}{dP_{out}}\right)$ are functions of the selected compensation topology and control input. Hence these factors are considered as the performance metrics for comparisons of control performances of DWPT systems, which are expected to work as guidelines for the selections of compensation topology and control configurations for better control performances.

8.2 Comparison of Control Performances

For the choice of control handles for comparisons, the general DWPT system diagram in Fig. 1.12 is considered. Without loss of generality, the primary side electronics can be represented as a dc-dc converter and a single-phase inverter, with a passive rectifier followed by the back-end dc-dc converter. Corresponding to this general system configuration, the front-end converter duty ratio (D_i), the inverter phase shift between its legs (ϕ_{inv}) and the duty ratio of the back-end converter (D_o) are considered as the control inputs. For the comparisons, in each case one control input is selected while keeping the others disabled.

For comparison of control performances, designs of a 800 V input, 800 V output, 50 kW DWPT system using the different existing compensation topologies are considered. Electromagnetic simulation model of a typical DWPT system with multiple-pad primary and single-pad secondary is shown in Fig. 8.1(a), and the typical coupling profile obtained from it along the road is shown in Fig. 8.1(b). It shows that the typical range of coupling where power needs to be regulated are 0.1 to 0.3. Hence this range is considered for the performance comparisons in this paper, with all the designs performed for a nominal coupling

of 0.2 with zero misalignment. As the vehicles drive over the pads, the vibration caused in the roads can cause additional variations in these profiles. However, the profile shown in Fig. 8.1(b) still demonstrates a typical profile encountered along the road in a DWPT system, and an analysis based on it will still hold for high-speed vehicles. Also, the stationary EV WPT standard operating frequency of 85 kHz is used in the analysis, since most of the EV DWPT works look to conform to this. Since the performance of the LC-type compensated systems are only governed by the operating frequency and coupler designs, the SS topology design is used to fix the coil self-inductances L_p and L_s. The same coils are used for all the other topologies. For this, verification were performed so that desired power controls while using the other topologies are possible with either front-end or back-end converter duty ratios in the acceptable range of 0.05 to 0.95. Also, the additional L and C parameters in the higher order compensation topologies were selected to meet the above control range. The parameters used in the simulations of the different topology designs are put in Table 8.1. For the hybrid topology shown in Fig. 7.2(g), inductance of each half of the primary DD pad ($L_{pt,1}$ and $L_{pt,2}$) is considered to be equal to $\frac{L_p}{2}$ and similarly inductance of each half of the secondary DD pad ($L_{st,1}$ and $L_{st,2}$) is considered to be equal to $\frac{L_s}{2}$. Also the predominant mutual inductance terms M_{12} and M_{34} have only been considered, with M_{34} having a negative value, as per the considerations in [21].

Without loss of generality a buck converter at the front-end and a buck-boost converter at the back end are considered. The comparison results are only demonstrated with D_o and D_i as control inputs. When D_o is controlled, the front-end converter is considered absent. Similarly for D_i is control, the back-end converter is considered absent. Because of the sinusoidal relationship between inverter phase shift and the tank voltage, the variation in phase shift control are always larger than duty ratio control. Moreover, inverter phase shift control needs considerations for zero voltage switching, which can be better achieved if controls are exercised through front-end or back-end converters.

For comparison plots, the variations in D_o and D_i with change in coupling in the range as per Table 8.1 and $\pm 10\,\%$ change in desired P_{out} are considered. The PP topology is

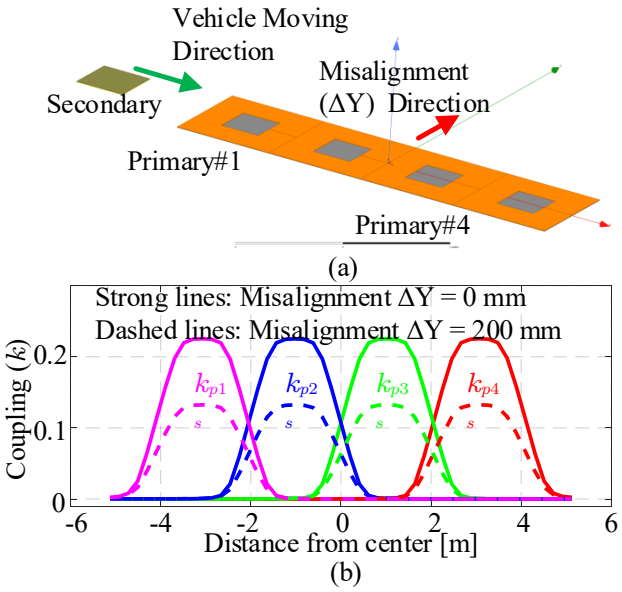

Fig. 8.1: (a) Model of DWPT system with multiple primary pads and single secondary pad, (b) Typical coupling profile along the roadway without and with Y-direction misalignment (ΔY).

Table 8.1: System design parameters for control performance comparisons.

Parameter	**Values**
$\boldsymbol{V_s}$ [V]	800
$\boldsymbol{V_{out}}$ [V]	800
$\boldsymbol{k_{nom}}$	0.2
$[\boldsymbol{k_{min}}, \boldsymbol{k_{max}}]$	[0.1, 0.3]
$\boldsymbol{L_p}$ [µH]	50
$\boldsymbol{L_s}$ [µH]	50
$\boldsymbol{f_s}$ [kHz]	85
$\boldsymbol{P_{out}}$ [kW]	50

excluded from the comparisons as it demands larger input voltages compared to the others for the same power levels, which is also commensurate with the analysis in [128]. The plots for all the other topologies are shown in Fig. 8.2, where normalized variations in control efforts with variations in coupling and desired output power are compared. The D_o vs k plots for the different topologies are shown in Fig. 8.2(a). This figure demonstrates that the topologies achieving relatively lower change in D_o vs k are found to be SS (both at zero and lagging primary phase angle), *LCCL*-S and *LCCL-LCCL* at lagging phase angle, *LCCL*-P with zero phase angle and the series hybrid topology with the factor m defined for this topology in (7.4) chosen near the nominal coupling value. Among them, the lowest percentage variation in D_o vs k is observed with the series hybrid topology. Especially the variation in the plot for series hybrid topology occurs because in the expressions (7.3)-(7.4) an ideal system with no losses and no negative coupling between each half of the primary DD pads are considered. In a real system with the pad ESRs and the negative couplings, considerably lower variations of D_o vs k are obtained, as demonstrated in [21].

On the other hand, the D_i vs k plots for the same topologies are shown in Fig. 8.2(b). It shows that only SS and *LCCL-LCCL* topologies operated with lagging primary phase angle achieve lower variations in D_i vs k. The same argument presented above for the series hybrid topology is also applicable here, which indicate a considerably lower variation in the D_i vs k plot for this topology in a practical system. However, the plots in Fig. 8.2(b) also demonstrate that the variations in D_i as control input with variations in k are larger than D_o control for almost all topologies.

For variation in desired P_{out}, plots of D_o vs P_{out} for the same topologies are shown in Fig. 8.2(c). This plot demonstrates that the topologies offering low variation in D_o vs k also have low variation of D_o vs P_{out}. On the other hand, the D_i vs P_{out} plots are not included in Fig. 8.2, as these plots were found to be topology invariant. However the percent change in D_i vs P_{out} from the peak value was found to be around 10 %, which was larger than the percentage variation in D_o vs P_{out} with D_o control.

The outcomes of the above analysis and comparisons demonstrate that it is not possible

to select a particular topology or control scheme to achieve both requirements of (8.2). However, a little more inspection reveals that, the deviations in control inputs are larger with varying k than with the variation in desired power output. Hence for topology selection, more importance can be given to performance against varying k. In this regard, the SS, *LCCL*-S, *LCCL-LCCL* topologies designed with lagging primary phase angle and series hybrid topologies with D_o control performs better. The lagging phase angle design of the primary sides in these topologies, achieved through proper selection of the parameters α and β in Fig. 7.3 [2]. Even though the series hybrid topology provides better performance against variations in k, it leads to a very sensitive power flow control compared to the others, as per Fig. 8.2(c). Among the control inputs, the secondary side D_o control provides better performance than primary side D_i control due to their relatively smaller variations with k for all topologies.

8.3 Effects of Communications

Communications and the effects of delay introduced by them are important to consider for primary or dual-side DWPT controls using feedback from the secondary [18]. Considering the typical scenario of regulating P_{out} within an amount $\pm\Delta P_{out}$ with a communication delay of t_l, the condition for successful regulation can be written as

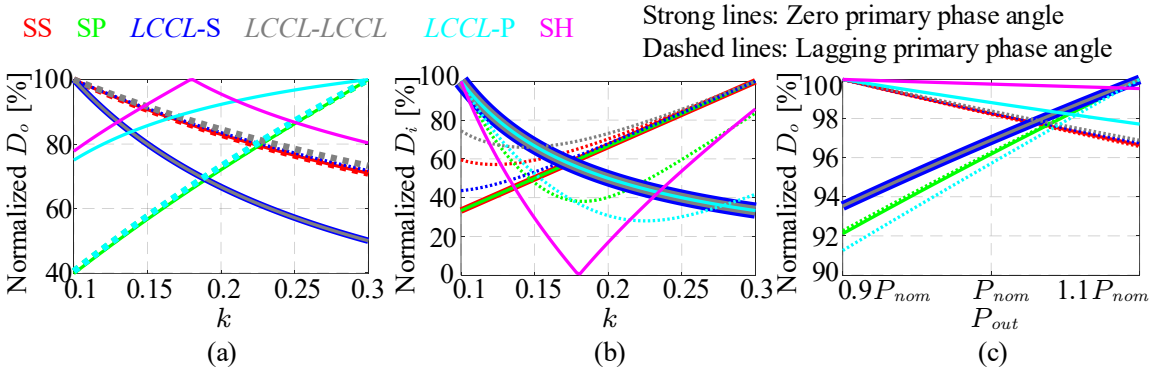

Fig. 8.2: Comparison of control performances for different compensation topologies using D_o control with buck-boost converter and D_i control with buck converter, (a) Normalized D_o vs k, (b) Normalized D_i vs k, (c) Normalized D_o vs P_{out}.

$$\frac{\Delta P_{out}/P_{out}}{t_l} \geq f(M)\ \Delta M|_{t_l}\ , \tag{8.3}$$

where the function $f(M)$ depends on the compensation topologies and $\Delta M|_{t_l}$ is a function of the rate of change of mutual inductance $\left(\frac{dM}{dt}\right)$. The expressions of $f(M)$ for the different topologies considered in the previous section are shown in Table 8.2. For the series hybrid topology the variable M_{sh} is incorporated to denote the equal magnitudes of the inductance M_{12} and M_{34}, which are in magnitude half of the M used for the other topologies.

On the other hand $\left(\frac{dM}{dt}\right)$ is a function of the vehicle speed v_v and coupler dimensions, which can be figuratively expressed for rectangular primary and secondary pads of lengths $l_{pad,pri}$ and $l_{pad,sec}$ as

$$\frac{dM}{dt} = g(v_v, l_{pad,pri}, l_{pad,sec})\ , \tag{8.4}$$

which for the square shaped pads assumed in Fig. 8.1(a) can be written as

$$\frac{dM}{dt} = \frac{v_v \Delta M}{l_{pad,pri}}\ , \tag{8.5}$$

Table 8.2: Expressions of $f(M)$ for SS, *SP*, *LCCL-S*, *LCCL-P*, *LCCL-LCCL* and Series Hybrid topologies.

Topology	$\boldsymbol{f(M)}$
SS	$-\frac{2}{M}$
SP	$-\frac{2}{M}$
***LCCL*-S**	$\frac{2}{M}$
***LCCL*-P**	$\frac{2}{M}$
LCCL-LCCL	$\frac{2}{M}$
Series Hybrid	$\frac{2}{M_{sh}} \frac{L_{pt,2(LCL)} L_{st,2(LCL)} + {M_{sh}}^2}{L_{pt,2(LCL)} L_{st,2(LCL)} - {M_{sh}}^2}$

where relevant conversion factors need to be introduced if v_v is in mph and $l_{pad,pri}$ is expressed in m. Using this relation, the effects of communication on DWPT controls with different couplers and compensation topologies can be compared.

As examples of the comparative analysis, at first two design cases were considered from the existing works which uses two different coupler shapes and nominal inductances [3, 4]. Both uses $LCCL$ primary compensations, and hence corresponding expressions are used from Table 8.2. The maximum vehicle speed permissible (v_{vmax}) for a $\pm 10\,\%$ power regulation with typical Bluetooth communication delay of 6 ms [91] and the maximum communication delay limits (t_{lmax}) for charging at 80 mph for these designs are presented in Table 8.3. It can be found that coupler configurations having lower $\left(\frac{dM}{dt}\right)$ and higher mutual inductance would be beneficial for DWPT with communication based feedback, which are mostly available with larger pad designs.

Further, comparisons are performed for communication effects with different topologies used for the example 50 kW designs earlier in this chapter, using the coupler arrangements and coupling plots shown in Fig. 8.1. Corresponding expressions of $f(M)$ were used in (8.5) for this purpose. The results of this comparison is summarised in Table 8.4.

The results for $LCCL$ or series compensations and the considered pad dimensions further corroborate that larger pads lead to better performances in charging high-speed cars despite communication delays. However with presently available communication protocols,

Table 8.3: Comparison of effects of communication delay on charging a moving vehicle for the considered design cases [3, 4].

Study cases		Design 1	Design 2
M_{nom} [µH]		14.3	12.5
$t_l = 6$ ms	$\left(\frac{dM}{dt}\right)_{max}$ [nH/s]	7.75	10.1
	v_{vmax} [mph]	20.5	7.2
$v_v = 80$ mph	$\left(\frac{dM}{dt}\right)$ [nH/s]	30.2	111.7
	t_{lmax} [ms]	1.5	0.5

Table 8.4: Comparison of effects of communication delay on charging a moving vehicle for the considered 50 kW design with different primary compensation topologies..

Primary compensation		Series or *LCCL*	Series hybrid
M_{nom} [µH]		10	10
$t_l = 6$ ms	$\left(\frac{dM}{dt}\right)_{max}$ [nH/ms]	83.3	4.4
	v_{vmax} [mph]	37.28	3.92
$v_v = 80$ mph	$\left(\frac{dM}{dt}\right)$ [nH/ms]	178.8	89.4
	t_{lmax} [ms]	2.8	0.3

it is still beneficial to design local feedback based systems for dynamic charging of high-speed vehicles. Moreover, the comparisons show that the series hybrid topology, designed with m in (7.4) close to nominal coupling for low control command variations, leads to poor performance when comes to regulating power for high-speed vehicles. However that is the situation where it provides the lowest variation in control effort with coupling. Hence this topology is very sensitive to the design conditions.

8.4 Recommendations for Future Research

From the control perspective, both the N-S poles across the road and waterfall type flux patterns perform the best, providing the best coupling profile. Among them, the former has single-sided flux, leading to higher coupling with lower shielding. However, the N-S poles along road coupler type is the most suitable to be interoperable, as discussed in Chapter 7. Even though it has to take care of the zero coupling zones, the usage of proper compensation topology, converter topology and efficient detection system help in reducing the power flow ripple. Effective single or multi-phase inverters driven at constant duty ratio and phase shift are best suited for reliable operation. Among detection methods, the free-resonance based method provides both closed loop detection with minimal additional hardware overhead.

The choice of the compensation topology is critical for control performance. As per the control performance comparisons presented above, the SS, *LCCL*-S and *LCCL-LCCL*

topologies with optimized, lagging primary phase angle design are recommended for future research. These also provide better ZVS operation, giving better efficiency and EMI performance. They are also better for being interoperable with other compensations, which is the principal drawback of series hybrid topology. However, for specific cases where interoperable behavior is not required, the series hybrid topology can be used for better power flow control with varying k. Hence these topologies should be focused for future developments to drive EV DWPT systems towards widespread commercialization. The choice among the SS, *LCCL*-S and *LCCL-LCCL* can be made based on the primary pad current, output voltage and current characteristics, power ratings and system volume considerations, in the lines of [128].

It was also shown that secondary side controls are more beneficial compared to primary side controls. They not only provide better performance against varying k, but also against high rate of change of coupling. Hence the secondary side controls are recommended for future works for better feedback controls. It is especially important for high-speed vehicle charging on highways, as feedback communication based primary side controls are not recommended for them as per the results in Table 8.3 and Table 8.4. Hence the vehicles should be equipped to control power flow for charging on highways. Alternatively, dedicated lanes with strictly enforced speed limits can be used along the highway for dynamic charging with lower bandwidth controls. This can enable operation with primary side controls, but that too will be limited to very slow vehicles. Fitting the vehicle with the maximum possible number of pads with the largest possible dimensions will lead to minimizing the control requirements.

CHAPTER 9

Conclusions and Future Works

While wireless inductive power transfer (IPT) has seen great growth in the areas of charging of stationary electric vehicles, biomedical implants and mobile phone charging, the emerging areas of IPT include charging of autonomous underwater vehicles and dynamic charging of electric vehicles. This dissertation focused on a few important areas of development in these emerging areas of IPT applications. In the first part of the work focused towards AUV charging, the aspects of loss modelings of underwater IPT coils, their optimizations for high-frequency underwater IPT for small AUV applications and analysis and design of topologies suitable for operating with a underwater current distribution system were addressed. The analysis and design were validated with experimental prototypes of up to 1 kW power ratings. In the second part, the existing EV DWPT topologies and their control schemes were critically reviewed and compared for analysis of their control performances. The importance of choice of compensation topologies, front-end or back-end converter controls and effects of communications were analyzed. The results were demonstrated through comparative plots for example 50 kW DWPT system designs with different compensations and control implementations. In addition to the above tasks accomplished in this dissertation, a few ideas got developed which could not be sufficiently addressed. This chapter provides a summary of the main contributions from the works accomplished in this dissertation and brief overview of some of the ideas generated from this dissertation which can be addressed in future research work.

9.1 Summary of the Contributions

The following are the main contributions of the present dissertation work:

9.1.1 Eddy Loss Model and Optimizations for Circular Spiral Coils for Underwater IPT

The dissertation presented an approximate integral based eddy loss model for circular spiral coils in underwater IPT system. The expressions were developed to simplify the estimation of eddy losses, accurate up to 15 % as compared to the difficult field based methods present in literature. The model was also used for optimization of small-size, high-frequency coils for underwater IPT, such that the operating frequency threshold in existing underwater IPT system could be increased without compromising efficiency. The validations of the loss models and optimizations were provided with the help of a proof-of-concept 1 kW constant voltage input IPT system, for which the coils were designed as air core and following the analytical optimization results.

The model and the analytical optimization developed is useful in finding ball-park range of coil inductances and dimensions before running FEM simulations with lower design points. Since the model takes care of the litz wire construction details and their effect on ac resistances, it is useful in finding out loss distribution among different loss sources in underwater IPT coils.

9.1.2 Development of Constant Current Input IPT Topology for Constant Voltage Output

As the state of the art constant voltage input IPT systems with low operating frequencies were not found suitable for small AUVs in advanced marine systems with constant current distribution, IPT topologies to interface with such current distribution systems were developed. With a requirement to generate a constant voltage output through the IPT system, potential topologies and their characteristics were analyzed. Based on that, two topologies using series-series (SS) compensation, one with a current-boost transformer and one without the current boost transformer were proposed for minimum system volume.

Steady-state analysis of these topologies were presented to demonstrate the constant voltage characteristics and the effect of system non-idealities on the characteristics. Based on these, key design challenges were identified for the design of these topologies.

These topologies demonstrate constant output voltage characteristics and also have load-independent primary coil current, when operated at resonance. Hence they can be operated at no-load or at uncoupled conditions with the input voltage reaching zero and delivering no power. This is an important improvement since typical dc voltage input SS IPT topologies are not operable at any of the above conditions due to the current reaching dangerously high levels.

9.1.3 Design Considerations of Constant Current Input SS IPT Topology

The design challenges coming out from the steady-state analysis were carefully addressed for the design of the constant dc current input underwater IPT topologies. The considerations included the current to voltage conversion ratio, transformer design and selection of quality factor ranges for the tanks for the transformer based design. In addition to them, the effect of misalignment and mistuning on current to voltage conversion ratio, coil VA ratings, DCM conditions of the secondary tank, output power expression and its dependence of the resonant tuning and component sizing for single-stage realization of the system with large number of turns on primary coil and small number of turns in the secondary coil were considered for the transformerless topology up to 1 kW. The experimental prototypes built with similar parameters were used to validate the effectiveness of these design procedure, with the 1 kW prototype demonstrating acceptably constant voltage characteristics in a wide power range of 300 W to 1000 W under nominal, maximum and minimum coupling positions and achieving underwater power transfer efficiencies above 90 % under all conditions.

The design considerations presented in this part of the work are useful to optimize the system with respect to conflicting requirements such as lowering VA ratings for reducing copper volume and achieving high quality factors to avoid DCM and minimize effects of mistuning. Thus the design procedure can be extended to similar SS IPT system designs in

any applications for achieving constant voltage characteristics in wide load range and with high efficiency.

9.1.4 Small-signal Phasor Modeling of Constant Current Input SS IPT Topology

In addition, small-signal modeling of the constant dc current input underwater IPT topologies were presented using small-signal phasor modeling technique. It was shown that the steady-state mutual inductance model is applicable for the small-signal modeling of the mutual inductance effect. Then the model was developed using the phasor transformer model of inverter and inverter and second-order simplified model of a series resonant tank for the primary and secondary compensation networks. From the model, circuit analysis was used to find transfer function between inverter phase shift angle and output voltage. From the transfer functions, the pole and zero locations were identified and it was shown that the input capacitor affects the right half plane zero location. Also a potential control loop structure was presented, based on the negative dc gain characteristics of the system.

The model and the insights gained into the dynamics of the system are useful in the stability analysis and controller designs of the system. The model can also be extended to current and voltage input SS IPT systems. The small-signal phasor modeling is also better in terms of gaining more insights of the system compared to the typical generalized state-space models and extended describing function methods.

9.1.5 Critical Review of Topologies and Controls in EV DWPT

On the other part of the dissertation focused on controls in EV DWPT, a comprehensive review of existing couplers, converter topologies, compensation topologies and control schemes were performed. It was shown that larger or more complicated couplers are typically required to obtain flat mutual inductance profile along the roadway and the converter topologies determine what type of controls can be exercised. On the other hand, it was shown that the compensation topologies modify the relation between mutual inductance profile and the power transfer profile, such that they can be properly selected to obtain

better power flow controls without the need to use complicated couplers. The review of control schemes brought out that the closed-loop controlled systems provide higher stability with simpler hardware designs, but only secondary side converter controls are suitable for communicationless control implementations.

The review is useful for understanding the functionality of each stage of an EV DWPT system in achieving power flow control. The outcomes can be useful in future works on DWPT systems.

9.1.6 Comparison of Control Performances through Performance Metrics

Using the review points mentioned above, comparisons of control performances were performed between different compensation topologies and different control handles. To compare the performances, the performance metrics such as variation of control effort with coupling $\left(\frac{dc}{dk}\right)$ and variation of control effort with desired range of power flow control $\left(\frac{dc}{dP_{out}}\right)$ were developed. It was shown that minimizing the first and maximizing the second performance metrics would lead to high resolution controls in DWPT with minimal variations with coupling, which indicates better control performance. Using these metrics, the control performances of typical compensation schemes such as SS, SP, *LCCL*-S, *LCCL*-P, *LCCL*-*LCCL* and series hybrid were shown with duty ratio controls in the primary side and secondary side. For the comparisons, an example 50 kW DWPT system with identical coils were designed using the different compensations and the different front-end or back-end dc-dc converters. Then the plots obtained from MATLAB simulations were used to compare the control performances in terms of the developed performance metrics. It was demonstrated that the SS topology and the primary *LCCL* based topologies perform better than the others, while the choice between them can be made considering other factors such as filtering of coil current harmonics and availability of load-independent primary pad current. Also it was shown that secondary side dc-dc converter controls perform better than primary side converter controls.

The performance metrics and the comparison method presented is applicable to any topology to judge the effectiveness of controls. Hence they can be applied for DWPT

systems to endure improved controllability.

9.1.7 Analysis of Effects of Communication Delays in EV DWPT Controls

The effects of communications on feedback controls of DWPT systems were also analyzed through the analytical expressions. For this, a relation was found between vehicle speed, pad dimensions and the rate of change of mutual inductance. Then, using the relevant expressions, comparisons were performed between at first between two types of coupler designs and then between different compensation topologies. It was shown that larger couplers show slower variation in mutual inductance, such that larger communication latencies are permissible. On the other hand, series hybrid topology was found to be unsuitable for communication based control systems except for a narrow range of designs. Moreover it was shown, that with the presently available communication protocols and associated latency, dynamic charging of high-speed vehicles with communication-dependent feedback is not recommended. This also led to the recommendation that secondary side controls could be better for future DWPT systems.

9.2 Future Works

In addition to the contributions summarised above, a few future research directions were identified during the completion of this dissertation work. A brief information about them are provided in this section.

9.2.1 Validation of Small-Signal Model Through Experimental Measurements

The small-signal model developed for the constant dc current input IPT system can be validated through experimental measurements using pseudo-random binary sequence (PRBS) injection into the phase shift command. The PRBS represents a band-limited white noise in digitally controlled systems [129, 130]. It contains a string of binary “0” and “1” pulses with varying time widths, generated to capture the response of a system in a desired band of frequencies, with the smallest pulse width equal to the inverse of selected sampling frequency. To experimentally measure the small-signal response of the phase-shift

controlled IPT system, the PRBS sequence is to be injected in the phase shift command. Then the output voltage response is to be recorded in a synchronized manner, and then processed to get the frequency response.

The work is already in progress, with the block-diagram of the PRBS injection, data recording and post-processing stages as shown in Fig. 9.1, which is adopted from [129]. The pre-emphasis and de-emphasis blocks are used to use higher step values for higher-frequency perturbations, such that at higher frequencies the attenuated responses can be properly captured without getting corrupted by the ADC noise floor. For the IPT system, the phase-shift command with pre-emphasised PRBS is generated in the primary FPGA and a synchronization signal is sent to the secondary FPGA for using to record the ADC data. The data is captured in MATLAB and processed through de-emphasis, FFT and fractional-decade filtering to filter out most of the measurement inaccuracy and get a smoothed frequency response. Initial results have already been captured for this work, which approximately match with the analytical frequency response shown in Chapter 6. However some more fine-tuning is required to make the experimental measurements match better with the analytical model, such that the model can be experimentally validated.

9.2.2 Closed Loop Control of the Underwater IPT System

The steady-state and small-signal analysis presented in this dissertation can be used for closed loop controls of the phase shift controlled underwater IPT system. The expressions developed will be useful for stability analysis under different operating conditions, and a control scheme similar to Fig. 5.6 can be implemented. The PRBS injection based system identification can also be used to automate the control loop designs for different operating conditions. However, the closed loop phase shift control operation needs considerations for achieving closed loop active ZVS as well, otherwise ZVS cannot be maintained under all conditions.

Both the primary and secondary converter boards were designed with voltage and current sensors for closed loop operation. The sensors were tested for proper operation. The primary board is also equipped with circuitry to control active ZVS operation through

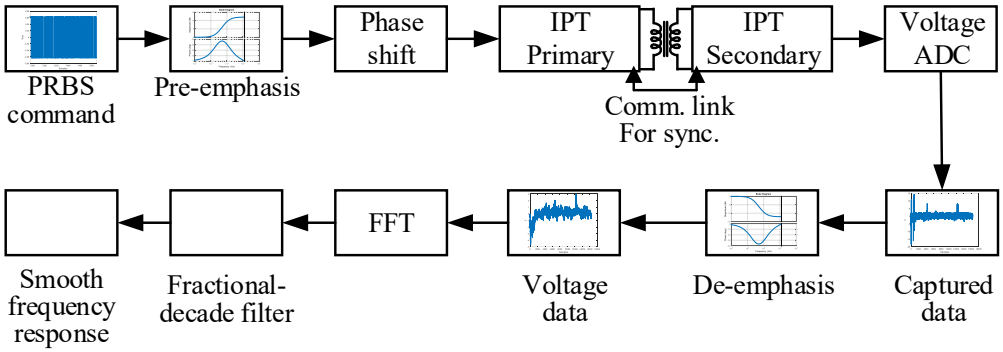

Fig. 9.1: Block-diagram of PRBS injection and data processing stages for experimental validations of the small-signal model of the constant dc current input underwater IPT system.

analog integrators connected with sensed tank current and active ZVS currents. A pictorial view of the primary board is shown in Fig. 9.2 depicting the associated sensors and active ZVS control circuits. The components were also populated for these circuits, so that they can be directly utilized for closed loop control operation with full active ZVS control of the constant dc current input underwater IPT system.

In addition, an energy buffer can be added to the input if wide bandwidth controls are to be implemented along with the input current distribution cable. The developed small-signal model and its validation method can be of special importance for such designs, as the system identification is necessary for high-bandwidth controller designs.

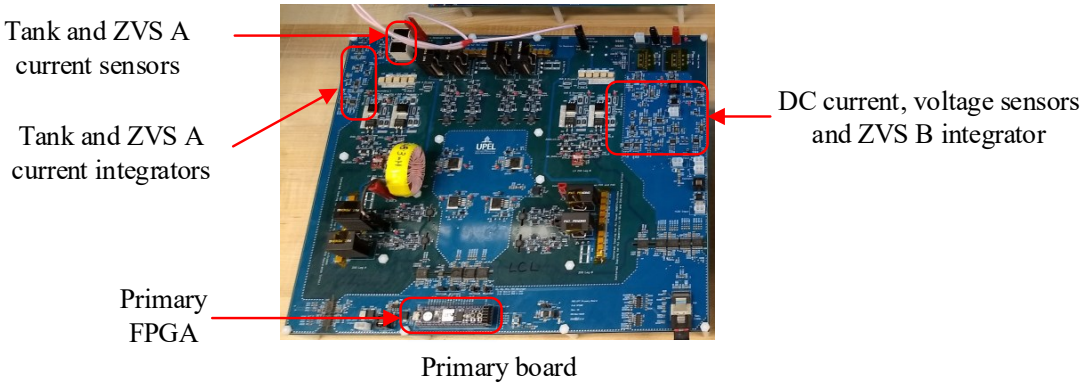

Fig. 9.2: Primary board pictorial view showing locations for dc voltage and current sensors and current integrators for controlled active ZVS operation.

9.2.3 *LCCL-LCCL* Compensated IPT Topology for Underwater IPT with Current Distribution

It was mentioned during the review on compensation topologies, that an alternative to the used series-series (SS) topology can be the of *LCCL-LCCL* compensation. A more detailed analysis of compensations presented in Chapter 7 shows that the SS and *LCCL-LCCL* compensated IPT systems possess identical input and output characteristics, such that both produces constant current output with constant dc voltage input, and constant voltage output if the primary H-bridge is driven with a constant current input. So this topology can be developed for AUV wireless charging with constant current distribution, as shown in Fig. 9.3.

The *LCCL-LCCL* compensation results in bigger tank volume, but it provides higher order filtering of the current harmonics. Moreover, the switching dv/dt does not appear across the coils this topology due to the presence of additional inductors (L_{fp} and L_{fs}) near the H-bridges. Hence the coils mostly run with sinusoidal currents, which is not maintained in the present SS IPT system at higher input voltage operating points, as shown in the waveforms in Chapter 6. As a result the *LCCL-LCCL* compensated system in underwater IPT can lead to better EMI behavior and also lessen the effect of any capacitive coupling between the primary and secondary coils through the seawater.

Typically *LCCL-LCCL* compensations are employed in medium power applications of electric vehicle dynamic charging (EV DWPT), where the couplings are often much lower than the AUV wireless charging applications. Similarly proper power range can be identified where the increase in tank volume and additional parasitic losses in the *LCCL-LCCL* tank do not offset the advantages of achieving a sinusoidal coil currents. The other possible advantage of the *LCCL-LCCL* topology is that potentially identical coils can be used for the underwater coupler, with the required current level translation obtained through proper selection of the resonant elements (L_{fp}, C_{fp} on the primary side and L_{fs}, C_{fs} on the secondary side).

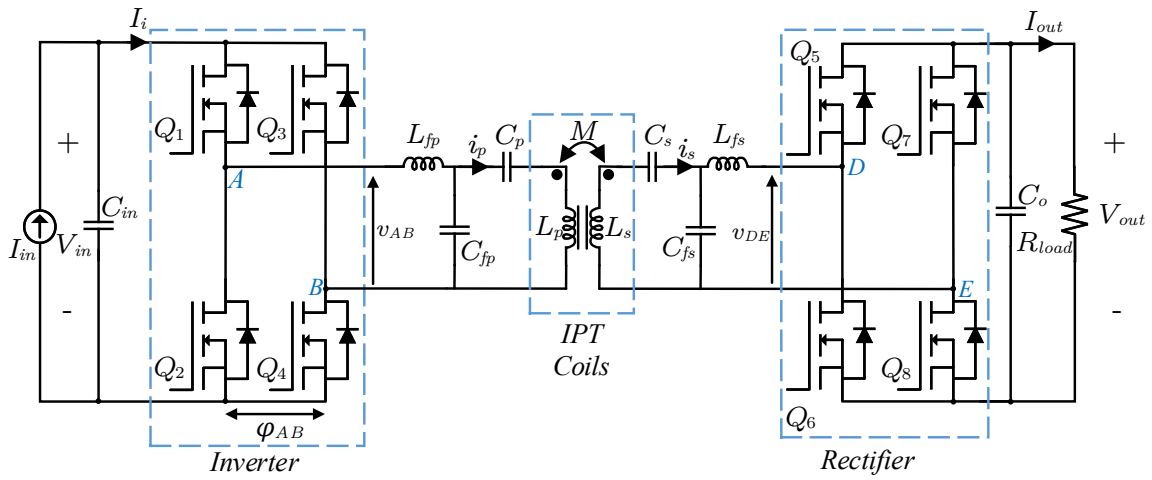

Fig. 9.3: Circuit diagram of underwater IPT system with constant dc current input and constant voltage output using *LCCL-LCCL* compensation.

9.2.4 DWPT System with Current Distribution

Similar *SS* and *LCCL* type topologies with voltage-fed inverter can be utilized for DWPT systems with current distributions. This will help long-distance dc power distribution systems for DWPT, using low-current cables, and synchrononization between consecutive DWPT units through a dc distribution link. Usage of the *LCCL-LCCL* topologies can be also beneficial for higher power designs, with the inverter capable of being designed for easy ZVS operation up to very high input voltage.

9.2.5 Bidirectional Underwater IPT System with Constant Current Distribution

The designed prototype for the 1 kW underwater IPT system with active switches on both side can be used for bidirectional power flow. A schematic diagram for the bidirectional power flow is shown in Fig. 9.4, where the system generates a constant voltage output from a constant current input in the forward power flow and on the contrary, generates a constant current output from a constant voltage input in the reverse power flow. The analysis of the reverse power flow mode is identical to the analysis provided for the constant voltage input IPT system in Chapter 3. A similar topology can be designed with *LCCL-LCCL* compensation too, for the reasons mentioned above.

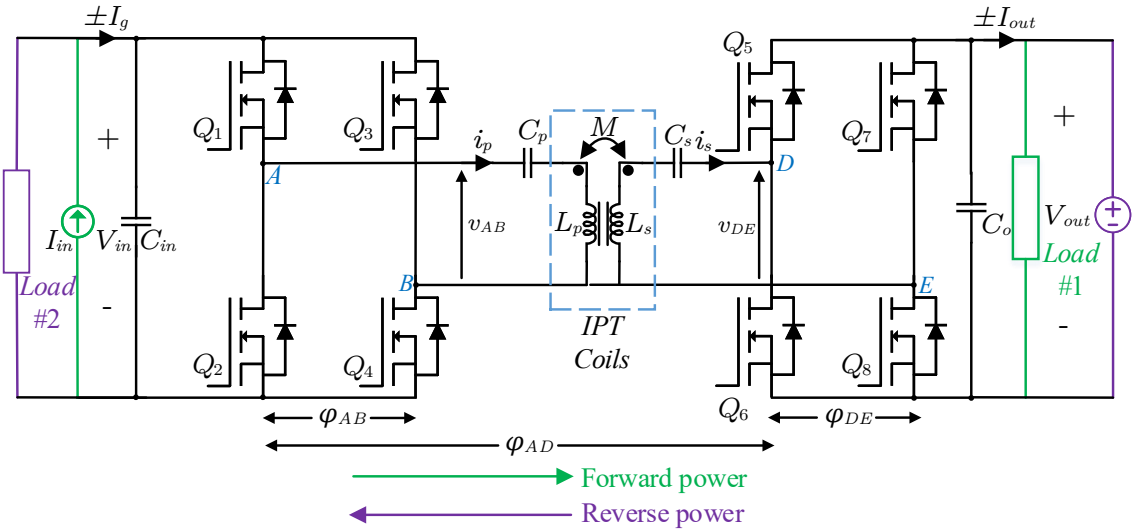

Fig. 9.4: Circuit diagram of bidirectional underwater IPT system in constant current distribution using SS compensation.

The primary and secondary converter boards shown in Fig. 6.11 are both equipped with circuitry to operate the system with bidirectional power flow. Due to the use of a voltage-fed H-bridge with MOSFET switches in both primary and secondary, they are not capable to operate as a bidirectional voltage system. Hence for the reverse power flow, a constant voltage input is to be connected on the secondary side dc terminals and the primary side dc contactors are to be reversed to take the constant current output, as shown in Fig. 9.4. This is typical for underwater distribution networks where the on-line changeovers between forward and reverse power flow is not required. A similar work was done for an *LCL-T* resonant converter in current distribution and demonstrated appreciable bidirectional power transfer performance, which can be replicated for the bidirectional underwater IPT system.

9.2.6 Active Rectifier Controls in IPT

The tank current sensor based synchronous rectification can be extended towards full phase shift control of the rectifier in an IPT system. For synchronizing the rectifier switches with the H-bridge inverter, typically multi-angle control with communication is required, leading to a dual-active bridge configuration. However, the rectifier side quantities such as

tank current or capacitor voltage can be utilized to synchronize the rectifier while running the inverter at full phase shift of 180 deg, such that communication dependencies can be avoided. Moreover, proper synchronization of the rectifier and its phase shift control can help in achieving ZVS in all the switches in the system with minimal assistance as per a few recent works in literature.

The above procedure can be especially beneficial in the bidirectional underwater IPT system in constant current distribution and secondary controls of EV DWPT systems. In the reverse power mode of the bidirectional underwater IPT system shown above, the high current secondary side works as the inverter and the high voltage primary side works as the rectifier. Phase shift control and active ZVS design for the high current secondary is challenging, and typically results in reduction in efficiency. On the contrary, phase shift control and active ZVS design for the primary is easier due to low currents and more beneficial due to high voltage across the switches there. So the active rectifier controls from only the rectifier side can help in communicationless implementation of the bidirectional underwater IPT system. The potential drawback can be inaccurate synchronization during the DCM occurring at low power operating points. However as per a few recent works, the capacitor voltages can be used to perform the synchronization, as the capacitor voltages remain sinusoidal despite the tank current going into DCM. This can be implemented in both SS or *LCCL-LCCL* compensated systems.

On the other hand, the DWPT systems are typically designed to operate near the nominal power rating whenever they are on, such that they do not need to consider the current distortions at lower power operations. For these systems, the tank current sensor output can be used to synchronize one leg of the rectifier, and drive the other leg with phase shift modulation. Thus communicationless vehicle side control without additional dc-dc converter stages can be achieved.

9.2.7 Modeling of EV DWPT Controls Including Speed of Vehicle

The relations derived in Chapter 8 between vehicle speed and rate of change of coupling and mutual inductance can be extended to better modeling of the system for controls. The

rate of change of mutual inductance can be transformed to the frequency domain using Laplace Transform. Then it can be plugged in the small-signal models for analysis of stability and controller designs.

Similarly, if communication based primary or dual-side controls are employed, the controller can be designed with consideration of the feedback delay along with the frequency domain model of mutual inductance changes. This can be effective in optimizing control implementations in dynamic EV charging systems.

9.2.8 Speed Controlled Charging Lane Concept in EV Dynamic Charging

Based on the findings of the communication delay effects on EV DWPT controls in Chapter 8, the DWPT systems can be designed in the form of dedicated charging lanes to efficiently use primary side or dual side controls. The charging lanes can be constructed on the side of the highways in regular intervals, where the vehicles needing charge can pull into and get charged while on the move. This will ensure both grid side and vehicle side controls can be ensured without large coupling pads and heavy on-board power electronics.

Smaller vehicles such as passenger cars can only house smaller coils due to their size constraints. Hence they will face higher effect of communication delays. So the lanes dedicated for such vehicles can be designed to have smaller speed limits. On the other hand, large vehicles such as hauling trucks or buses can house larger or multiple coils on the bottom of their chassis. Hence higher speed limits can be permissible for them.

Here are some of the key advantages of this concept:

- The speed controlled dynamic charging lanes will not block traffic on the highway
- It will let the cars charge on-the-go without having to stop, such that travel time will reduce. This will basically emulate a gas station model, but with moving vehicles rather than stopped ones.
- DWPT related maintenance activities can be constrained to specific places, rather than on the main highway. Hence implementations will be easier.

- Both grid side and on-board power flow controls can be utilized with optimally designed communications in a controlled area.

APPENDICES

APPENDIX A

Details of the Synchronous Rectification (SR) Circuitry

The synchronous rectification (SR) circuit is designed with a current sense transformer, two comparators and a decision making circuitry designed within the FPGA. The sensor circuit and the comparators generate the reference pulse for SR, as per the phase of the secondary tank current. Based on this pulse, the MOSFET gate signals of the secondary H-bridge are generated.

A.1 Sensor and Comparator Circuitry

The sensor and comparator circuitry as part of the SR oepration is shown in Fig. A.1. A current transformer (CT) is used to convert the secondary tank ac current into an equivalent voltage, riding upon a common-mode voltage of 2.5 V, to help in comparator designs following it.

Hysteresis comparator is used for both the positive and negative pulse comparators, as the magnetizing inductance of the current transformer causes a dc offset near the zero crossings of the current. Moreover, it also provides stability against the discontinuous operation of the rectifier at low power levels, where the tank current goes to zero for certain durations, where no devices should be kept on. As a result, the SR operation is available when the secondary tank current amplitude is sufficiently high and the waveform is mostly sinusoidal. For the positive pulse detector, the comparator is supplied 2.5 V reference at the negative input, such that its output goes high during the positive half-cycle of the

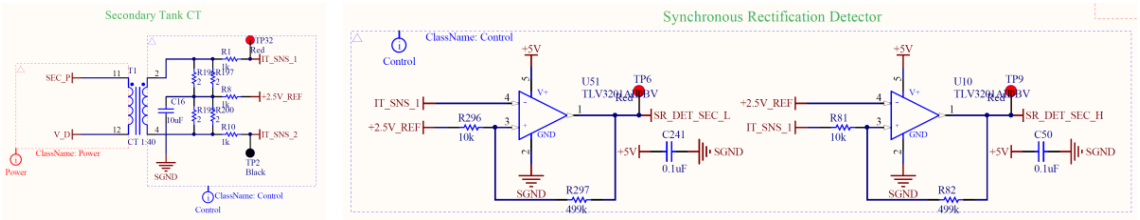

Fig. A.1: Current transformer and comparator circuit schematic used for detection of synchronous rectification pulses.

secondary tank current. On the other hand, the comparator for negative pulse detector, the reference is supplied to the positive input, such that its output goes high during the negative half-cycle of the secondary tank current. These two comparator outputs are sent to the FPGA to be used as reference signals for the SR gate signal generations. The positive half-cycle SR reference signal is available at 'SR_DET_SEC_H' and the negative half-cycle SR reference signal is available at 'SR_DET_SEC_L'.

A.2 FPGA Implementation of Synchronous Rectification

In the FPGA, the reference pulses are taken as inputs for SR signal generation, and a signal is defined for enabling or disabling the SR operation based on the secondary tank current amplitude. Also, a command decoder is created to enable or disable the SR operation from the computer terminal. In our experiments, the SR operation is enabled in open-loop after the output power (and hence the secondary tank current amplitude) is above 150 W, but output current sensor is kept in the board design such that the SR enable/disable operation can be achieved online.

When the SR enable signal is High and a rising edge is detected on 'SR_DET_SEC_H', the gate pulses for the switches Q_5 and Q_8 are turned high. The pulse width is kept controllable through a register, programmable from the computer terminals, with the maximum pulse width of 1.8 µs, such that the MOSFETs are turned off well before the currents going to zero. Similarly, the pulses for the switches Q_6 and Q_7 are generated synchronized with the rising edge of input signal 'SR_DET_SEC_L', with the same pulse width. This makes sure the SR operation with maximum pulse width is achieved and ZVS is ensured for all switches.

APPENDIX B

Controller Implementations and MATLAB Terminal Commands

B.1 FPGA Implementation of Controller and Synchronous Rectification

The basic gate signals are generated in FPGA though phase shifting counters, as mentioned in details in [131]. The phase shift commands for φ_{AB} and φ_{AZ}, pulse enable and phase shift enable commands are sent from the MATLAB terminals to the CMOD-A7 module plugged in the primary board, where they get executed as per the modules shown in [131]. Typically, for steady-state testing of the system, 8-bit addressed UART is used for communication between the MATLAB terminal and the FPGA. However, the PRBS based system identification requires 16-bit UART addressing is required. Hence, the FPGA codes are modified to use both 8-bit and 16-bit UART addressing schemes based on a third argument sent from the MATLAB terminal, explained in the next section.

The following code snippet shows the commands in the main secondary board module for SR operation, followed by the snippets for the different sub-modules.

```
// Top Module port definition
module TopModule{
    ...
    input sr_det_h, // Input signal SR_DET_SEC_H
    input sr_det_l, // Input signal SR_DET_SEC_L
    output wire [3 :0] SW_SEC, // Output gate signals
    ...}
    wire [3:0] gateSignal; // Secondary gate signals
    wire sync,sync_bar; // Buffered SR detect signals
    assign SW_SEC = GlobalEnable ? (gateSignal) : (6'b0);
                                    // Enable/disable gate signals
```

```
    assign sync = sr_det_h; // Assign buffered SR_DET_SEC_H
    assign sync_bar = sr_det_l;  // Assign buffered SR_DET_SEC_H
    // Set pulse width command
    always @ (posedge clk300_bufd) begin
        if(PARAMETERS[` P_SR_TON])
                SR_ton_cmd <= PARAMETERS[` P_SR_TON]; //Latch pulse width command
        else
                SR_ton_cmd <= 12'd340;  //1.36us based on 250MHz clock
    end
    // Module instance for SR gate signal generation
    pwm_gen_2 gate_signal(.clk(clk300_bufd), //250MHz clock
        .rst(rst), //Reset
        .sync(sync), // Buffered SR_DET_SEC_H
        .syncb(sync_bar), // Buffered SR_DET_SEC_L
        .srton(SR_ton_cmd), // SR Ton command
        .gate_sgnl(gateSignal)); // Gate pulses
endmodule
```

In the above code, the 'pwm_gen_2' module generates the SR gate signals based on the buffered reference input signals and pulse width commands provided to it, whose detailed codes are shown in the next snippet.

```
// Module port definition
module pwm_gen_2 (clk,  // Clock input
        rst, //Reset
        sync, // Input Sync HI
        syncb, // Input Sync LO
        srton, // On time
        gate_sgnl); // Pulse output
        input clk;
```

```
        input rst;
        input sync,syncb;
        input [` NPHI-1:0] srton;
        output [3:0] gate_sgnl;
        wire hi;
        wire lo;
        wire [11:0] count;
        wire rise;
        wire fall;
    assign gate_sgnl[0] = hi && sync; // D top
        assign gate_sgnl[1] = lo && syncb; // D bot
        assign gate_sgnl[2] = lo && syncb; // E top
        assign gate_sgnl[3] = hi && sync; // E bot
        // Pulse generation of width srton
pwmCtl_2 pwm1_inst(.clk(clk),
        .rst(rst),
        .fall(fall),
        .rise(rise),
        .max(srton),
        .Hi_O(hi),
        .Lo_O(lo));
        // Edge detector
edge_detector dtct_1(.clk(clk),
        .rst(rst),
        .puls_in(sync),
        .rise(rise),
        .fall(fall));
endmodule
```

The details of the pulse generation and edge detector blocks are as follows:

Pulse generation:

```
module pwmCtl_2(clk,
        rst,
        rise,
        fall,
        max,
        Hi_O,
        Lo_O
        );
        input clk;
        input rst;
        input rise;
        input fall;
        input [` NPHI-1:0] max; // SR Ton
        output Hi_O;
        output Lo_O;
        reg PO;
        reg Hi_O;
        reg Lo_O;
        reg [11:0] negCount;
        reg [11:0] posCount;
        reg negLock;
        reg posLock;
        always @ (posedge clk or posedge rst)begin
                if(rst)begin
                        negCount <= 12d0;
                        negLock <= 1b0;
```

```
        end
        else begin
                if(fall && negCount < max && !negLock)begin
                        negCount <= negCount + 1;
                        Lo_O <= 1'b1;
                end
                else begin
                        negCount <= 12'd0;
                        negLock <= 1'b1;
                        Lo_O <= 1'b0;
                end
                if(rise)
                        negLock <= 1'b0;
        end
end
always @ (posedge clk or posedge rst)begin
        if(rst)begin
                posCount <= 12'd0;
                posLock <= 1'b0;
                Hi_O <= 1'b0;
        end
        else begin
                if(rise && posCount < max && !posLock)begin
                        posCount <= posCount + 1;
                        Hi_O <= 1'b1;
                end
                else begin
                        posCount <= 12'd0;
```

```
                posLock <= 1'b1;
                Hi_O <= 1'b0;
            end
            if(fall)
                posLock <= 1'b0;
        end
    end
endmodule
```

Edge detector:

```
module edge_detector (clk,
    rst,
    puls_in,
    rise,
    fall);
    input clk;
    input rst;
    input puls_in;
    output rise;
    output fall;
    reg rise;
    reg fall;
  reg prev;
  reg curnt;
  reg [1:0] stat;
  always @ (posedge clk or posedge rst)begin
      if(rst)begin
          prev <= 1'b0;
          curnt <= 1'b0;
```

```
                stat <= 2'b00;
            end
            else begin
                stat <= stat[0],puls_in;
            end
    end
    always @ (posedge clk or posedge rst)begin
            if(rst)begin
                rise <= 1'b0;
                fall <= 1'b0;
            end
            else begin
                if(stat == 1)begin
                    rise <= 1'b1;
                    fall <= 1'b0;
                end
                else if(stat == 2)begin
                    rise <= 1'b0;
                    fall <= 1'b1;
                end
        end
    end
endmodule
```

B.2 MATLAB Terminal Commands

The communication to the CMOD-A7 modules were performed from MATLAB terminals. Two separate windows are to be opened, one for the primary board and the other for the secondary board. The paths in these windows need to be set to the directories where the primary and secondary board MATLAB terminal commands through UART

are stored. Then, use the following codes for steady-state operation of the primary and secondary boards.

Commands for primary board

The following code snippet shows the commands to be run for starting up the primary board.

```
function [ pg ] = BDPC_IPT_Pri_Startup(  )
clc;
%Use command 'seriallist' to find the number COM port number 'x'
BDPC_Serial_Open('COMx');          % Primary COM port opening
% In following commands, The third argument '0' - 8-bit UART, '1' - 16-bit UART
BDPC_Serial_Write_Register(9,499,0)   % 180 deg Phase Angle 250 MHz Clock
BDPC_Serial_Write_Register(1,1000,0)  % 250 kHz default with 250 MHz Clock
BDPC_Serial_Write_Register(12,499,0)        % ZVS A Phase Angle
BDPC_Serial_Write_Register(13,1,0)        % ZVS B Phase Angle
BDPC_Serial_Write_Register(21,0,0)        % Active clamp reference
% Next command enables pulses, phase shift and ZVS phase control
BDPC_Serial_Write_Register(0,2055,0)
clc;
end
```

Once this start-up command is run, change the number in the register '9' for φ_{AB} and the number in the register '12' for φ_{AZ}, to set desired output voltage at different loads and maintain full ZVS operation. While turning the system off, slowly increase the number in register '9' to reduce current input to the tank. Increase register '12' number too, such that while reducing load, the ZVS is maintained as long as input voltage is high.

To perform ADC data reads, which are available in registers '17' through '20', use the following codes, after opening up the COM port as mentioned above.

```
BDPC_Serial_Read_Register(17,0) % Input voltage ADC reading
BDPC_Serial_Read_Register(18,0) % Input current ADC reading
BDPC_Serial_Read_Register(19,0) % Output voltage ADC reading
BDPC_Serial_Read_Register(20,0) % Output current ADC reading
```

For PRBS tests, the third argument for each 'BDPC_Serial_Write_Register' command needs to be '1' to start 16-bit UART addressing. Further commands for the PRBS tests can be developed by using the other registers configured in the FPGA, accessible with the numbers up to '23'. With 16-bit addressing, higher number of registers can be accessed for PRBS data storing. Also, for reading data, use '1' for the second argument of each 'BDPC_Serial_Read_Register' command.

Commands for Secondary board

The following code snippet shows the commands to be run for starting up the secondary board.

```
function [ pg ] = BDPC_IPT_Sec_Startup(  )
clc;
%Use command 'seriallist' to find the number COM port number 'x'
BDPC_Serial_Open('COMx');          % Secondary COM port opening
% In following commands, The third argument '0' - 8-bit UART, '1' - 16-bit UART
BDPC_Serial_Write_Register(0,0,0)   % Keep SR disabled by default
BDPC_Serial_Write_Register(8,250,0)  % Default pulse width of 1 us to start
% BDPC_Serial_Write_Register(8,450,0)        % Full SR pulse width 1.8 us
clc;
end
```

After running this start-up script, enable SR operation by writing '1' to the register '0' after output power is above 150 W. This will start SR with a reduced pulse width of 1 µs. After reaching output power of 300 W, enable full pulse width SR by uncommenting the last line of the SR start-up commands listed above.

APPENDIX C

Capacitance Effects in Underwater IPT

In addition to the considerations for ac winding losses, seawater losses and core losses in the design of the coils for underwater IPT, the winding capacitances need considerations for assuring the high-frequency behavior of the systems. While winding capacitance effects are common in transformers, its effects are mostly not considered for typical IPT pad designs, except for works utilizing the winding capacitance as resonant elements. However, for high-voltage underwater IPT systems, the different capacitances and common-mode path formed between the primary and secondary systems through the partially conductive seawater needs consideration.

C.1 Transformer Equivalent Circuit with Parasitic Capacitances

A typical parasitic capacitance equivalent model of a two-winding transformer is shown in Fig. C.1, which shows the primary winding equivalent capacitance (C_{pp}), secondary winding equivalent capacitance (C_{ss}) and the common-mode capacitance (C_{ps}) between the windings [132]. The winding equivalent capacitances (C_{pp} and C_{ps}) are typically more prominent, which form between different turns and layers of each of these windings. Sectionalizing the windings into smaller portions with no overlapping between them, or interleaving different sections of the windings help in reducing the electric field build-up within the transformer and correspondingly these capacitance effects. The winding-to-winding capacitance, also called the common-mode capacitance, is typically lower, but for high-frequency applications this plays a critical role, as the voltage gradient between the windings can always remain high. As a result, high-frequency transformers such as gate drive isolation transformers require this capacitance to be strictly controlled.

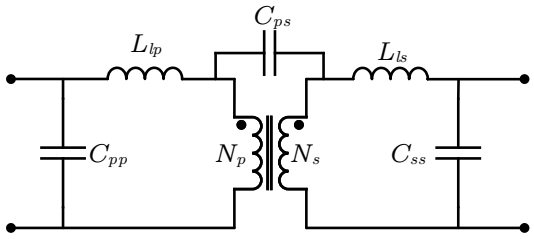

Fig. C.1: Parasitic capacitance model of a two-winding transformer.

C.2 Formation of Capacitances in Underwater IPT Systems

In underwater IPT, the power transfer medium is seawater, which necessitates the coils be put in a thin, hermetically sealed enclosures within the AUVs. Also, the seawater represent a highly lossy dielectric, with its dielectric constant dependent upon the conductivity. The ferrite pads associated with the pads also have a fairly high dielectric constants, which cause large capacitances to form wherever the windings are separated from the seawater through the ferrite pads. The formation of these capacitances is shown for a two-pad underwater IPT system in Fig. C.2, which is also relevant for the system designed for this dissertation work.

Similar to the case of a transformer, the effects of these capacitances are manifested through the energy stored in them and the dv/dt occurring across them. In the present work, the high-voltage primary coil designed with large number of turns was found to have sufficient equivalent capacitance to cause visible spike in the primary tank current closer to full-power operation, when the inbverter switching dv/dt was occurring across the equivalent capacitance C_{pp}. Also, the capacitance formed between the two pads through the plastic enclosures, seawater and the ferrite pads create a complex common-mode current path, which significantly changes the common-mode impedance of the system. It was observed in our experiements, that a considerable amount of common-mode current was flowing when the ferrite pads were kept in close contact with the seawater.

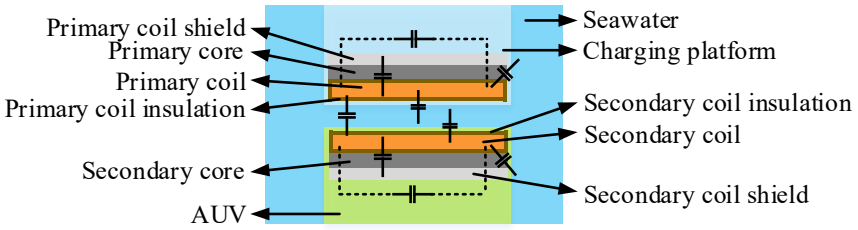

Fig. C.2: Formation of different parasitic capacitances in a two-pad underwater IPT system.

C.3 Possible Ways to Avoid Effects of these Capacitances

From the above-mentioned discussion about formations of different capacitances in underwater IPT, the following ways can be identified to avoid effects of these capacitances.

- Design each coil for the lowest voltage possible, such that the energy stored in the parasitic capacitances are lower and hence they do not affect the system performance.
- Design the compensation tank using symmetrical component distribution in the positive and negative lines of the tank, and use common-mode and differential-mode filters to block any currents drawn by these parasitic capacitances. This is the procedure adapted in the present dissertation work, as designing the coil for low voltage was not feasible.
- Avoid any contact between the ferrite and the seawater, as the coil and the seawater separated by the high dielectric constant ferrite material forms a high capacitive coupling. This is achieved in the present work by putting the coils in underwater coil boxes, and placing the ferrites away from the seawater side. This is also commensurate with how the coils are to be placed in an actual AUV. However, in an actual installation, their will be aluminum shielding on the pads, which will cause additional capacitance associated with the pads. These need to be carefully considered as well.

CURRICULUM VITAE

Anindya Chitta Bagchi

Submitted/Published Journal Articles

J1 A. C. Bagchi, A. Kamineni, R. Zane and R. B. Carlson, "Review and Comparative Analysis of Topologies and Control Methods in Dynamic Wireless Charging of Electric Vehicles," in *IEEE Journal of Emerging and Selected Topics in Power Electronics*, *undergoing revision.*

J2 T. Saha, A. C. Bagchi and R. Zane, "Analysis and Design of an LCL–T Resonant DC–DC Converter for Underwater Power Supply," in *IEEE Transactions on Power Electronics.*

Journal Articles to be Submitted

J3 A. C. Bagchi, T. Saha and R. Zane, "Design of a Constant Voltage Output Wireless Power Supply for Autonomous Underwater Vehicles Fed from a Constant Low-Current Source," in *IEEE Journal of Emerging and Selected Topics in Power Electronics*, *to be re-submitted.*

J4 T. Saha, A. C. Bagchi and R. Zane, "Bidirectional LCL–T Resonant DC–DC Converter for Critical Loads in Undersea Distribution Network," in *IEEE Transactions on Power Electronics.*

Patents

P1 A. C. Bagchi, T. Saha, A. Kamineni and R. Zane, *Wireless Charger for Underwater Vehicles Fed From a Constant Current Distribution Cable*, patent filed, Jul. 2019.

P2 T. Saha, A. C. Bagchi, H. Wang and R. Zane, *Constant DC current input to constant DC voltage output power supply covering a wide programmable range*, patent filed, June, 2019.

P3 T. Saha, A. C. Bagchi, R. Zane and H. Wang, *Dual active bridge bi-directional resonant DC-DC converter for load independent constant current to constant voltage conversion and vice versa over wide range*, disclosure filed, June, 2020.

Published Conference Papers

C1 A. C. Bagchi, T. Saha, A. Kamineni and R. Zane, "Analysis and Design of a Wireless Charger for Underwater Vehicles Fed from a Constant Current Distribution Cable," in *Proc. 2018 IEEE 19th Workshop on Control and Modeling for Power Electronics (COMPEL)*, Padua, Italy, 2018, pp. 1-8.

C2 A. C. Bagchi, A. Kamineni and R. Zane, "Analytical Optimization of a Litz Wire Spiral Coil Based Underwater IPT System," in *Proc. 2018 IEEE Energy Conversion Congress and Exposition (ECCE)*, Portland, OR, 2018, pp. 2456-2463.

C3 A. C. Bagchi, H. Wang, T. Saha and R. Zane, "Small-Signal Phasor Modeling of an Underwater IPT System in Constant Current Distribution," in *Proc. 2019 IEEE Applied Power Electronics Conference and Exposition (APEC)*, Anaheim, CA, USA, 2019, pp. 876-883.

C4 A. C. Bagchi, A. Kamineni, R. Zane and R. B. Carlson, "Comparative Analysis of DWPT Topologies and Regulation Schemes for Improved Controllability," in *Proc. 2020 IEEE Energy Conversion Congress and Exposition (ECCE)*, Detroit, MI, USA, 2020, pp. 5199-5206,.

C5 T. Saha, A. C. Bagchi, H. Wang and R. Zane, "Analysis and Design of Wide Range Output Voltage Regulated Power Supply for Underwater Constant Input Current DC Distribution System," in *Proc. 2018 IEEE 19th Workshop on Control and Modeling for Power Electronics (COMPEL)*, Padua, Italy, 2018, pp. 1-7.

C6 T. Saha, A. C. Bagchi and R. Zane, "Time-Domain Analysis and ZVS Assistance Design for a DAB LCL-T Resonant Converter in Underwater Current Distribution Network," in *Proc. 2020 IEEE 21st Workshop on Control and Modeling for Power Electronics (COMPEL)*, *in press.*

REFERENCES

[1] D. Patil, M. K. McDonough, J. M. Miller, B. Fahimi, and P. T. Balsara, "Wireless power transfer for vehicular applications: Overview and challenges," *IEEE Transactions on Transportation Electrification*, vol. 4, no. 1, pp. 3–37, March 2018.

[2] Q. Zhu, L. Wang, Y. Guo, C. Liao, and F. Li, "Applying lcc compensation network to dynamic wireless ev charging system," *IEEE Transactions on Industrial Electronics*, vol. 63, no. 10, pp. 6557–6567, Oct 2016.

[3] H. Feng, T. Cai, S. Duan, J. Zhao, X. Zhang, and C. Chen, "An lcc-compensated resonant converter optimized for robust reaction to large coupling variation in dynamic wireless power transfer," *IEEE Transactions on Industrial Electronics*, vol. 63, no. 10, pp. 6591–6601, Oct 2016.

[4] F. Lu, H. Zhang, H. Hofmann, and C. C. Mi, "A dynamic charging system with reduced output power pulsation for electric vehicles," *IEEE Transactions on Industrial Electronics*, vol. 63, no. 10, pp. 6580–6590, Oct 2016.

[5] T. Orekan, P. Zhang, and C. Shih, "Analysis, design, and maximum power-efficiency tracking for undersea wireless power transfer," *IEEE Journal of Emerging and Selected Topics in Power Electronics*, vol. 6, no. 2, pp. 843–854, June 2018.

[6] Z. Cheng, Y. Lei, K. Song, and C. Zhu, "Design and loss analysis of loosely coupled transformer for an underwater high-power inductive power transfer system," *IEEE Transactions on Magnetics*, vol. 51, no. 7, pp. 1–10, July 2015.

[7] J. Shi, D. Li, and C. Yang, "Design and analysis of an underwater inductive coupling power transfer system for autonomous underwater vehicle docking applications," *Journal of Zhejiang University SCIENCE C.*, vol. 15, no. 1, pp. 51–62, 2014.

[8] T. Kan, R. Mai, P. P. Mercier, and C. C. Mi, "Design and analysis of a three-phase wireless charging system for lightweight autonomous underwater vehicles," *IEEE Transactions on Power Electronics*, vol. 33, no. 8, pp. 6622–6632, Aug 2018.

[9] W. Haibing, Z. Kehan, Y. Zhengchao, and S. Baowei, "Comparison of two electromagnetic couplers in an inductive power transfer system for autonomous underwater vehicle docking application," in *OCEANS - Shanghai, 2016*, Apr 2016, pp. 1–5.

[10] J. H. Kim, B. Lee, J. Lee, S. Lee, C. Park, S. Jung, S. Lee, K. Yi, and J. Baek, "Development of 1-mw inductive power transfer system for a high-speed train," *IEEE Transactions on Industrial Electronics*, vol. 62, no. 10, pp. 6242–6250, Oct 2015.

[11] J. Shin, S. Shin, Y. Kim, S. Ahn, S. Lee, G. Jung, S. Jeon, and D. Cho, "Design and implementation of shaped magnetic-resonance-based wireless power transfer system for roadway-powered moving electric vehicles," *IEEE Transactions on Industrial Electronics*, vol. 61, no. 3, pp. 1179–1192, March 2014.

[12] S. Y. Choi, S. Y. Jeong, B. W. Gu, G. C. Lim, and C. T. Rim, "Ultraslim s-type power supply rails for roadway-powered electric vehicles," *IEEE Transactions on Power Electronics*, vol. 30, no. 11, pp. 6456–6468, Nov 2015.

[13] V. Vu, M. Dahidah, V. Pickert, and V. Phan, "A high-power multiphase wireless dynamic charging system with low output power pulsation for electric vehicles," *IEEE Journal of Emerging and Selected Topics in Power Electronics*, pp. 1–1, 2019.

[14] C. Park, S. Lee, S. Y. Jeong, G. Cho, and C. T. Rim, "Uniform power i-type inductive power transfer system with dq-power supply rails for on-line electric vehicles," *IEEE Transactions on Power Electronics*, vol. 30, no. 11, pp. 6446–6455, Nov 2015.

[15] S. Zhou, C. Zhu, S. Cui, Z. Wang, S. Zhou, and C. C. Chan, "Dynamic wireless power transfer system for electric vehicles employing multiplexing lcc modules with individual transmitters," *IEEE Access*, vol. 6, pp. 62 514–62 527, 2018.

[16] Z. Wang, S. Cui, S. Han, K. Song, C. Zhu, M. I. Matveevich, and O. S. Yurievich, "A novel magnetic coupling mechanism for dynamic wireless charging system for electric vehicles," *IEEE Transactions on Vehicular Technology*, vol. 67, no. 1, pp. 124–133, Jan 2018.

[17] M. Budhia, G. A. Covic, and J. T. Boys, "Design and optimization of circular magnetic structures for lumped inductive power transfer systems," *IEEE Transactions on Power Electronics*, vol. 26, no. 11, pp. 3096–3108, Nov 2011.

[18] R. Tavakoli and Z. Pantic, "Analysis, design and demonstration of a 25-kw dynamic wireless charging system for roadway electric vehicles," *IEEE Journal of Emerging and Selected Topics in Power Electronics*, 2017, to be published.

[19] P. K. S. Jayathurathnage, A. Alphones, D. M. Vilathgamuwa, and A. Ong, "Optimum transmitter current distribution for dynamic wireless power transfer with segmented array," *IEEE Transactions on Microwave Theory and Techniques*, vol. 66, no. 1, pp. 346–356, Jan 2018.

[20] A. Ong, P. K. S. Jayathurathnage, J. H. Cheong, and W. L. Goh, "Transmitter pulsation control for dynamic wireless power transfer systems," *IEEE Transactions on Transportation Electrification*, vol. 3, no. 2, pp. 418–426, June 2017.

[21] L. Zhao, D. J. Thrimawithana, U. K. Madawala, A. P. Hu, and C. C. Mi, "A misalignment-tolerant series-hybrid wireless ev charging system with integrated magnetics," *IEEE Transactions on Power Electronics*, vol. 34, no. 2, pp. 1276–1285, Feb 2019.

[22] S. Zhou and C. Chris Mi, "Multi-paralleled lcc reactive power compensation networks and their tuning method for electric vehicle dynamic wireless charging," *IEEE Transactions on Industrial Electronics*, vol. 63, no. 10, pp. 6546–6556, Oct 2016.

[23] G. R. Nagendra, G. A. Covic, and J. T. Boys, "Sizing of inductive power pads for dynamic charging of evs on ipt highways," *IEEE Transactions on Transportation Electrification*, vol. 3, no. 2, pp. 405–417, June 2017.

[24] A. Zaheer, M. Neath, H. Z. Z. Beh, and G. A. Covic, "A dynamic ev charging system for slow moving traffic applications," *IEEE Transactions on Transportation Electrification*, vol. 3, no. 2, pp. 354–369, June 2017.

[25] A. Kamineni, M. J. Neath, A. Zaheer, G. A. Covic, and J. T. Boys, "Interoperable ev detection for dynamic wireless charging with existing hardware and free resonance," *IEEE Transactions on Transportation Electrification*, vol. 3, no. 2, pp. 370–379, June 2017.

[26] S. Samanta and A. K. Rathore, "A new current-fed clc transmitter and lc receiver topology for inductive wireless power transfer application: Analysis, design, and experimental results," *IEEE Transactions on Transportation Electrification*, vol. 1, no. 4, pp. 357–368, 2015.

[27] A. Kamineni, G. A. Covic, and J. T. Boys, "Self-Tuning Power Supply for Inductive Charging," *IEEE Transactions on Power Electronics*, vol. 32, no. 5, pp. 3467–3479, 2017.

[28] K. Lee, Z. Pantic, and S. M. Lukic, "Reflexive field containment in dynamic inductive power transfer systems," *IEEE Transactions on Power Electronics*, vol. 29, no. 9, pp. 4592–4602, Sep. 2014.

[29] F. Faradjizadeh, M. Vilathgamuwa, D. Jovanovic, P. Jayathurathnage, G. Ledwich, and U. Madawala, "Expandable n-legged converter to drive closely spaced multi transmitter wireless power transfer systems for dynamic charging," *IEEE Transactions on Power Electronics*, pp. 1–1, 2019.

[30] L. Zhao, D. J. Thrimawithana, and U. K. Madawala, "Hybrid bidirectional wireless ev charging system tolerant to pad misalignment," *IEEE Transactions on Industrial Electronics*, vol. 64, no. 9, pp. 7079–7086, Sep. 2017.

[31] S. A. Schelkunoff, *Electromagnetic Waves*. D. Van Nostrand Co., New York, 1943, p. 145.

[32] C. R. Teeneti, T. T. Truscott, D. N. Beal, and Z. Pantic, "Review of wireless charging systems for autonomous underwater vehicles," *IEEE Journal of Oceanic Engineering*, pp. 1–20, 2019.

[33] G. A. Covic and J. T. Boys, "Modern trends in inductive power transfer for transportation applications," *IEEE Journal of Emerging and Selected Topics in Power Electronics*, vol. 1, no. 1, pp. 28–41, March 2013.

[34] A. N. Azad, "Energy management of dynamic wireless power transfer systems for electric vehicle applications," Ph.D. dissertation, Utah State University, Logan, UT, 2019. [Online]. Available: https://digitalcommons.usu.edu/etd/7643

[35] N. Tesla, "Apparatus for transmitting electrical energy." December 1914. [Online]. Available: http://www.freepatentsonline.com/1119732.html

[36] A. Kamineni, M. J. Neath, G. A. Covic, and J. T. Boys, "A Mistuning-Tolerant and Controllable Power Supply for Roadway Wireless Power Systems," *IEEE Transactions on Power Electronics*, vol. 32, no. 9, pp. 6689–6699, 2017.

[37] J. Dai and D. C. Ludois, "A survey of wireless power transfer and a critical comparison of inductive and capacitive coupling for small gap applications," *IEEE Transactions on Power Electronics*, vol. 30, no. 11, pp. 6017–6029, 2015.

[38] H. Zhang, F. Lu, H. Hofmann, W. Liu, and C. C. Mi, "A four-plate compact capacitive coupler design and lcl-compensated topology for capacitive power transfer in electric vehicle charging application," *IEEE Transactions on Power Electronics*, vol. 31, no. 12, pp. 8541–8551, 2016.

[39] S. Sinha, A. Kumar, B. Regensburger, and K. K. Afridi, "A new design approach to mitigating the effect of parasitics in capacitive wireless power transfer systems for electric vehicle charging," *IEEE Transactions on Transportation Electrification*, vol. 5, no. 4, pp. 1040–1059, 2019.

[40] "Jackson: Classical Electrodynamics, 3rd Edition - Student Companion Site." [Online]. Available: http://bcs.wiley.com/he-bcs/Books?action=index&itemId=047130932X&bcsId=3728

[41] R. L. Steigerwald, "A review of soft-switching techniques in high performance dc power supplies," in *Industrial Electronics, Control, and Instrumentation, 1995., Proceedings of the 1995 IEEE IECON 21st International Conference on*, vol. 1, Nov 1995, pp. 1–7 vol.1.

[42] S. Li and C. C. Mi, "Wireless power transfer for electric vehicle applications," *IEEE Journal of Emerging and Selected Topics in Power Electronics*, vol. 3, no. 1, pp. 4–17, March 2015.

[43] D. van Wageningen and T. Staring, "The qi wireless power standard," in *Proceedings of 14th International Power Electronics and Motion Control Conference EPE-PEMC 2010*, 2010, pp. S15–25–S15–32.

[44] "Wireless power transfer for light-duty plug-in/electric vehicles and alignment methodology j2954˙201904," Apr. 2019, Private Communication. [Online]. Available: https://www.sae.org/standards/content/j2954_201904/

[45] H. H. Wu, A. Gilchrist, K. D. Sealy, and D. Bronson, "A high efficiency 5 kw inductive charger for evs using dual side control," *IEEE Transactions on Industrial Informatics*, vol. 8, no. 3, pp. 585–595, 2012.

[46] H. Hwang, J. Moon, B. Lee, C. Jeong, and S. Kim, "An analysis of magnetic resonance coupling effects on wireless power transfer by coil inductance and placement," *IEEE Transactions on Consumer Electronics*, vol. 60, no. 2, pp. 203–209, 2014.

[47] Z. Yang, W. Liu, and E. Basham, "Inductor Modeling in Wireless Links for Implantable Electronics," *IEEE Transactions on Magnetics*, vol. 43, no. 10, pp. 3851–3860, 2007.

[48] "Autonomous Underwater Vehicle, REMUS 600." [Online]. Available: https://www.kongsberg.com/maritime/products/marine-robotics/autonomous-underwater-vehicles/AUV-remus-600/

[49] "Bluefin 1.5 kwh subsea battery." [Online]. Available: https://gdmissionsystems.com/products/underwater-vehicles/bluefin-robotics/1-5-kwh-subsea-battery

[50] D. M. Crimmins, C. T. Patty, M. A. Beliard, J. Baker, J. C. Jalbert, R. J. Komerska, S. G. Chappell, and D. R. Blidberg, "Long-endurance test results of the solar-powered auv system," in *OCEANS 2006*, 2006, pp. 1–5.

[51] R. Stokey, B. Allen, T. Austin, R. Goldsborough, N. Forrester, M. Purcell, and C. von Alt, "Enabling technologies for remus docking: an integral component of an autonomous ocean-sampling network," *IEEE Journal of Oceanic Engineering*, vol. 26, no. 4, pp. 487–497, 2001.

[52] R. Coulson, J. C. Lambiotte, G. Grenon, T. Pantelakis, J. Curran, and A. An, "Development of a modular docking sub-system for 12" class autonomous underwater vehicles," in *Oceans '04 MTS/IEEE Techno-Ocean '04 (IEEE Cat. No.04CH37600)*, vol. 3, 2004, pp. 1745–1749 Vol.3.

[53] B. Allen, T. Austin, N. Forrester, R. Goldsborough, A. Kukulya, G. Packard, M. Purcell, and R. Stokey, "Autonomous docking demonstrations with enhanced remus technology," in *OCEANS 2006*, 2006, pp. 1–6.

[54] H. Painter and J. Flynn, "Current and future wet-mate connector technology developments for scientific seabed observatory applications," in *OCEANS 2006*, 2006, pp. 1–6.

[55] G. Guidi, J. A. Suul, F. Jenset, and I. Sorfonn, "Wireless charging for ships: High-power inductive charging for battery electric and plug-in hybrid vessels," *IEEE Electrification Magazine*, vol. 5, no. 3, pp. 22–32, Sep. 2017.

[56] L. Tan, N. Zhu, and B. Wu, "An integrated inductor for eliminating circulating current of parallel three-level dc–dc converter-based ev fast charger," *IEEE Transactions on Industrial Electronics*, vol. 63, no. 3, pp. 1362–1371, 2016.

[57] L. Tan, B. Wu, S. Rivera, and V. Yaramasu, "Comprehensive dc power balance management in high-power three-level dc–dc converter for electric vehicle fast charging," *IEEE Transactions on Power Electronics*, vol. 31, no. 1, pp. 89–100, 2016.

[58] J. Ferrieux, G. Kwimang, G. Meunier, B. Sarrazin, A. Derbey, T. Ghanbari, and E. Farjah, "Maximising transferred power and preserving zero voltage switching in grid to vehicle and vehicle to grid modes of a wireless charging system," *IET Electrical Systems in Transportation*, vol. 10, no. 2, pp. 196–203, 2020.

[59] T. Fujita, T. Yasuda, and H. Akagi, "A dynamic wireless power transfer system applicable to a stationary system," *IEEE Transactions on Industry Applications*, vol. 53, no. 4, pp. 3748–3757, July 2017.

[60] H. Wang, "Design and control of series resonant converters for dc current power distribution applications," Ph.D. dissertation, Utah State University, Logan, UT, 2018. [Online]. Available: https://digitalcommons.usu.edu/etd/7160

[61] H. Wang, T. Saha, and R. Zane, "Small Signal Phasor Modeling of Phase-shift Modulated Series Resonant Converters with Constant Input Current," *2018 IEEE 19th Workshop on Control and Modeling for Power Electronics (COMPEL)*, pp. 1–8, 2018.

[62] H. Wang, T. Saha, B. Riar, and R. Zane, "Design considerations for current-regulated series-resonant converters with a constant input current," *IEEE Transactions on Power Electronics*, vol. 34, no. 1, pp. 141–150, Jan 2019.

[63] H. Wang, R. A. Zane, and T. Saha, "Dc power supply from a constant current source," September 2019. [Online]. Available: http://www.freepatentsonline.com/y2019/0296650.html

[64] H. Wang, T. Saha, B. Riar, and R. Zane, "Operational study and protection of a series resonant converter with dc current input applied in dc current distribution systems," in *2018 International Power Electronics Conference (IPEC-Niigata 2018 -ECCE Asia)*, May 2018, pp. 4145–4150.

[65] T. Saha, H. Wang, B. Riar, and R. Zane, "Analysis and design of a parallel resonant converter for constant current input to constant voltage output dc-dc converter over wide load range," in *2018 International Power Electronics Conference (IPEC-Niigata 2018 -ECCE Asia)*, 2018, pp. 4074–4079.

[66] T. Saha, A. C. Bagchi, H. Wang, and R. Zane, "Analysis and design of wide range output voltage regulated power supply for underwater constant input current dc distribution system," in *2018 IEEE 19th Workshop on Control and Modeling for Power Electronics (COMPEL)*, June 2018, pp. 1–7.

[67] C. T. Rim and G. H. Cho, "Phasor Transformation and its Application to the DC/AC Analyses of Frequency Phase-controlled Series Resonant Converters (SRC)," *IEEE Transactions on Power Electronics*, vol. 5, no. 2, pp. 201–211, 1990.

[68] S. Lee, B. Choi, and C. T. Rim, "Dynamics Characterization of the Inductive Power Transfer System for Online Electric Vehicles by Laplace Phasor Transform," *IEEE Transactions on Power Electronics*, vol. 28, no. 12, pp. 5902–5909, 2013.

[69] Z. U. Zahid, Z. M. Dalala, C. Zheng, R. Chen, W. E. Faraci, J. J. Lai, G. Lisi, and D. Anderson, "Modeling and control of series–series compensated inductive power transfer system," *IEEE Journal of Emerging and Selected Topics in Power Electronics*, vol. 3, no. 1, pp. 111–123, March 2015.

[70] J. P. K. Sampath, A. Alphones, and H. Shimasaki, "Coil design guidelines for high efficiency of wireless power transfer (wpt)," in *2016 IEEE Region 10 Conference (TENCON)*, 2016, pp. 726–729.

[71] R. Bosshard, U. Iruretagoyena, and J. W. Kolar, "Comprehensive evaluation of rectangular and double-d coil geometry for 50 kw/85 khz ipt system," *IEEE Journal of Emerging and Selected Topics in Power Electronics*, vol. 4, no. 4, pp. 1406–1415, 2016.

[72] K. H. Zhang, Z. B. Zhu, B. W. Song, and D. M. Xu, "A Power Distribution Model of Magnetic Resonance WPT System in Seawater," in *IEEE 2nd Annual Southern Power Electronic Conference (SPEC)*. IEEE, 2016, pp. 1–4.

[73] A. Jenkins, V. Bana, and G. Anderson, "Impedance of a coil in seawater," in *IEEE Antennas and Propagation Society International Symposium (APSURSI), 2014*, July 2014, pp. 625–626.

[74] J. Zhou, D. J. Li, and Y. Cheng, "Frequency selection of an inductive contactless power transmission system for ocean observing," *Ocean Engineering*, vol. 60, no. Supplement C., pp. 175–185, 2013.

[75] M. B. Kraichman, "Impedance of a Circular Loop in an Infinite Conducting Medium," *Journal of Research of the National Bureau of Standards- D. Radio Propagation*, vol. 66D, no. 4, pp. 499–503, July-August 1962.

[76] J. Huh, S. W. Lee, W. Y. Lee, G. H. Cho, and C. T. Rim, "Narrow-width inductive power transfer system for online electrical vehicles," *IEEE Transactions on Power Electronics*, vol. 26, no. 12, pp. 3666–3679, Dec 2011.

[77] J. Zhao, T. Cai, S. Duan, H. Feng, C. Chen, and X. Zhang, "A general design method of primary compensation network for dynamic wpt system maintaining stable transmission power," *IEEE Transactions on Power Electronics*, vol. 31, no. 12, pp. 8343–8358, Dec 2016.

[78] R. Bosshard, J. W. Kolar, J. Mühlethaler, I. Stevanović, B. Wunsch, and F. Canales, "Modeling and η-α-pareto optimization of inductive power transfer coils for electric vehicles," *IEEE Journal of Emerging and Selected Topics in Power Electronics*, vol. 3, no. 1, pp. 50–64, Mar 2015.

[79] Z. Yan, Y. Zhang, T. Kan, F. Lu, K. Zhang, B. Song, and C. C. Mi, "Frequency optimization of a loosely coupled underwater wireless power transfer system considering eddy current loss," *IEEE Transactions on Industrial Electronics*, vol. 66, no. 5, pp. 3468–3476, May 2019.

[80] S. Y. Choi, B. W. Gu, S. Y. Jeong, and C. T. Rim, "Advances in wireless power transfer systems for roadway-powered electric vehicles," *IEEE Journal of Emerging and Selected Topics in Power Electronics*, vol. 3, no. 1, pp. 18–36, March 2015.

[81] C. C. Mi, G. Buja, S. Y. Choi, and C. T. Rim, "Modern advances in wireless power transfer systems for roadway powered electric vehicles," *IEEE Transactions on Industrial Electronics*, vol. 63, no. 10, pp. 6533–6545, Oct 2016.

[82] Y. Shin, K. Hwang, J. Park, D. Kim, and S. Ahn, "Precise vehicle location detection method using a wireless power transfer (wpt) system," *IEEE Transactions on Vehicular Technology*, vol. 68, no. 2, pp. 1167–1177, Feb 2019.

[83] S. Choi, J. Huh, W. Y. Lee, S. W. Lee, and C. T. Rim, "New cross-segmented power supply rails for roadway-powered electric vehicles," *IEEE Transactions on Power Electronics*, vol. 28, no. 12, pp. 5832–5841, Dec 2013.

[84] S. Y. Jeong, J. H. Park, G. P. Hong, and C. T. Rim, "Autotuning control system by variation of self-inductance for dynamic wireless ev charging with small air gap," *IEEE Transactions on Power Electronics*, vol. 34, no. 6, pp. 5165–5174, June 2019.

[85] Y. Guo, L. Wang, Q. Zhu, C. Liao, and F. Li, "Switch-on modeling and analysis of dynamic wireless charging system used for electric vehicles," *IEEE Transactions on Industrial Electronics*, vol. 63, no. 10, pp. 6568–6579, Oct 2016.

[86] S. Wang, H. Feng, H. Hu, J. Chen, Z. Hu, C. Rong, T. Cai, and M. Liu, "Optimisation design for series–series dynamic wpt system maintaining stable transfer power," *IET Power Electronics*, vol. 10, no. 9, pp. 987–995, 2017.

[87] Y. Liu, R. Mai, D. Liu, Y. Li, and Z. He, "Efficiency optimization for wireless dynamic charging system with overlapped dd coil arrays," *IEEE Transactions on Power Electronics*, vol. 33, no. 4, pp. 2832–2846, April 2018.

[88] J. M. Miller, O. C. Onar, C. White, S. Campbell, C. Coomer, L. Seiber, R. Sepe, and A. Steyerl, "Demonstrating dynamic wireless charging of an electric vehicle: The benefit of electrochemical capacitor smoothing," *IEEE Power Electronics Magazine*, vol. 1, no. 1, pp. 12–24, March 2014.

[89] A. N. Azad, A. Echols, V. A. Kulyukin, R. Zane, and Z. Pantic, "Analysis, optimization, and demonstration of a vehicular detection system intended for dynamic wireless charging applications," *IEEE Transactions on Transportation Electrification*, vol. 5, no. 1, pp. 147–161, March 2019.

[90] X. Dai, J. Jiang, and J. Wu, "Charging area determining and power enhancement method for multiexcitation unit configuration of wirelessly dynamic charging ev system," *IEEE Transactions on Industrial Electronics*, vol. 66, no. 5, pp. 4086–4096, May 2019.

[91] D. Patil, J. Miller, B. Fahimi, P. T. Balsara, and V. Galigerkere, "A coil detection system for dynamic wireless charging of electric vehicle," *IEEE Transactions on Transportation Electrification*, pp. 1–1, 2019.

[92] L. Xiang, X. Li, J. Tian, and Y. Tian, "A crossed dd geometry and its double-coil excitation method for electric vehicle dynamic wireless charging systems," *IEEE Access*, vol. 6, pp. 45 120–45 128, 2018.

[93] G. de Freitas Lima and R. B. Godoy, "Modeling and prototype of a dynamic wireless charging system using lsps compensation topology," *IEEE Transactions on Industry Applications*, vol. 55, no. 1, pp. 786–793, Jan 2019.

[94] Y. Li, J. Hu, T. Lin, X. Li, F. Chen, Z. He, and R. Mai, "A new coil structure and its optimization design with constant output voltage and constant output current for electric vehicle dynamic wireless charging," *IEEE Transactions on Industrial Informatics*, vol. 15, no. 9, pp. 5244–5256, Sep. 2019.

[95] Y. Huang, C. Liu, Y. Zhou, Y. Xiao, and S. Liu, "Power allocation for dynamic dual-pickup wireless charging system of electric vehicle," *IEEE Transactions on Magnetics*, vol. 55, no. 7, pp. 1–6, July 2019.

[96] X. Ge, Y. Sun, Z. Wang, and C. Tang, "Dual-independent-output inverter for dynamic wireless power transfer system," *IEEE Access*, vol. 7, pp. 107 320–107 333, 2019.

[97] J. M. Arteaga, S. Aldhaher, G. Kkelis, D. C. Yates, and P. D. Mitcheson, "Multi-mhz ipt systems for variable coupling," *IEEE Transactions on Power Electronics*, vol. 33, no. 9, pp. 7744–7758, Sep. 2018.

[98] Z. Zhang, W. Ai, Z. Liang, and J. Wang, "Topology-reconfigurable capacitor matrix for encrypted dynamic wireless charging of electric vehicles," *IEEE Transactions on Vehicular Technology*, vol. 67, no. 10, pp. 9284–9293, Oct 2018.

[99] A. Babaki, S. Vaez-Zadeh, and A. Zakerian, "Performance optimization of dynamic wireless ev charger under varying driving conditions without resonant information," *IEEE Transactions on Vehicular Technology*, vol. 68, no. 11, pp. 10 429–10 438, Nov 2019.

[100] X. Liu, C. Liu, and P. W. T. Pong, "Tmr-sensor-array-based misalignment-tolerant wireless charging technique for roadway electric vehicles," *IEEE Transactions on Magnetics*, vol. 55, no. 7, pp. 1–7, July 2019.

[101] J. M. Miller, O. C. Onar, and M. Chinthavali, "Primary-side power flow control of wireless power transfer for electric vehicle charging," *IEEE Journal of Emerging and Selected Topics in Power Electronics*, vol. 3, no. 1, pp. 147–162, March 2015.

[102] G. A. Covic, J. T. Boys, M. L. G. Kissin, and H. G. Lu, "A three-phase inductive power transfer system for roadway-powered vehicles," *IEEE Transactions on Industrial Electronics*, vol. 54, no. 6, pp. 3370–3378, Dec 2007.

[103] Z. Zhang, H. Pang, C. H. T. Lee, X. Xu, X. Wei, and J. Wang, "Comparative analysis and optimization of dynamic charging coils for roadway-powered electric vehicles," *IEEE Transactions on Magnetics*, vol. 53, no. 11, pp. 1–6, Nov 2017.

[104] T. Saha, H. Wang, and R. Zane, "Zero Voltage Switching Assistance Design for DC-DC Series Resonant Converter with Constant Input Current for Wide Load Range," *2017 IEEE 18th Workshop on Control and Modeling for Power Electronics (COMPEL)*, 2017.

[105] D. Seltzer and R. Zane, "Feedback Control of Phase Shift Modulated Half Bridge Circuits for Zero Voltage Switching Assistance," in *IEEE 14^{th} Workshop on Control and Modeling for Power Electronics (COMPEL), 2013*, June 2013, pp. 1–6.

[106] L. Corradini, D. Seltzer, D. Bloomquist, R. Zane, D. Maksimović, and B. Jacobson, "Zero voltage switching technique for bidirectional dc/dc converters," *IEEE Transactions on Power Electronics*, vol. 29, no. 4, pp. 1585–1594, Apr 2014.

[107] W. Zhang and C. C. Mi, "Compensation topologies of high-power wireless power transfer systems," *IEEE Transactions on Vehicular Technology*, vol. 65, no. 6, pp. 4768–4778, June 2016.

[108] Y. H. Sohn, B. H. Choi, E. S. Lee, G. C. Lim, G. H. Cho, and C. T. Rim, "General Unified Analyses of Two-Capacitor Inductive Power Transfer Systems: Equivalence of Current-Source SS and SP Compensations," *IEEE Transactions on Power Electronics*, vol. 30, no. 11, pp. 6030–6045, November 2015.

[109] A. K. Swain, M. J. Neath, U. K. Madawala, and D. J. Thrimawithana, "A Dynamic Multivariable State-Space Model for Bidirectional Inductive Power Transfer Systems," *IEEE Transactions on Power Electronics*, vol. 27, no. 11, pp. 4772–4780, 2012.

[110] E. X. Yang, F. C. Lee, and M. M. Jovanovic, "Small-signal modeling of series and parallel resonant converters," in *[Proceedings] APEC '92 Seventh Annual Applied Power Electronics Conference and Exposition*, 1992, pp. 785–792.

[111] K. Aditya and S. S. Williamson, "Simplified Mathematical Modelling of Phase-shift Controlled Series-Series Compensated Inductive Power Transfer System," in *2016 IEEE 25th International Symposium on Industrial Electronics (ISIE)*. IEEE, 2016, pp. 842–848.

[112] Marn Go Kim and Myung Joong Youn, "A discrete time domain modeling and analysis of controlled series resonant converter," *IEEE Transactions on Industrial Electronics*, vol. 38, no. 1, pp. 32–40, 1991.

[113] D. Seltzer, L. Corradini, D. Bloomquist, R. Zane, and D. Maksimovic, "Small Signal Phasor Modeling of Dual Active Bridge Series Resonant DC/DC Converters with Multi-angle Phase Shift Modulation," *2011 IEEE Energy Conversion Congress and Exposition (ECCE)*, pp. 2757–2764, 2011.

[114] L. Chen, G. R. Nagendra, J. T. Boys, and G. A. Covic, "Double-coupled systems for ipt roadway applications," *IEEE Journal of Emerging and Selected Topics in Power Electronics*, vol. 3, no. 1, pp. 37–49, March 2015.

[115] R. Tanzania, F. H. Choo, and L. Siek, "Design of WPT Coils to Minimize AC Resistance and Capacitor Stress Applied to SS-topology," in *41st Annual Conference of the IEEE Industrial Electronics Society (IECON-2015)*. IEEE, January 2015, pp. 00 118–00 122.

[116] "Product selection guide, new england wire technologies," pp. 127–136. [Online]. Available: https://www.newenglandwire.com/technical-resources/product-selection-guide

[117] J. Kim and Y. J. Park, "Approximate Closed-Form Formula for Calculating Ohmic Resistance in Coils of Parallel Round Wires With Unequal Pitches," *IEEE Transactions on Industrial Electronics*, vol. 62, no. 6, pp. 3482–3489, 2015.

[118] C. M. Zierhofer and E. S. Hochmair, "Geometric Approach for Coupling Enhancement of Magnetically Coupled Coils," *IEEE Transactions on Biomedical Engineering*, vol. 43, no. 7, pp. 708–714, 1996.

[119] C. R. Sullivan, "Optimal Choice for Number of Strands in a Litz-Wire Transformer Winding," *IEEE Transactions on Power Electronics*, vol. 14, no. 2, pp. 283–291, Mar 1999.

[120] "Log interpretation charts, schlumberger," pp. 7–8, 2013. [Online]. Available: http://pages.geo.wvu.edu/~tcarr/pttc/schlumberger_chartbook.pdf

[121] J. P. K. Sampath, A. Alphones, and D. M. Vilathgamuwa, "Figure of Merit for the Optimization of Wireless Power Transfer System Against Misalignment Tolerance," *IEEE Transactions on Power Electronics*, vol. 32, no. 6, pp. 4359–4369, June 2017.

[122] C. T. Rim and C. Mi, *Coupled Coil Model*. IEEE, 2017, pp. 53–65.

[123] A. Safaee and K. Woronowicz, "Time-domain analysis of voltage-driven series–series compensated inductive power transfer topology," *IEEE Transactions on Power Electronics*, vol. 32, no. 7, pp. 4981–5003, 2017.

[124] H. Hao, G. A. Covic, and J. T. Boys, "A Parallel Topology for Inductive Power Transfer Power Supplies," *IEEE Transactions on Power Electronics*, vol. 29, no. 3, pp. 1140–1151, March 2014.

[125] C. R. Sullivan, "Optimal choice for number of strands in a litz-wire transformer winding," *IEEE Transactions on Power Electronics*, vol. 14, no. 2, pp. 283–291, March 1999.

[126] H. Hao, G. A. Covic, and J. T. Boys, "An approximate dynamic model of lcl- t-based inductive power transfer power supplies," *IEEE Transactions on Power Electronics*, vol. 29, no. 10, pp. 5554–5567, Oct 2014.

[127] B. J. Varghese, R. Tavakoli, Z. Pantic, R. A. Zane, and A. Kamineni, "Multi-pad receivers for high power dynamic wireless power transfer," in *2020 IEEE Energy Conversion Congress and Exposition (ECCE)*, Oct. 2020, in press.

[128] V. Shevchenko, O. Husev, R. Strzelecki, B. Pakhaliuk, N. Poliakov, and N. Strzelecka, "Compensation topologies in ipt systems: Standards, requirements, classification, analysis, comparison and application," *IEEE Access*, vol. 7, pp. 120 559–120 580, 2019.

[129] M. Shirazi, J. Morroni, A. Dolgov, R. Zane, and D. Maksimovic, "Integration of frequency response measurement capabilities in digital controllers for dc–dc converters," *IEEE Transactions on Power Electronics*, vol. 23, no. 5, pp. 2524–2535, 2008.

[130] B. Miao, R. Zane, and D. Maksimovic, "System identification of power converters with digital control through cross-correlation methods," *IEEE Transactions on Power Electronics*, vol. 20, no. 5, pp. 1093–1099, 2005.

[131] T. Saha, "Soft-switched resonant dc-dc converter in underwater dc power distribution network," Ph.D. dissertation, Utah State University, Logan, UT, 2020. [Online]. Available: https://digitalcommons.usu.edu/etd/7955

[132] F. Blache, J. . Keradec, and B. Cogitore, "Stray capacitances of two winding transformers: equivalent circuit, measurements, calculation and lowering," in *Proceedings of 1994 IEEE Industry Applications Society Annual Meeting*, vol. 2, 1994, pp. 1211–1217 vol.2.